COUPLED TRACE ELEMENT ANALYSIS AND CATHODOLUMINESCENCE IMAGING APPLIED TO ANATECTIC ALUMINOUS GRANULITES: THE METAMORPHIC RECORD OF QUARTZ AND KYANITE

by © Jillian Kendrick

A thesis submitted to the School of Graduate Studies in partial fulfillment of the requirements for the degree of

Master of Science

Department of Earth Sciences

Memorial University of Newfoundland

December 2017

St. John's Newfoundland and Labrador

ABSTRACT

Anatectic aluminous granulites from the Grenville Province, Canada, are investigated using trace element analysis and cathodoluminescence (CL) mapping of quartz and kyanite. Two types of quartz: crystals resorbed during partial melting and retrograde pseudomorphs after partial melt, are identified by CL mapping. Titanium-in-quartz thermobarometry for each type is evaluated in the context of phase equilibria modelling. Despite the presence of rutile, most quartz did not reach equilibrium Ti concentrations, especially during melt crystallisation. Kyanite porphyroblasts in high-pressure samples are found to be composite crystals comprising up to three generations of kyanite, two prograde and one retrograde. These are linked to a metamorphic reaction history consistent with phase equilibria modelling, and are used to provide additional constraints on the *P–T* evolution of these rocks. Trace element analysis and CL mapping are valuable complements to traditional methods of investigating high-grade metamorphic rocks.

ACKNOWLEDGMENTS

First and foremost, I would like to express my gratitude to my supervisor, Aphrodite Indares. Not only did she fund this work and provide the samples, she gave me invaluable opportunities to learn and explore, particularly when it came to the EPMA. The knowledge that Aphrodite shared with me is also indispensable – including, but not limited to, the thermodynamic principles fundamental to metamorphic petrology, the intricacies of interpreting the metamorphic history of anatectic aluminous granulites (or any other metamorphic rock), and how to make a good cappuccino. I feel that largely because of her, I was able to get the most out of my Masters program at MUN, and the experience I gained here will aid me for many years to come.

I would like to thank my committee members, John Hanchar and Roger Mason, for their valuable advice (particularly regarding the EPMA) and constructive reviews of my thesis. Wanda Aylward in the EPMA lab also deserves recognition for the huge amount of training and assistance she has given me over the course of my program. I appreciate the assistance of David Grant and Dylan Goudie in the SEM lab, whether I was collecting maps for my project or for someone else. Markus Wälle is acknowledged for his patience and assistance in the LA-ICP-MS lab and with the data reduction. I must also thank Mackenzie Patrick for teaching me how to use Thermocalc.

Many people in the community of the MUN Earth Sciences department have encouraged me along the way, and are too numerous to all be named here. These include the morning coffee crowd (Sharon Deemer, Chuck Hurich and many others), members of the faculty (Greg Dunning, Toby Rivers, and others) and staff, and many graduate

students. I am also grateful for financial support from the School of Graduate Studies, NSERC, the Dr. Alfred K. Snelgrove Graduate Scholarship, the F.A. Aldrich Graduate Award, and the Mineralogical Association of Canada.

Finally, I want to thank my family for their encouragement along the way, most of all my mother for her undying support.

TABLE OF CONTENTS

LIST OF TABLES

LIST OF FIGURES

LIST OF ABBREVIATIONS

T	Temperature
P	Pressure
kb	Kilobars
°C	Degrees Celsius
ppm	Parts per million
kV	Kilovolts
nA	Nanoamps
ms	Milliseconds
nm	Nanometers
µm	Micrometers (microns)
wt. %	Weight percent
j	Joules
Hz	Hertz
NCKFMASH	Na_2O-CaO-K_2O-FeO-MgO-Al_2O_3-SiO_2-H_2O
NCKFMASHTO	Na_2O-CaO-K_2O-FeO-MgO-Al_2O_3-SiO_2-H_2O-TiO_2-O
MnNCKFMASHTO	MnO-Na_2O-CaO-K_2O-FeO-MgO-Al_2O_3-SiO_2-H_2O-TiO_2-O
Ma	Millions of years
AFM diagram	Aluminium-Iron-Magnesium ternary plot
fO_2	Oxygen fugacity
X_{grs} (of garnet)	Grossular component of garnet
X_{Fe} (of garnet)	Fe/Mg ratio of garnet

LIST OF APPENDICES

CHAPTER 1: INTRODUCTION AND OVERVIEW

1.1 Objectives of the thesis

Interpreting the history of metamorphosed aluminous rocks is vital to understanding the tectonic processes that operate in orogenic systems. The wide variety of minerals that can occur in rocks of aluminous bulk compositions at different *P–T* conditions allows first-order assessments of the metamorphic history to be made with relative ease. In addition, these rocks undergo extensive anatexis under granulite-facies conditions, and thus understanding their mineralogy and textures can shed light on this important process.

Through the application of phase equilibria modelling using internally consistent thermodynamic databases and mineral activity-composition models, mineral assemblages, textures, and mineral chemistry can be integrated and interpreted, allowing the *P–T* path of the rock during metamorphism to be estimated (e.g., Indares et al., 2008; Guilmette et al., 2011; Lasalle & Indares, 2014). Chemical zonation of individual minerals, typically garnet, is a particularly valuable feature to interpret using phase equilibria modelling, as it can provide important constraints on *P–T* paths. However, this technique alone is not always sufficient, and information from other metamorphic minerals could place important additional constraints on metamorphic history.

Minerals with a relatively simple major element chemistry may retain important information about their growth history in their trace element chemistry, and in some minerals, the distribution of these trace elements can be imaged at high resolution using

cathodoluminescence (CL). Therefore, trace element analyses coupled with CL or back-scattered electron (BSE) imaging or wavelength dispersive spectroscopy (WDS) X-ray maps are useful tools for investigating metamorphic rocks (and most rocks in general).

The aim of this thesis is to evaluate the potential of this approach using trace element analyses and CL imaging for assessing the metamorphic history of anatectic aluminous granulites, using rocks from the Manicouagan area of the central Grenville Province (Canada). This is accomplished by targeting two common and luminescent minerals in this type of rock, quartz and kyanite. Incorporation of trace Ti^{4+} into quartz is known to be linked to *P–T* conditions (Wark & Watson, 2006), and the CL emission in quartz has been linked empirically to the Ti content (Müller et al., 2002; Leeman et al., 2012); however, Ti-in-quartz has been relatively underexplored in anatectic aluminous granulites. The luminescence of kyanite is mainly attributed to trace Cr^{3+} (e.g., Wojtowicz, 1991), and investigating kyanite porphyroblasts using CL could reveal details of their growth history, and therefore the metamorphic evolution of the rock.

1.2 Background

1.2.1 Trace elements and cathodoluminescence

1.2.1.1 Quartz

Under certain conditions, trace amounts of Ti may substitute for Si in quartz. This substitution is dependent upon three main factors: 1) the temperature; 2) pressure; and 3) activity of Ti (a_{TiO2}) of the system in which the quartz crystallized or equilibrated. Several studies of experimental and natural systems have demonstrated a positive correlation between temperature and the Ti content of quartz (e.g., Wark & Watson, 2006; Kawasaki

& Osanai, 2008), and a negative correlation between pressure and Ti content (e.g., Thomas et al., 2010; Huang & Audétat, 2012). In most cases, a_{TiO2} is the most important and complex factor to consider. If the system is saturated with respect to TiO_2 (i.e. TiO_2 is in excess), $a_{TiO2} = 1.0$. The presence of rutile in equilibrium with quartz indicates that quartz crystallized in a system saturated with TiO_2, and that the Ti content of quartz is not restricted by Ti availability. In a system lacking rutile, $a_{TiO2} < 1.0$, leaving less Ti available for incorporation into quartz. In natural systems, a_{TiO2} is related to temperature, pressure, and activities of other components, making estimation of a_{TiO2} difficult if rutile is absent (Ghent & Stout, 1984). The Ti content of natural quartz is typically 0–150 ppm (e.g., Wiebe et al., 2007; Spear & Wark, 2009), with the highest Ti concentrations of up to 250 ppm found in high temperature settings such as anatectic metamorphic rocks with peak $T > 800$°C (e.g., Storm & Spear, 2009).

Several Ti-in-quartz thermo(baro)meters have been proposed, based mainly on synthesis experiments in which quartz is produced in equilibrium with rutile. "TitaniQ" by Wark & Watson (2006) was the first, calculated from the results of heating finely ground SiO_2 with TiO_2 powders between 600°C and 1000°C at 10.0 kb. This initial calibration was a simple thermometer and was later updated by Thomas et al. (2010) to include the effect of pressure on Ti-in-quartz; quartz and rutile were grown at pressures ranging from 5 to 20 kbar at a relatively narrow range of temperatures (700 to 940°C). Another Ti-in-quartz thermobarometer was developed by Huang & Audétat (2012) by heating natural and synthetic quartz crystals in the presence of crushed rutile at temperatures between 600 and 850°C and pressures of 1.0, 2.0, and 10.0 kb. Quartz overgrowths resulting from the experiment were analysed to determine their Ti content,

and the calibration produced different results from that of Thomas et al. (2010). Thomas et al. (2015) recently evaluated the Thomas et al. (2010) calibration in comparison to that of Huang & Audétat (2012) by reproducing the experiments of the former and cross-checking the results with Zr-in-rutile thermobarometry. Thomas et al. (2015) also noted that the experimental approach of Huang & Audétat (2012) did not guarantee rutile saturation during quartz growth and that a_{TiO2} gradients were likely present, lending uncertainty to the reliability of this thermobarometer. Given that the experiments of Thomas et al. (2010) have been shown to give more consistent and reproducible results with better evidence for equilibrium between quartz and rutile than the those of Huang & Audétat (2012) (Thomas et al., 2015), the Ti-in-quartz thermobarometer proposed by the former is the calibration used in this thesis.

Although quartz appears to be homogeneous under the optical microscope and in BSE images, the trace element distribution in quartz may preserve complex patterns related to various geological processes (Rusk, 2014, and references therein). These textures can be imaged using CL, and several studies have shown a general empirical relationship between Ti content and a particular CL emission; the two typically have a strong positive correlation (Müller et al., 2002; Rusk et al., 2008; Leeman et al., 2012). The Ti distribution in quartz imaged using CL has shown high resolution growth zonation, fluid inclusion trails, zonation at the rims of grains caused by diffusion, and annealed fractures, among other textures (Müller et al., 2002; Rusk et al., 2008; Spear & Wark, 2009; Leeman et al., 2012; Morgan et al., 2014). However, the origin of CL emissions in quartz is complex and not restricted to the presence of Ti.

Cathodoluminescence emissions in quartz may arise from two general sources: "intrinsic" defects in the quartz structure and defects caused by structurally-bound trace elements in quartz (Rusk, 2014 and references therein). Several studies have used an empirical approach to investigate the contribution of trace Ti in the quartz crystal structure to the CL spectrum. Müller et al. (2002) and Leeman et al. (2012) approached the issue by obtaining CL spectra from quartz crystals and attempting to determine the origin of the peaks. Müller et al. (2002) found eight principle peaks in natural quartz from granitic rocks, four in the blue range of the spectrum (481, 463, 444, and 417 nm), and four in red/yellow range (717, 674, 633, and 577 nm) (Figure 1.1a). Measured Ti concentrations (< 20-85 ppm) showed a positive correlation with the 417 nm emission peak intensity; zones and crystals with a reddish CL colour were found to be Ti-poor. Leeman et al. (2012) examined both natural and synthetic quartz known to contain Ti. Their CL spectra showed three major peaks at 642, 566, and 456 nm, and a linear correlation was found between 456 nm peak intensity and Ti content of the quartz crystal or zone (Figure 1.1b). By producing CL intensity maps of each peak alone, Leeman et al. (2012) found that the 642 and 566 nm peaks were more prominent in Ti-poor quartz; maps of 456 nm intensity were considered to be equivalent to Ti content maps. The data of Rusk et al. (2008) support the proposed correlation between Ti content and CL emission intensity, as their high temperature (500-750°C) hydrothermal quartz showed a direct positive correlation between the two.

1.2.1.2 Kyanite

In comparison to quartz, there has been relatively little investigation of the trace element chemistry of kyanite. Early work was the most extensive, including studies by

Hietanen (1956), Pearson & Shaw (1960), Herz & Dutra (1964), and Chinner et al. (1969), along with the more recent work of Müller et al. (2016). Collectively, these authors determined that kyanite may contain significant amounts of Cr, Fe, V, Ti, Ga, Mg, Li, and Na (and less commonly others), and the meaning of some trace element concentrations in kyanite has been addressed. Chinner et al. (1969) and Müller et al. (2016) observed that the amount of Fe, typically the most abundant trace element in kyanite, reflects the Fe^{3+}/Fe^{2+} ratio, or oxidation state, of the rock. The latter study examined kyanite from a range of geologic settings, including metapelites, metamorphosed granites, metamorphosed alteration zones, and metabasites. The diverse bulk compositions of these rocks allowed Müller et al. (2016) to determine that the Cr and V content of the kyanite varied as a function of bulk Cr and V of the protoliths. These authors also found a positive correlation between Ti content and formation temperature of kyanite. Evidence of significant chemical zonation within kyanite has also been identified. For instance, Yang & Rivers (2001) revealed strong zonation within kyanite porphyroblasts in amphibolite-facies aluminous rocks using WDS X-ray maps. These crystals showed broad core and rim zones defined by Fe content and sharp, concentric annuli of high and low Cr, which are locally bifurcated. Yang & Rivers (2001) interpreted that Cr zonation in those kyanite is an inherited feature, caused by kyanite overgrowing Cr-bearing phases such as micas in the groundmass.

The CL spectrum of typical kyanite is dominated by a broad red emission (centred at ~ 740 nm) superimposed by two narrow and intense peaks (Figure 1.2a), which have all been determined to be caused by trace Cr^{3+} occupying Al *sites* in the kyanite structure, and the intensities of these emissions have been positively correlated with the Cr content

(Wojtowicz, 1991; Müller et al., 2016 and references therein). A relatively low-intensity blue emission has also been recognized (centred at ~ 485 nm) and linked empirically to trace Ti in kyanite (Figure 1.2b, Müller et al., 2016). Müller et al. (2016) additionally found that trace Fe has a quenching effect on kyanite CL, as no CL could be detected from most kyanite crystals with relatively high Fe (e.g., > 3200 ppm).

1.2.2 Geological setting

The Grenville Province in Canada represents the remnants of the Mesoproterozoic Grenville Orogen, which formed by progressive accretion and final continental collision on the southeastern margin of Laurentia (Rivers et al., 2012). It is interpreted to have been the first large hot orogen on Earth, analogous to the modern Himalaya-Tibet Orogen (Rivers et al., 2012). Much of the Grenville Province comprises amphibolite- to granulite-facies rocks, which likely represent the middle to lower crust of a former orogenic plateau in the hinterland of the Grenville Orogen (Rivers et al., 2012). The Grenville Province therefore provides a window into the architecture of lower levels of continental crust in a large hot orogen, and an opportunity to investigate crustal processes involved in orogenesis. The Manicouagan area in the central Grenville Province (Figure 3) hosts a suite of well-documented aluminous granulites belonging to several distinct domains at different structural levels.

Structurally lowest is the Gagnon terrane, which represents the Parautochthonous belt in the central Grenville Province (Figure 1.3; Rivers et al., 1989). This terrane comprises tonalitic Archean basement and continental margin metasedimentary sequences, which were deformed into a northwest-verging metamorphic fold and thrust belt during the Grenville Orogeny (Rivers, 1983a,b; Rivers et al., 1993; van Gool et al.,

2008). The metamorphic grade of the Gagnon terrane varies from greenschist facies at the Grenville Front to high-*P* granulite and eclogite at its southern structural contact with the overlying hinterland (Rivers, 1983a; Indares, 1993; Indares, 1995). In the Manicouagan area, the high-*P* metamorphism was dated at ca. 985 Ma, suggesting that the Gagnon terrane was metamorphosed during the Rigolet phase, or the final stage, of the Grenville Orogeny (Jordan et al., 2006). High-*P* metamorphism was accompanied by partial melting facilitated by biotite breakdown up to ca. 13 kb and 840°C, with a moderately-sloping, hairpin-shaped *P–T* path (Jordan et al., 2006; Indares et al., 2008). Thrusting of hinterland rock onto the southern end of the Gagnon terrane is interpreted as the cause of the high-*P* metamorphism (Jordan et al., 2006).

The Manicouagan Imbricate Zone, exposed north of the Manicouagan impact structure (Figure 1.3), comprises stacked tectonic slices of the former Grenvillian hinterland dipping toward the southeast. These rocks are part of a high-*P* belt exposed discontinuously throughout the Grenville Province (Rivers et al., 2002) near the contact between parautochthonous and allochthonous units, and host high-*P* granulites and eclogites. In the west, the Manicouagan Imbricate Zone is dominated by anorthositic suites (Lelukuau terrane; Indares et al., 1998; Indares et al., 2000). The southeast comprises a series of complex rock packages, with a large unit of ca. 1450 Ma diorite containing rafts of supracrustal rocks, intruded by ca. 1170 Ma gabbro (Indares et al., 1998; Cox et al., 1998; Indares et al., 2000). Supracrustal rocks including aluminous gneisses resembling those of the Canyon domain (see below) are exposed at the southern tip of the Manicouagan Imbricate Zone to the south of the Manicouagan impact structure (Dunning & Indares, 2010). Mafic rocks preserve high-*P* and eclogite facies assemblages

(Cox et al., 1999; Indares, 2003) and the aluminous gneisses are interpreted to have undergone partial melting by dehydration of micas in the kyanite stability field, at *P–T* conditions up to 15 kb and 840–870°C with a steep retrograde *P–T* path (Indares & Dunning, 2001; Indares et al., 2008; Lasalle & Indares, 2014). The timing of metamorphism of these rocks has been constrained to ca. 1040–1030 Ma (Cox et al., 1998; Indares & Dunning, 2001; Dunning & Indares, 2010), similar to ages obtained elsewhere in the Manicouagan Imbricate Zone (Indares et al., 1998; Indares et al., 2000). This coincides with the Ottawan phase, the culmination of the Grenville Orogeny.

The Canyon domain, which overlies the Gagnon terrane and has an unknown relationship to the Manicouagan Imbricate Zone, is exposed to the south of the Manicouagan impact crater (Figure 1.3). Thick packages of layered rocks dominate this domain, including a mafic to intermediate unit dated at ca. 1410 Ma (Dunning & Indares, 2010), and a ca. 1234 Ma bimodal felsic–mafic sequence locally with aluminous layers (Indares & Moukhsil, 2013; Lasalle et al., 2013). Metamorphic assemblages in mafic and aluminous rocks are consistent with medium-*P* granulite facies metamorphism. The aluminous rocks display evidence of partial melting by dehydration of micas in the stability field of sillimanite, at ca. 820–880°C (Lasalle & Indares, 2014). The timing of metamorphism in the Canyon domain has been constrained to ca. 1080–1040 Ma (Dunning & Indares, 2010), during the Ottawan phase of the Grenville Orogeny.

In the present study, five previously documented samples with *P–T* paths determined by phase equilibria modelling are examined (sample locations in Figure 1.3). These are: kyanite-bearing sample 100 of the Gagnon terrane (Jordan et al., 2006; GT100 in Indares et al., 2008), kyanite-bearing sample 320 of the Manicouagan Imbricate Zone

(BNS3b in Indares & Dunning, 2001; Indares et al., 2008), kyanite-bearing sample 107b of the Manicouagan Imbricate Zone (BNS2b in Indares & Dunning, 2001; Indares et al., 2008), kyanite-bearing sample 244 of the Manicouagan Imbricate Zone (Lasalle & Indares, 2014), and sillimanite-bearing sample HJ60b of the Canyon domain (Lasalle & Indares, 2014).

1.3 Organisation of the thesis

This work comprises two manuscript-style chapters, chapters 2 and 3, which will each be published in international peer-reviewed scientific journals. Chapter 1, the current chapter, is an overview of the thesis project. Chapter 2 is an investigation of quartz in anatectic aluminous granulites using CL imaging and Ti-in-quartz thermobarometry. The results are evaluated in the framework of phase equilibria modelling and compared to the previously constrained *P–T* paths of these rocks. Chapter 3 is a study of kyanite in high-*P* anatectic aluminous granulites using CL imaging and trace element analysis. Multiple generations of kyanite are identified, and their growth and resorption are linked to phase equilibria modelling. Lastly, chapter 4 is a summary that gives the overall conclusions and implications of this thesis.

References

Chinner, G.A., Smith, J.V., & Knowles, C.R. (1969). Transition-metal contents of Al2SiO5 polymorphs. American Journal of Science, 267, 96–113.

Cox, R.A., Dunning, G.R., & Indares, A. (1998). Petrology and U–Pb geochronology of mafic, high-pressure, metamorphic coronites from the Tshenukutish domain, eastern Grenville Province. Precambrian Research, 90, 59–83.

Cox, R.A., & Indares, A. (1999). Transformation of Fe–Ti gabbro to coronite, eclogite and amphibolite in the Baie du Nord segment, Manicouagan Imbricate Zone, eastern Grenville Province. Journal of Metamorphic Geology, 17, 537–555.

Dunning, G., & Indares, A. (2010). New insights on the 1.7–1.0 Ga crustal evolution of the central Grenville Province from the Manicouagan – Baie Comeau transect. Precambrian Research, 180, 204–226.

Guilmette, C., Indares, A., & Hébert, R. (2011). High-pressure anatectic paragneisses from the Namche Barwa, Eastern Himalayan Syntaxis: Textural evidence for partial melting, phase equilibria modeling and tectonic implications. Lithos, 124, 66–81.

Herz, N., & Dutra, C.V. (1964). Geochemistry of some kyanites from Brazil. The American Mineralogist, 49, 1290–1305.

Hietanen, A. (1956). Kyanite, andalusite, and sillimanite in the schist in Boehls Butte Quadrangle, Idaho. The American Mineralogist, 41, 1–27.

Huang, R., & Audétat, A. (2012). The titanium-in-quartz (TitaniQ) thermobarometer: A critical examination and re-calibration. Geochimica et Cosmochimica Acta, 84, 75–89.

Indares, A. (1993). Eclogitized gabbros from the eastern Grenville Province: Textures, metamorphic context, and implications. Canadian Journal of Earth Sciences, 30, 159–173.

Indares, A. (1995). Metamorphic interpretation of high-pressure–temperature metapelites with preserved growth zoning in garnet, eastern Grenville Province, Canadian Shield. Journal of Metamorphic Geology, 13, 475–486.

Indares, A. D. (2003). Metamorphic textures and P–T evolution of high-P granulites from the Lelukuau terrane, NE Grenville Province. Journal of Metamorphic Geology, 21, 35–48.

Indares, A., & Dunning, G. (2001). Partial melting of high-P–T metapelites from the Tshenukutish terrane (Grenville Province): Petrography and U–Pb geochronology. Journal of Petrology, 42, 1547–1565.

Indares, A., & Moukhsil, A. (2013). Geon 12 crustal extension in the central Grenville Province, implications for the orogenic architecture, and potential influence on the emplacement of anorthosites. Canadian Journal of Earth Sciences, 50, 955–966.

Indares, A., Dunning, G., Cox, R., Gale, D., & Connelly, J. (1998). High-pressure, high-temperature rocks from the base of thick continental crust: Geology and age constraints from the Manicouagan Imbricate Zone, eastern Grenville Province. Tectonics, 17, 426–440.

Indares, A., Dunning, G., & Cox, R. (2000). Tectono-thermal evolution of deep crust in a Mesoproterozoic continental collision setting: The Manicouagan example. Canadian Journal of Earth Sciences, 37, 325–340.

Indares, A., White, R.W., & Powell, R. (2008). Phase equilibria modelling of kyanite-bearing anatectic paragneisses from the central Grenville Province. Journal of Metamorphic Geology, 26, 815–836.

Jordan, S.L., Indares, A., & Dunning, G. (2006). Partial melting of metapelites in the Gagnon terrane below the high-pressure belt in the Manicouagan area (Grenville Province): Pressure–temperature (P–T) and U–Pb age constraints and implications. Canadian Journal of Earth Sciences, 38, 1309–1329.

Kawasaki, T., & Osanai, Y. (2008). Empirical thermometer of TiO2 in quartz for ultrahigh-temperature granulites of East Antarctica. In M. Satish-Kumar, Y. Motoyoshi, Y. Osanai, Y Hiroi, and K. Shiraishi (Eds.), Geodynamic Evolution of East Antarctica: A Key to the East-West Gondwana Connection (pp. 419-430). Geological Society, London, Special Publications 308.

Lasalle, S., & Indares, A. (2014). Anatectic record and contrasting P–T paths of aluminous gneisses from the central Grenville Province. Journal of Metamorphic Geology, 32, 627–646.

Lasalle, S., Fisher, C. M., Indares, A., & Dunning, G. (2013). Contrasting types of Grenvillian granulite facies aluminous gneisses: Insights on protoliths and

metamorphic events from zircon morphologies and ages. Precambrian Research, 228, 117–130.

Leeman, W. P., MacRae, C. M., Wilson, N. C., Torpy, A., Lee, C.-T. A., Student, J. J., Thomas, J. B., & Vicenzi, E. P. (2012). A study of cathodoluminescence and trace element compositional zoning in natural quartz from volcanic rocks: Mapping titanium content in quartz. Microscopy and Microanalysis 18, 1322–1341.

Morgan, D. J., Jollands, M. C., Lloyd, G. E., & Banks, D. A. (2014). Using titanium-in-quartz geothermometry and geospeedometry to recover temperatures in the aureole of the Ballachulish Igneous Complex, NW Scotland. Geological Society, London, Special Publications 394, 145–165.

Müller, A., Lennox, P., & Trzebski, R. (2002). Cathodoluminescence and micro-structural evidence for crystallisation and deformation processes of granites in the Eastern Lachlan Fold Belt (SE Australia). Contributions to Mineralogy and Petrology 143, 510–524.

Müller, A., van den Kerkhof, A.M., Selbekk, R.S., & Broekmans, M.A.T.M. (2016). Trace element composition and cathodoluminescence of kyanite and its petrogenetic implications. Contributions to Mineralogy and Petrology, 171, 70.

Pearson, G.R., & Shaw, D.M. (1960). Trace elements in kyanite, sillimanite and andalusite. The American Mineralogist, 45, 808–817.

Rivers, T. (1983a). Progressive metamorphism of pelitic and quartzofeldspathic rocks in the Grenville Province of western Labrador – tectonic implications of bathozone 6 assemblages. Canadian Journal of Earth Sciences, 20, 1791–1804.

Rivers, T. (1983b). The northern margin of the Grenville Province in western Labrador – anatomy of an ancient orogenic front. Precambrian Research, 22, 41–73.

Rivers, T., Martignole, J., Gower, C.F., & Davidson, A. (1989). New tectonic divisions of the Grenville Province, southeast Canadian Shield. Tectonics, 8, 63–84.

Rivers, T., van Gool, J.A.M., & Connelly, J.N. (1993). Contrasting tectonic styles in the northern Grenville Province: Implications for the dynamics of orogenic fronts. Geology, 21, 1127–1130.

Rivers, T., Ketchum, J., Indares, A., & Hynes, A. (2002). The High Pressure belt in the Grenville Province: Architecture, timing, and exhumation. Canadian Journal of Earth Sciences, 39, 867–893.

Rivers, T., Culshaw, N., Hynes, A., Indares, A., Jamieson, R., & Martignole, J. (2012). The Grenville orogen – a post lithoprobe perspective. In J.A. Percival, F.A. Cook, & R.M. Clowes (Eds.), Tectonic Styles in Canada: The Lithoprobe Perspective (pp. 97–236). Geological Survey of Canada, Special Paper 49.

Rusk, B.G., Lowers, H.A., & Reed, M.H. (2008). Trace elements in hydrothermal quartz: Relationships to cathodoluminescent textures and insights into vein formation. Geology, 36, 547–550.

Rusk, B. (2014). Quartz cathodoluminescence: Textures, trace elements, and geological applications. In I.M. Coulson (Ed.), Cathodoluminescence and its Application to Geoscience (pp. 127–142). Mineralogical Association of Canada, Mineralogical Association of Canada Short Course Series Volume 45.

Spear, F. S., & Wark, D. A. (2009). Cathodoluminescence imaging and titanium thermometry in metamorphic quartz. Journal of Metamorphic Geology 27, 187–205.

Storm, L.C., & Spear, F.S. (2009). Application of the titanium-in-quartz thermometer to pelitic migmatites from the Adirondack Highlands, New York. Journal of Metamorphic Geology, 27, 479–494.

Thomas, J. B., Watson, E. B., Spear, F. S., Shemella, P. T., Nayak, S. K., & Lanzirotti, A. (2010). TitaniQ under pressure: The effect of pressure and temperature on the solubility of Ti in quartz. Contributions to Mineralogy and Petrology 160, 743–759.

Thomas, J. B., Watson, E. B., Spear, F. S., & Wark, D. A. (2015). TitaniQ recrystallized: Experimental confirmation of the original Ti-in-quartz calibrations. Contributions to Mineralogy and Petrology 169, 27.

van Gool, J.A.M., Rivers, T., & Calon, T. (2008). Grenville Front zone, Gagnon terrane, southwestern Labrador: Configuration of a midcrustal foreland fold-thrust belt. Tectonics, 27, TC1004.

Wark, D. A., & Watson, E. B. (2006). TitaniQ: A titanium-in-quartz geothermometer. Contributions to Mineralogy and Petrology, 152, 743–754.

Wiebe, R.A., Wark, D.A., & Hawkins, D.P. (2007). Insights from quartz cathodoluminescence zoning into crystallization of the Vinalhaven granite, coastal Maine. Contributions to Mineralogy and Petrology, 154, 439–453.

Wojtowicz, A.J. (1991). Luminescence of Cr3+ in kyanite. Journal of Luminescence, 50, 221–230.

Yang, P., & Rivers, T. (2001). Chromium and manganese zoning in pelitic garnet and kyanite: Spiral, overprint, and oscillatory (?) zoning patterns and the role of growth rate. Journal of Metamorphic Geology, 19, 455–474.

CO-AUTHORSHIP STATEMENT

Chapter 2 is a manuscript entitled "The Ti record of quartz in anatectic aluminous granulites", co-authored by Aphrodite Indares (Memorial University of Newfoundland), and was submitted for publication to the *Journal of Petrology* in August 2017. Reviews were received in September 2017 (from two anonymous reviewers and Dr. Chiara Groppo), and chapter 2 is the revised version of the manuscript. As first author, I was responsible for reviewing the literature, designing analytical protocols (EPMA), collecting and interpreting data (SEM mineralogical maps, EPMA data, cathodoluminescence maps), producing phase equilibria models, and preparing and submitting the manuscript. Aphrodite Indares provided the samples, guidance and aid at all stages, and editorial comments on the manuscript.

Chapter 3 is a manuscript entitled "The reaction history of kyanite in high-pressure aluminous granulites", co-authored by Aphrodite Indares (Memorial University of Newfoundland). The original manuscript was submitted for publication to the *Journal of Metamorphic Geology* in May 2017, the reviews (by Dr. Tim Johnson and an anonymous reviewer) were received in June 2017, and it was accepted by the journal in September 2017. This chapter contains the revised version. As first author, I was responsible for reviewing the literature, designing the analytical protocol (EPMA), collecting and interpreting data (SEM mineralogical maps, EPMA and LA-ICP-MS data, cathodoluminescence maps), producing phase equilibria models, and preparing and submitting the manuscript. This study was not included in the thesis project originally offered to me and I made the decision to pursue this research. Aphrodite Indares provided the samples, guidance and aid at all stages, and editorial comments on the manuscript.

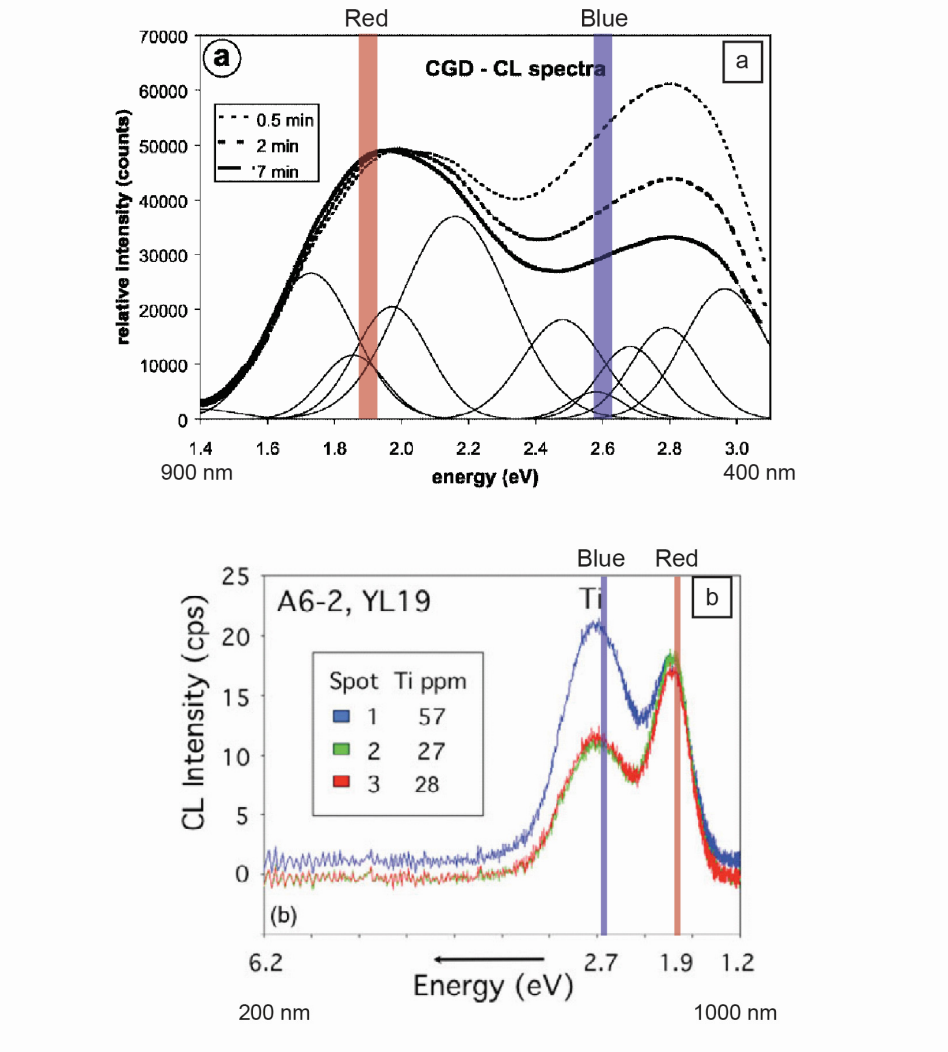

Figure 1.1. Examples of quartz CL spectra from a) Müller et al. (2002) and b) Leeman et al. (2012). Each shows broad peaks in the red and blue regions of the visible spectrum. Note the change in scale and reversal of the x-axis between a) and b).

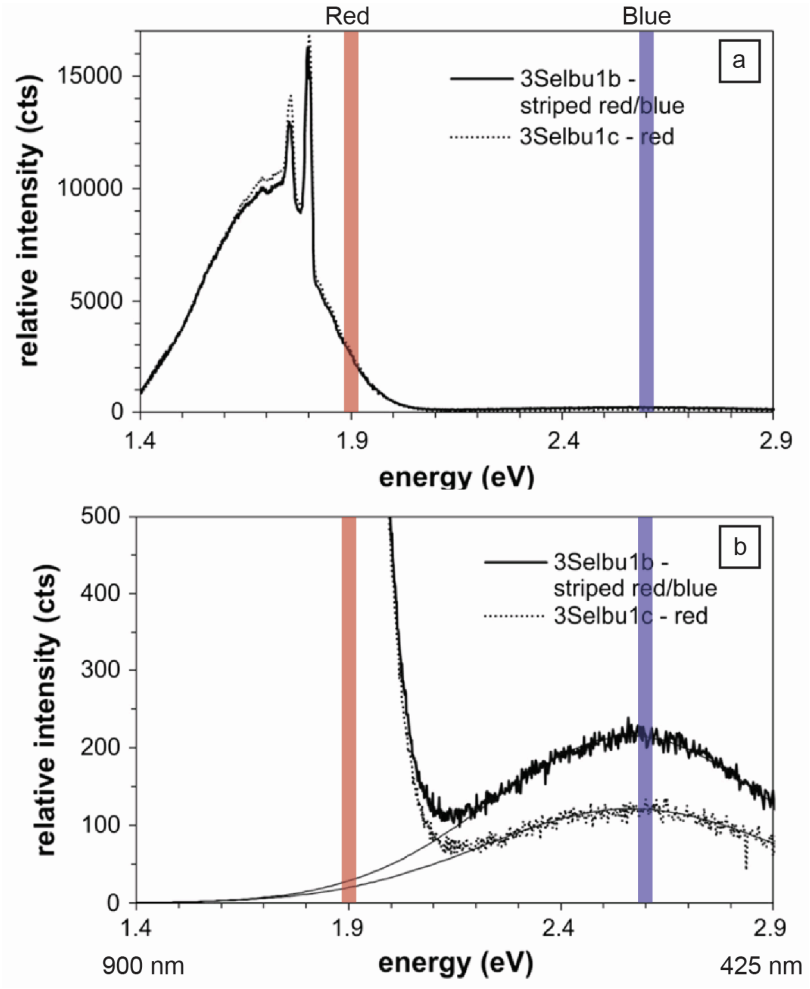

Figure 1.2. Kyanite CL spectrum from Müller et al. (2016). a) The spectrum is dominated by the characteristic Cr^{3+}-related peaks in the red region. b) Vertical exaggeration of a) showing a weak emission in the blue region of the spectrum.

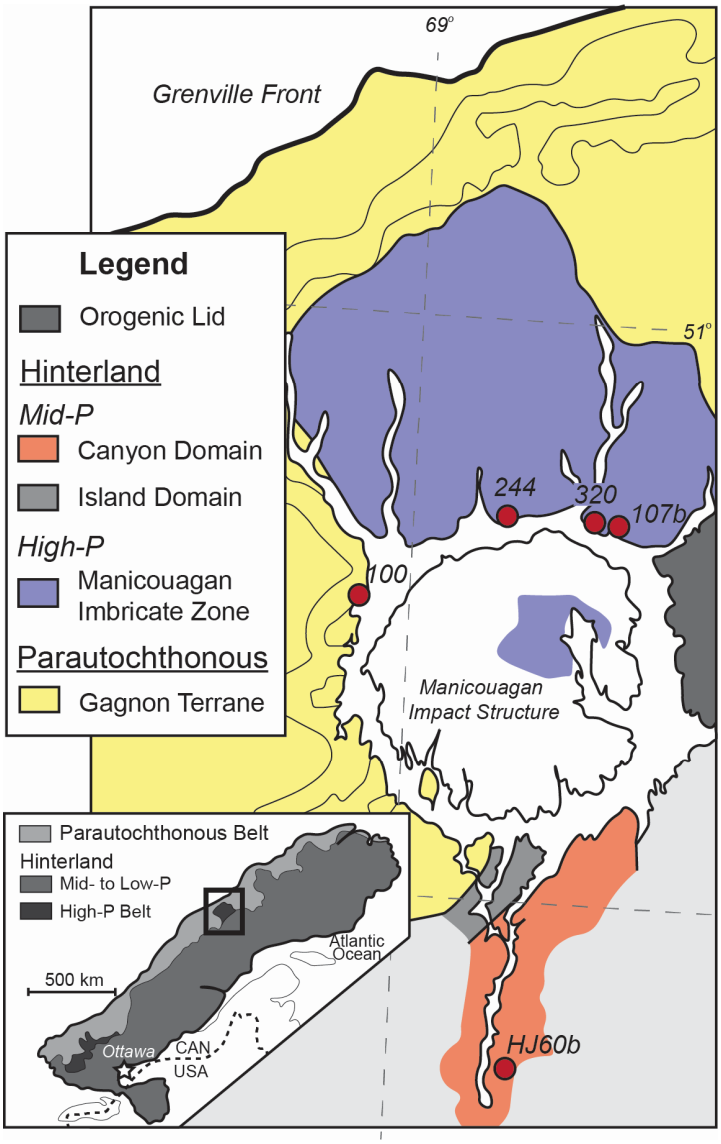

Figure 1.3. Simplified geological map of the Manicouagan area (after Dunning & Indares, 2010) with locations of the samples. Inset shows the extent of the Grenville Province and the location of the study area.

CHAPTER 2: THE TI RECORD OF QUARTZ IN ANATECTIC ALUMINOUS GRANULITES

Abstract

The distribution and concentration of Ti in quartz was assessed in five rutile-bearing anatectic aluminous granulites from the Grenville Province, Canada, each with previously constrained *P–T* paths. Characterisation of quartz in these samples with the aid of cathodoluminescence (CL) mapping revealed two distinct types in each sample, resorbed quartz partly consumed by melting reactions during the prograde portion of metamorphism and quartz grown from crystallisation of partial melt during retrogression. In two of the samples, pseudomorphs after former melt in the form of quartz overgrowths on existing quartz were discovered using CL and are not visible by other methods. The *P–T* conditions recorded by each type based on Ti-in-quartz thermobarometry are in poor agreement with *P–T* paths inferred from phase equilibria modelling. The negative correlation between Ti incorporation into quartz and *P* suggests that prograde quartz, which is expected to record near-peak *P–T*, should be Ti-poor relative to retrograde quartz, which crystallised at conditions several kbar lower than peak *P*. The opposite trend was found; retrograde quartz is typically relatively Ti-poor, and quartz overgrowths may be nearly Ti-free. Despite the presence of rutile in the samples, which is generally considered to ensure a Ti-saturated system, these results are strong evidence for Ti-undersaturation of quartz caused by disequilibrium between quartz and rutile. In addition, Zr-in-rutile thermometry generally gives lower temperatures than expected for these

rocks, which can be explained by retrograde resetting of Zr in rutile and potentially by disequilibrium between rutile and zircon. Based on these results, the degree of Ti (or Zr) saturation achieved at any stage of metamorphism should be assessed with caution, as co-existence of quartz and rutile (or rutile and zircon) within a thin section or sample may not be a sufficient criterion for equilibrium.

2.1 Introduction

Quartz is a ubiquitous phase in aluminous metamorphic rocks and contains trace amounts of Ti that are controlled by the temperature, pressure, and availability of Ti during metamorphism (Wark & Watson, 2006; Thomas et al., 2010; Huang & Audétat, 2012). Trace Ti in quartz has also been empirically linked to a particular cathodoluminescence (CL) emission (Müller et al., 2002), allowing Ti distribution in quartz to be imaged at high resolution (e.g., Leeman et al., 2012). Therefore, CL can be a useful tool in metamorphic rocks for distinguishing different types of quartz, examining their internal zoning and other structures, and for providing valuable information about the origin and history of quartz in the context of the metamorphic evolution of these rocks.

Since the initial formulation of a Ti-in-quartz thermometer by Wark & Watson (2006), the technique has become increasingly popular and has been applied to rocks from a variety of geological settings. Metamorphic rocks, however, have been relatively underexplored, particularly those metamorphosed at granulite-facies conditions (e.g.,

Spear & Wark, 2009; Storm & Spear, 2009; Zhang et al., 2014). Titanium-in-quartz has the potential to be a useful complementary technique for interpreting the *P–T* paths of such rocks for several reasons. The high temperatures associated with granulite-facies metamorphism (> 750°C) aids Ti volume diffusion in quartz (Cherniak et al., 2007) and a Ti-buffering phase such as ilmenite or rutile is typically stable at these conditions. Sluggish diffusion of Ti in quartz at lower temperatures, compared to major elements such as Fe and Mg in other minerals, could make Ti-in-quartz relatively resistant to retrograde resetting and consequently capable of recording peak *T* conditions reliably (Storm & Spear, 2009). Furthermore, aluminous granulites inevitably undergo anatexis, in which quartz plays an important role. Large quantities of quartz are consumed by melt-producing reactions (Spear & Wark, 2009), and thus new quartz grows upon crystallisation of anatectic melt during retrogression. Two populations of quartz should therefore be present in aluminous granulites: 1) resorbed relics of quartz that were present during the prograde portion of metamorphism; and 2) retrograde quartz grown from melt. Their Ti contents could yield important constraints on the anatectic record of these rocks. In addition, combining Ti-in-quartz with Zr-in-rutile thermometry (Zack et al., 2004; Ferry & Watson, 2007; Tomkins et al., 2007) could allow for even tighter constraints on peak *P–T* conditions, given that the latter has been applied to zircon-bearing aluminous granulites with some success (e.g., Luvizotto & Zack, 2009; Kooijman et al., 2012; Ewing et al., 2013).

Although Ti-in-quartz thermobarometry can be an attractive option, the application of this technique is not without challenges. The most complicated aspect and

long-standing problem is evaluating a_{TiO2}, or activity of TiO_2, in the system under consideration. The presence of rutile is generally considered to ensure TiO_2 saturation, or $a_{TiO2} = 1.0$, and although Ti-in-quartz thermobarometers are ideally calibrated in this environment, there is some debate as to whether saturation was achieved during the different calibration experiments (Thomas et al., 2010; Huang & Audétat, 2012; Thomas et al., 2015). Assigning an a_{TiO2} value to rutile-free assemblages in natural samples can therefore be difficult, although there is some consensus that aluminous rocks remain near TiO_2 saturation even for ilmenite-bearing assemblages based on analysis of natural samples and theoretical calculations (Ghent & Stout, 1984; Ashley & Law, 2015). However, even the presence of rutile may not always guarantee TiO_2 saturation; for instance, Morgan et al. (2014) found evidence for variable a_{TiO2} during contact metamorphism of rutile-bearing quartzite.

In this contribution, we investigate quartz in anatectic aluminous granulites to evaluate the potential of CL imaging for discriminating quartz related to melt production and crystallisation, and the possibility of using its Ti concentration to constrain the *P–T* range of the near-peak and retrograde anatectic record. We focus on five samples collected in the Manicouagan area of the central Grenville Province in Québec, Canada, where both high-*P,* kyanite-bearing and mid-*P,* sillimanite-bearing granulites are exposed. These rocks provide evidence of partial melting and were estimated to have reached at least 830°C based on their assemblages and phase equilibria modelling (Indares & Dunning, 2001; Jordan et al., 2006; Indares et al., 2008; Lasalle & Indares, 2014). To fully characterize quartz in these samples, we employed high-resolution

imaging techniques including CL mapping of individual grains. Different generations of quartz were identified, in some cases only visible in the CL maps, and the Ti content of each was used for Ti-in-quartz thermobarometry. In addition, trace Zr was measured in rutile for Zr-in-rutile thermometry. The results were evaluated in the context of phase equilibria models and previously established constraints on the *P–T* paths of these samples. This work has revealed the importance of CL imaging of quartz, but also major limitations of applying trace element thermobarometers to anatectic aluminous rocks, and brings into question assumptions of equilibrium in trace element systems.

2.2 Methods

2.2.1 Imaging

Entire thin sections were mapped using an FEI Quanta 400 scanning electron microscope (SEM) at Memorial University of Newfoundland (MUN) equipped with Mineral Liberation Analysis (MLA) software (JKTech, University of Queensland, Australia), operating at 25 kV with a 10 nA beam current. The MLA software generated false colour mineral maps, highlighting the distribution of quartz and its textural relationships with other phases at the thin section scale. Quartz was imaged at the grain scale by CL mapping using the xCLent IV system coupled to the JEOL JXA-8230 electron microprobe (EPMA) at MUN. Mapping conditions were 20 (for some 15) kV accelerating voltage, 200 nA beam current, and 80 ms dwell time with step sizes ranging from 1 μm to 7 μm (depending on the size of the crystal mapped). The system collects

CL maps simultaneously with wavelength-dispersive spectroscopy (WDS) X-ray maps. The xCLent IV software acquires the CL spectra, from the ultraviolet (UV) to the infrared (IR) regions of the electromagnetic spectrum, from each pixel and produces false colour maps of the relative CL intensities; particular emissions may be isolated to create wavelength-specific CL intensity maps. In all samples, quartz produced two distinct, broad peaks centred at ~ 430 nm ('blue' emission) and ~ 640 nm ('red' emission); as the former has been linked to trace Ti in quartz (Müller et al., 2002), intensity maps of this emission were used to assess the distribution of Ti in the quartz (see also Leeman et al., 2012). Silicon x-ray maps collected synchronous with CL were used to illustrate the distribution of quartz in the CL images.

2.2.2 Quantitative analysis

Quartz was quantitatively analyzed for trace Ti using the EPMA at MUN. Titanium-in-quartz analyses were done at 20 (for some 15) kV accelerating voltage and 200 nA beam current, with 240 s counting time on peak and 120 s on each background. A first set of analyses (samples 100 and 107b) were run using 15 kV following the protocol of Wark & Watson (2006), Storm & Spear (2009), and Spear & Wark (2009). Subsequent analyses (samples 244, 320, HJ60b, some for 100) were carried out at 20 kV after Donovan et al. (2011), and there appears to be no significant difference between the two datasets aside from small changes in analytical uncertainty and minimum detection limit (MDL) (all Ti-in-quartz results are available in Appendices 1 and 2). Using the Probe for EPMA software (Probe Software, Inc.), Ti counts simultaneously collected by two WDS spectrometers with PETL crystals were combined to improve analytical precision and

MDL (Donovan et al., 2011). Analytical precision was in the range of ± 3 to 4 ppm (1 σ) for 15 kV, and between ± 2 and 3 ppm (1 σ) for 20 kV. The MDL was 7 ppm for 15 kV and 5 ppm for 20 kV. These values represent minimum error, as they are based only on counting statistics; physical factors (e.g., beam stability, beam focus, fluctuations in room temperature) can have a significant effect on uncertainty for trace element analyses. For each quartz analysis, SiO_2 was fixed at 100 wt. %. The "blank correction" protocol in the Probe for EPMA software was applied to reduce systematic errors in the analysis of trace Ti (Donovan et al., 2011); the Astimex quartz standard, which has nominal Ti, was analyzed as the blank. The primary standard for Ti was synthetic Astimex rutile, and operating conditions of 20 (for some 15) kV, 20 nA, and 10 s on peak and 5 s on each background were used for standardization. Secondary standards with trace Ti were analyzed to ensure accuracy, including Shandong smoky quartz (reported Ti content of 57 ± 4 ppm from Audétat et al., 2014), a collection of synthetic glasses produced at MUN doped with various trace elements (J. M. Hanchar, unpublished data), and a collection of Ti-doped synthetic glasses produced at the University of Edinburgh (J. Craven). Seventy analyses of the Shandong smoky quartz collected over the course of this research gave an average of 54 ppm Ti, with a standard deviation of 4 ppm (1 σ) for this population (see Appendix 2).

Zirconium in rutile was also analyzed at MUN using the EPMA, with operating conditions of 20 kV, 200 nA, 240 s counting time on peak and 120 s on each background. A single spectrometer measured Zr with a PETL crystal, and analytical uncertainty ranged from ± 12 to 17 ppm (1 σ) with an MDL of 159 ppm. Synthetic ZrO_2 (J. M.

Hanchar collection) was the primary standard for Zr, and standardization was carried out at 20 kV, 20 nA, 10 s on peak and 5 s on each background. For rutile analysis, TiO_2 was fixed at 100 wt. %.

2.3 Mineralogy and microstructures

All five samples contain garnet porphyroblasts, kyanite or sillimanite, biotite, plagioclase, K-feldspar, and quartz (Fig. 2.1). Four are high-*P*, kyanite-bearing granulites that were previously described by Indares & Dunning (2001), Jordan et al. (2006), Indares et al. (2008), Lasalle & Indares (2014), and Kendrick & Indares (in press); one is a mid-*P* granulite containing sillimanite and was described by Lasalle & Indares (2014). Rutile and zircon are present in all samples, both in the groundmass and within garnet porphyroblasts, and the sillimanite-bearing sample additionally contains ilmenite. These minor phases are distinguished in the SEM maps in Fig. 2.1, however they are too small to be clearly visible at the scale of the figure.

Sample 100 comprises garnet porphyroblasts in a groundmass containing biotite, plagioclase, K-feldspar, quartz, and scarce kyanite, with prominent quartz ribbons (Fig. 2.1a). The latter are composed of several large, variably elongated (up to 4 mm long) quartz crystals exhibiting weak undulose extinction (Fig. 2.2a). The SEM mineral map of the thin section reveals a heterogeneous distribution of feldspar; plagioclase is concentrated in plagioclase + biotite ± kyanite ± quartz bands, whereas K-feldspar typically forms clusters with interstitial quartz. Patches of muscovite are also present,

associated with garnet or K-feldspar clusters. Rutile is distributed randomly in the groundmass and as inclusions in garnet, and zircon is present throughout the thin section.

Sample 244 contains abundant elongate garnet and kyanite porphyroblasts, which are aligned in a homogeneous biotite + plagioclase + K-feldspar + quartz groundmass (Fig. 2.1b). Some garnet crystals contain abundant inclusions of kyanite parallel to their long axes, suggesting that the garnet are pseudomorphs after former kyanite. Rutile, apatite, and less abundant zircon are minor phases throughout the groundmass and as inclusions in garnet.

Sample 320 comprises garnet, kyanite, and K-feldspar porphyroblasts in a relatively homogeneous groundmass of biotite + plagioclase + K-feldspar + quartz (Fig. 2.1c). Rutile is present mainly as inclusions in garnet and scarcely in the groundmass, along with zircon.

The most heterogeneous of the samples examined, sample 107b features aluminous domains comprising kyanite and garnet porphyroblasts along with partly recrystallised quartz ribbons made of several large quartz grains (each up to 5 mm long; Fig. 2.2b) in a K-feldspar-dominated groundmass (Fig. 2.1d). Kyanite crystals are separated from quartz by successive rims of plagioclase and K-feldspar. Rutile is mainly in aluminous domains in association with biotite and garnet, however several grains are dispersed in the quartzofeldspathic groundmass. Zircon is present as a minor phase throughout the sample.

Sample HJ60b features xenomorphic to sub-idioblastic garnet porphyroblasts in a groundmass consisting of a biotite + sillimanite (+ quartz) 'network' interstitial to K-feldspar + quartz + plagioclase clusters (Fig. 2.1e). Rutile associated with quartzofeldspathic domains or as inclusions in garnet appears stable, however where it is associated with the biotite + sillimanite network, rutile is partly replaced by ilmenite. Sulphides, graphite, and zircon are distributed throughout the sample.

In all samples, the rims of garnet porphyroblasts are variably replaced by biotite ± plagioclase ± aluminosilicate.

2.3.1 Evidence of partial melting

Each sample exhibits evidence of partial melting during metamorphism, with several features involving quartz indicative of the former presence of melt. Garnet in samples 100, 244, 320, and HJ60b contains polyphase inclusions comprising resorbed quartz or aluminosilicate surrounded by a pool of optically continuous plagioclase or K-feldspar (Fig. 2.2c), interpreted to have replaced former melt (Indares & Dunning, 2001; Jordan et al., 2006; Lasalle & Indares, 2014). Similarly, pods of skeletal kyanite surrounded by quartz found between adjacent garnet porphyroblasts in samples 320 and 244 (Fig. 2.2d) have been inferred to represent resorbed kyanite trapped with former melt (Indares & Dunning, 2001). In sample 320, one kyanite porphyroblast has thin, elongate overgrowths intergrown with quartz (Fig. 2.2e), which have been interpreted to have formed during melt crystallisation (Kendrick & Indares, in press). Pseudomorphs after melt were also identified as thin rims or small pools of quartz around biotite and aluminosilicate, and as plagioclase films associated with garnet (Fig. 2.2f and g; samples

HJ60b, 320, and 244), plagioclase and K-feldspar rims separating kyanite from quartz ribbons (Fig. 2.2h; sample 107b) and patches of quartz interstitial between K-feldspar crystals (samples 100 and 244). Such features were previously described by Holness & Sawyer (2008) in samples from other natural settings. In addition, symplectic intergrowths of biotite + quartz were found in sample HJ60b, and such features have been inferred by Waters (2001) to form during melt crystallisation; Ashworth (1972) also attributed similar muscovite + quartz symplectites to melt crystallisation. Finally, patches of plagioclase intergrown with quartz are found in samples HJ60b, 100, 244, and 320 and appear to be retrograde, although their relation to former partial melt is unclear.

2.3.2 Interpretation

The assemblages and textures observed in these rocks are indicative of dehydration melting of biotite, which proceeded by a quartz-consuming continuous reaction of the type

Biotite + Al-silicate ± Plagioclase + Quartz = Garnet + K-feldspar + Melt

in the NCKFMASH system, following dehydration melting of muscovite. Variable replacement of garnet by biotite ± plagioclase ± aluminosilicate in each sample suggests retrogression and melt crystallisation within the multivariant *P–T* field of biotite dehydration melting (Jordan et al., 2006; Indares et al., 2008; Lasalle & Indares, 2014; Kendrick & Indares, in press). Preservation of the peak assemblage and the scarcity of retrograde muscovite in these rocks, which is present only in sample 100, is consistent

with the loss of a fraction of the anatectic melt during metamorphism (Spear et al., 1999; White & Powell, 2002).

In the kyanite-bearing samples, rutile is the only Ti-bearing oxide phase; however, both rutile and ilmenite are present in the sillimanite-bearing sample HJ60b. Rutile can be produced during the prograde portion of metamorphism by the release of Ti upon breakdown of biotite during biotite dehydration melting, whereas the replacement of rutile by ilmenite in sample HJ60b suggests that ilmenite formed during retrogression. The presence of rutile in the kyanite-bearing samples suggests that these rocks were saturated with respect to TiO_2 during metamorphism, and the persistence of rutile (variably replaced by retrograde ilmenite) in the sillimanite-bearing sample HJ60b, may indicate that this sample too remained saturated with respect to TiO_2. Additionally, all samples contain quartz and zircon, which is inferred to buffer the Zr content of rutile (Zack et al., 2004).

2.4 Quartz textures and Ti content

2.4.1 General features

Most quartz in the samples are small, rounded grains throughout the groundmass, all with a resorbed appearance. Samples 100 and 107b additionally contain partly recrystallised quartz ribbons, also with resorbed edges. These two populations are therefore inferred to have been present during the prograde portion of metamorphism, and partly consumed during anatexis – these will collectively be referred to as 'prograde

quartz'. In contrast, quartz found in films, pools, or other settings linked to melt crystallisation are interpreted to have formed during retrogression in the suprasolidus *P–T* range, and will be referred to here as 'retrograde quartz'. In all samples, the CL maps of prograde quartz define complex patterns including crosscutting linear features, in contrast to the comparatively simple appearance of retrograde quartz.

The intensity of the ~ 430 nm (blue) emission correlates well with the Ti content, as has been previously reported (Müller et al., 2002; Leeman et al., 2012); however, the intensity also fluctuated slightly but systematically with the c-axis orientation of the quartz grains. Grains with c-axes perpendicular or near perpendicular to the thin section plane (determined by optical microscopy) typically emitted weaker blue CL than crystals with similar Ti content and a different orientation (Fig. 2.3a). Walderhaug & Rykkje (2000) also documented the effect of quartz orientation on CL emissions, in that case in terms of observed CL colours. In general, intensity maps of the blue emission were considered here to approximate Ti-in-quartz maps and were used to guide analysis, although in a few cases, quartz was analysed without a map in the interest of time. Results are presented in box and whisker plots in Fig. 2.4, and Figs 2.5–2.9 show false-colour, blue CL intensity maps of quartz.

2.4.1.1 Biotite secondary fluorescence

An important factor that must be considered when analysing Ti in quartz by EPMA is the possibility of secondary fluorescence from nearby Ti-rich phases adding spurious Ti to the analysis. Wark & Watson (2006) documented this effect by showing that false Ti can be detected in quartz up to 150 μm from rutile, with Ti increasing

exponentially with decreasing distance from rutile. Simulations by Fournelle (2007) showed that EPMA analyses of trace Ti in zircon near rutile or ilmenite, or even zircon mounted in a Ti-bearing glass are all susceptible to secondary fluorescence. Although care was taken in this study to avoid analysing quartz near rutile, biotite also contains significant Ti and is therefore a potential source of secondary fluorescence.

To test this hypothesis, analyses were collected along a linear traverse orthogonal to the biotite-quartz interface of a quartz grain that appears homogeneous in CL in sample 100 (Fig. 2.3a). The analyses were carried out at 20 kV in order for the results to be comparable to the majority of our data. The results (Fig. 2.3b) show that trace Ti in quartz increases exponentially with decreasing distance from biotite, beginning at ~ 50 μm from the interface. This interface appears to be nearly perpendicular to the plane of the thin section (determined by optical microscopy), suggesting that secondary fluorescence is the cause of the increased Ti rather than direct sampling of biotite beneath the surface. Although the effect is not as dramatic as secondary fluorescence of rutile, which can add hundreds of ppm of Ti to the analysis (Wark & Watson, 2006), the several tens of extra ppm found here could result in outlying data. In samples 244 and 320, remarkably high Ti contents were obtained from retrograde quartz associated with biotite, and several analyses of prograde quartz close to biotite in samples 100 and HJ60b are also relatively high, in some cases contrary to the CL map. Some of the retrograde quartz pools associated with biotite are < 100 μm wide, necessitating analyses < 50 μm from biotite, where some false Ti, caused by secondary fluorescence, could have been measured, which in turn could lead to inaccuracies in the calculated temperatures. Although it may

be possible that quartz associated with biotite is indeed more Ti-rich, we cannot rule out the possibility of secondary fluorescence affecting our analyses, and therefore we interpret Ti values measured near (< 50 μm) biotite with caution.

2.4.2 Sample 100

In sample 100, prograde quartz comprises variably recrystallised quartz ribbons (~ 1 mm wide) and small groundmass grains (up to 300 μm) typically associated with plagioclase + biotite + kyanite domains. The CL intensity maps of prograde quartz in the sample show variable patterns; they may be patchy or zoned toward weaker intensity at the rims (Fig. 2.5a); quartz ribbons are typically more homogeneous in CL maps than the discrete quartz grains. Retrograde quartz is represented by patches or overgrowths on prograde quartz (Fig. 2.5b) filling interstices in K-feldspar clusters, and is commonly associated with muscovite (Fig. 2.5c). The CL intensity of this quartz may decrease toward the rims or may be very weak overall with straight, sharp features reminiscent of igneous growth zoning (Fig. 2.5b).

Trace Ti in quartz in sample 100 ranges from below MDL to 111 ppm, with 196 total analyses (Fig. 2.4a). Small prograde grains have the highest Ti contents and the largest range, with nearly all analyses between 10 and 70 ppm Ti and rarely higher values of 80 ± 3 (from two separate grains), 90 ± 2, and 111 ± 2 ppm. These maximum values were measured in grains up to 100 μm in diameter, mainly in contact with plagioclase, biotite, or K-feldspar. Prograde quartz ribbons have a distinctly narrower range with generally lower overall values, typically from below MDL to ~ 30 ppm with outliers at 39 ± 3 and 47 ppm ± 3 ppm. Retrograde interstitial quartz ranges from below MDL to

nearly 50 ppm, with the majority below 30 ppm, based on 16 analyses. Interstitial quartz associated with muscovite showed very weak CL, indicating low Ti (< 20 ppm).

2.4.3 Sample 244

In sample 244, relatively large prograde grains (up to 1 mm; Fig. 2.6a) are common in the groundmass and retrograde quartz includes quartz + plagioclase intergrowths (Fig. 2.6b), quartz films or pools around biotite and kyanite, and interstitial quartz between K-feldspar grains. The CL intensity of retrograde quartz is similar to that of prograde grains or weaker, and may decrease toward the rims.

Twenty-two analyses of prograde quartz in this sample revealed a Ti range of ~ 35 to nearly 70 ppm (Fig. 2.4b). The range for retrograde quartz partly overlaps that of prograde quartz, with ~ 20 to 50 ppm Ti from 17 analyses. Notably, retrograde quartz pools associated with biotite gave outlying data, with one 75 ± 2 ppm and two 112 ± 2 ppm Ti analyses.

2.4.4 Sample 320

Quartz in sample 320 comprises large prograde quartz grains (up to 1 mm; Fig. 2.7a) with several types of retrograde quartz: quartz + plagioclase intergrowths, a quartz + kyanite intergrowth at the edges of a large kyanite grain (Fig. 2.2e), quartz pools or films around biotite (Fig. 2.7b) and kyanite, and kyanite + quartz pods between adjacent garnet porphyroblasts (Figs. 2.2b, 2.7c). Prograde quartz typically displays zonation toward rims with weaker CL intensity.

A range of ~ 10 to nearly 55 ppm Ti was measured in prograde quartz in this sample, resulting from 22 analyses (Fig. 2.4c). Retrograde quartz from all settings collectively gave a larger range, from ~ 15 to nearly 90 ppm Ti from 33 analyses. Many of the upper quartile results (> ~ 55 ppm) were obtained from quartz associated with biotite.

2.4.5 Sample 107b

All quartz in sample 107b appears prograde, in the form of quartz ribbons (up to 2 mm wide). These may be zoned with a more intense CL core and weaker rims (Fig. 2.8a). The CL images revealed distinct quartz overgrowths on some ribbons (Fig. 2.8a and b), typically in contact with K-feldspar or plagioclase. These overgrowths are distinguished in CL maps by their very weak CL intensity, lack of cross-cutting linear features, and straight, sharp patterns, and are interpreted to be retrograde.

Titanium contents in quartz in this sample are the most distinctly bimodal (Fig. 2.4d). Based on 23 analyses, Ti in quartz ribbons range from ~ 25 to nearly 50 ppm, with consistently ~ 45 ± 3 ppm Ti in the cores and all lower values measured at the rims. Ten analyses of retrograde quartz overgrowths with weak CL were all at or below MDL.

2.4.6 Sample HJ60b

Quartz in sample HJ60b comprises relatively large prograde quartz grains (up to 1 mm) throughout the groundmass (Fig. 2.9a) and as inclusions in garnet, and retrograde quartz is represented by pools or films around sillimanite (Fig. 2.9b), symplectic quartz + biotite intergrowths (Fig. 2.9c), and quartz + plagioclase intergrowths. Both types show

zonation from cores with high CL intensity to lower intensity rims; prograde crystals display stronger zonation and retrograde quartz typically has weaker CL overall.

In this sample, the cores and rims of over 60 prograde grains were analysed, giving a range of ~ 20 to 165 ppm Ti (outlier at 177 ± 2 ppm; Fig. 2.4e); the highest contents (those > 100 ppm) were typically obtained from the cores. The large range in values is the result of both strong Ti zonation in many grains and variation among grains. Thirteen analyses from retrograde quartz range from ~ 40 to 90 ppm, and the consistent CL intensity in this type of quartz indicates that this range is representative.

2.4.7 Summary and discussion

In samples 100, HJ60b, 244, and 107b, prograde quartz has a higher average Ti content than the retrograde quartz. Prograde quartz is the most Ti-rich in sample HJ60b, with sample 100 reaching the second highest values, and sample 244 having somewhat higher concentrations than samples 320 and 107b, which are comparable. Quartz ribbons in sample 100, however, have the lowest average Ti concentration of all prograde quartz if they are considered as a separate population. The most Ti-poor retrograde quartz is found in samples 100 and 107b, where it forms overgrowths on existing quartz or interstitial patches identified by CL mapping (Figs 2.5b and c and 2.8a and b), and are generally surrounded by K-feldspar. Retrograde quartz in other settings, such as pools or films associated with aluminosilicate or biotite and intergrowths with plagioclase yielded Ti contents lower than or somewhat overlapping with those of prograde quartz. Maximum Ti contents of retrograde quartz typically came from analyses of quartz pools

associated with biotite (e.g., Fig. 2.7b). On average, retrograde quartz in sample HJ60b is more Ti-rich than the other samples.

According to the results of diffusion experiments by Cherniak et al. (2007), the diffusion distance of Ti through the quartz structure over 1 My would be on the order of 500 μm at 800°C. Given that these samples are interpreted to have reached temperatures > 800°C in a tectonic setting characterised by protracted regional metamorphism, prograde quartz could have feasibly re-equilibrated to Ti concentrations reflective of peak *P–T* conditions. Alternatively, the quartz could have failed to equilibrate and thus would retain a Ti value inherited from an earlier part of the *P–T* history; this would be expected for particularly large grains, such as the quartz ribbons. Deformation is another important factor that could affect the Ti content of the prograde grains, as quartz undergoing dynamic recrystallisation may re-equilibrate to the Ti concentration expected for the temperature of deformation (Grujic et al., 2011; Korchinski et al., 2012). The samples investigated here do not exhibit evidence for deformation post-peak *P–T*, as delicate features such as former melt films and pools are preserved in the groundmass. The recrystallisation of quartz ribbons in samples 100 and 107b and the Ti contents of this quartz are therefore interpreted to be related to prograde deformation. Retrograde quartz in all samples, given the evidence that it crystallised from melt, is expected to record conditions within the *P–T* range of melt crystallisation.

2.5 Zr contents of rutile

Rutile in different textural settings in each sample was targeted for Zr-in-rutile thermometry. Rutile is present as inclusions in garnet and in the groundmass in each thin section, and where possible, multiple measurements were taken from individual grains. Results are presented in box and whisker plots in Fig. 2.10.

In sample 100, the Zr contents of groundmass grains and inclusions in garnet are comparable, with ranges of 283 ± 12 to 544 ± 13 ppm and 437 ± 13 to 649 ± 13 ppm respectively (Fig. 2.10a). Small crystals are homogeneous with respect to Zr, whereas larger grains (> 70 μm) exhibit weakly decreasing Zr toward their rims. The most Zr-poor rutile analysed was surrounded mainly by biotite. Small rutile inclusions in garnet in sample 244 (Fig. 2.11a) are enriched in Zr relative to groundmass crystals, with ranges of 1095 ± 14 to 1751 ± 16 ppm and 522 ± 13 to 1527 ± 16 ppm respectively (Fig. 2.10b). Groundmass rutile is typically weakly zoned with higher Zr cores and lower Zr rims; minimum values were measured in a grain associated with biotite and quartz films. In contrast to the other samples, small rutile inclusions (≤ 100 μm) in garnet are abundant in sample 320 and groundmass rutile is scarce. The two populations have distinct Zr contents, with 435 ± 13 to 1038 ± 14 ppm in rutile inclusions in garnet and 175 ± 12 to 242 ± 12 ppm in groundmass grains (Fig. 2.10c). Notably, all four groundmass rutile grains found in sample 320 have irregular shapes and are separated from adjacent biotite by a film of quartz (Fig. 2.11b). In sample 107b, the Zr contents of each type of rutile are distinct, with 1343 ± 15 to 1364 ± 15 ppm from a rutile inclusion in garnet and 450 ± 13 to 1126 ± 15 ppm in groundmass rutile (Fig. 2.10d). However, as only one rutile inclusion in garnet was analyzed, the narrow range of Zr values may not be

representative. Groundmass grains typically have weak zonation, with higher Zr in cores than rims. Rutile in sample HJ60b gave a broad range of Zr values, from below MDL to 2161 ± 17 ppm in groundmass grains and from 1743 ± 16 to 2181 ± 17 ppm in inclusions in garnet (Fig. 2.10e). Rutile inclusions in garnet are few, and thus only two were analyzed. Minimum Zr-in-rutile values from groundmass grains were measured in rutile partly replaced by ilmenite in the biotite + sillimanite network (< MDL to 470 ± 13 ppm; Fig. 2.11c); rutile elsewhere in the groundmass is more Zr-rich (1228 ± 15 to 2161 ± 17 ppm; Fig. 2.11d) and may be weakly zoned with slightly Zr-depleted rims.

2.5.1 Summary and interpretation

In all samples, rutile inclusions in garnet are generally more Zr-rich than groundmass rutile. These grains may have been trapped within garnet produced during biotite dehydration melting, the same reaction that could have also produced rutile in these rocks; therefore, these rutile grains could record prograde or near-peak temperatures. However, some garnet may have been produced before anatexis, and thus the rutile inclusions in those grains would record an earlier portion of the prograde history. The comparatively low Zr in groundmass rutile may be the result of Zr resetting at lower temperatures, as rutile partly replaced by ilmenite in sample HJ60b (Fig. 2.11c) and the irregularly shaped rutile associated with biotite ± quartz films in samples 320 (Fig. 2.11b), 244, and 100, have especially low Zr concentrations. One ilmenite + rutile grain in sample HJ60b is associated with interstitial zircon (Fig. 2.11c), consistent with rutile releasing Zr during retrogression. In contrast, maximum groundmass Zr-in-rutile

values in all samples were found in grains not associated with retrograde microstructures (e.g., Fig. 2.11d).

2.6 Thermobarometry

2.6.1 Pseudosections and P–T paths

A *P–T* framework for each sample was previously developed by phase equilibria modelling (Indares et al., 2008; Lasalle & Indares, 2014; Kendrick & Indares, in press), and each phase diagram has been reproduced here to evaluate the accuracy of the Ti-in-quartz and Zr-in-rutile results. These phase diagrams, which are valid only for the particular bulk compositions for which they were constructed, are referred to here using the informal term 'pseudosections'. For all samples, pseudosections were calculated in the NCKFMASHTO system using the THERMOCALC software (version 3.33, updated from Powell & Holland, 1988) with the tcds55 dataset of Holland & Powell (1998; updated in 2003). Activity models used were as follows: White et al. (2007) for garnet, biotite, and melt; Holland & Powell (2003) for plagioclase and K-feldspar; and Coggon & Holland (2002) for muscovite. Bulk compositions (Table 1) used for modelling are those of Indares et al. (2008) and Lasalle & Indares (2014). The value of O is set to a minimal 0.05 for all samples to reflect the presence of rutile in the high-*P* samples and the appearance of ilmenite as only a retrograde phase in the mid-*P* sample. Ilmenite has been excluded from the pseudosections, as the value of O for the samples has not been independently constrained; therefore, the modelled *P–T* extent of ilmenite stability has

little meaning. Abbreviations used are grt (garnet), bt (biotite), liq (liquid), pl (plagioclase), ksp (K-feldspar), qtz (quartz), ky (kyanite), sil (sillimanite), ms (muscovite), opx (orthopyroxene), crd (cordierite), ilm (ilmenite), rt (rutile).

Each pseudosection features a similar set of topologies, most importantly including the field in which the assemblage grt–bt–ky/sil–pl–ksp–liq–qtz–rt is stable, referred to here as Field I (Fig. 2.12, Field I shown in purple). This is the field in which continuous dehydration melting of biotite proceeds with increasing *T*; observed mineral assemblages and textures indicate that the near-peak prograde and retrograde *P–T* paths of these samples lie within Field I. In all pseudosections, Field I is limited at high *T* by the biotite-out boundary and at low *T* by the solidus. In pseudosections for samples 107b, 244, and 320 (Fig. 2.12b–d), the appearance of muscovite and disappearance of plagioclase mark the high-*P* limit. Field I in the sample 100 pseudosection (Fig. 2.12a) has notable differences from the other kyanite-bearing samples, including kyanite-out boundaries at high *T* and high *P*, and a muscovite-in boundary extending to lower *P*. In the pseudosection for sillimanite-bearing sample HJ60b (Fig. 2.12e), a cordierite-in boundary marks the low *P* limit of Field I. Isopleths of quartz proportions calculated within Field I for each sample have a steep d*P*/d*T*, and a maximum of ~ 4 to ~ 8 modal % quartz is predicted to be produced by retrogression within this field.

P–T paths in Field I for each sample were determined by Indares et al. (2008) and Lasalle & Indares (2014) by comparing relevant measured concentrations of X_{Fe} and X_{grs} of garnet with calculated isopleths in the pseudosections. In addition, the presence of appreciable retrograde kyanite in samples 100, 244, and 320 suggests that peak *T* is near

(or even beyond) the biotite-out boundary (Kendrick & Indares, in press). Based on X_{grs}, samples 107b, 244, and 320 record evidence for ~ 2 to ~ 4 kbar of decompression (Fig. 2.12b–d), in contrast to ~ 1 kbar and ~ 1–1.5 kbar of decompression for samples 100 and HJ60b respectively (Fig. 2.12a and e). The *P–T* conditions of melt crystallisation are best constrained for sample 100 due to the presence of retrograde muscovite, as the appearance of muscovite at the solidus is predicted in a small *P–T* window (Fig. 2.12a). For sample HJ60b, the addition of retrograde ilmenite to the assemblage cannot be used to accurately constrain conditions of melt crystallisation without a well-constrained value for O. Based on the *P–T* paths estimated for the samples, 3–5 modal % quartz is predicted to be produced during retrogression, consistent with petrographic observations.

As the pseudosections can adequately account for the mineral assemblages, textures, and mineral chemistries observed or measured in these samples, the interpreted *P–T* paths are inferred to be geologically reasonable (Indares et al., 2008; Lasalle & Indares, 2014). Although the absolute position of the topologies in *P–T* space is subject to uncertainty (Powell & Holland, 1988; Palin et al., 2016), the general *P–T* range of Field I and the shape of the *P–T* path are considered to be reliable.

2.6.2 Ti-in-quartz thermobarometry

Before evaluating the results, an appropriate calibration of the Ti-in-quartz thermobarometer must be chosen. Generally, the calibrations are based on experiments where quartz and rutile were precipitated from fluid to evaluate the Ti uptake of quartz in a TiO_2-saturated environment. The two most recent calibrations, by Thomas et al. (2010) and Huang & Audétat (2012), have both taken into account the important *P* dependence

of Ti substitution into quartz as well as *T*, building upon the approach of Wark & Watson (2006), where *P* was held constant. The different experimental approaches of Thomas et al. (2010) and Huang & Audétat (2012), however, have resulted in substantially different mathematical expressions relating Ti content to *P* and *T*. Here, we prefer the calibration of Thomas et al. (2010), as their experiments provide more convincing evidence of equilibrium between quartz and rutile, or a_{TiO2} of 1.0 (Thomas et al., 2015). Furthermore, the experiments of Huang & Audétat (2012) were run at a maximum of 10 kbar, considerably lower than the peak P of our kyanite-bearing samples (~ 13-16 kbar), whereas Thomas et al. (2010) ran experiments up to 20 kbar. A comparison of the two calibrations in the context of our samples and Ti-in-quartz results is provided in Appendix 10.

Each pseudosection was overlain with isopleths of Ti-in-quartz (Fig. 2.13) calculated using the equation of Thomas et al. (2010),

$$RTlnX_{TiO_2}^{quartz} = -60952 + 1.520 \times T(K) - 1741 \times P(kbar) + RTlna_{TiO_2},$$

which relates Ti concentration in quartz ($X_{TiO_2}^{quartz}$) to *P* and *T*; the a_{TiO2} value was set as 1.0. These isopleths are linear in *P*–*T* space with a positive d*P*/d*T*, and become more closely spaced with slightly shallower d*P*/d*T* as Ti concentration increases with decreasing *P* and increasing *T*. Field I falls in a range of ~ 70 to ~ 180 ppm Ti in quartz in the pseudosection for sample 100, ~ 50 to ~ 200 ppm Ti in those for samples 107b, 244, and 320, and ~ 160 to > 300 ppm Ti in the pseudosection for sample HJ60b. Measured Ti

concentrations of prograde and retrograde quartz were evaluated by comparison of Ti-in-quartz isopleths with the interpreted *P–T* paths of the rocks.

2.6.2.1 Samples 100 and 107b

For sample 100, Ti isopleths corresponding to the high end of the Ti range measured in prograde quartz cross Field I and some overlap with the interpreted near-peak *P–T* path (Fig. 2.13a); specifically, a range from 70 ppm Ti to the maximum measurement of 111 ± 2 ppm. These relatively high values are consistent with the relatively low peak *P* of sample 100 compared to the other kyanite-bearing samples. In contrast, the isopleths corresponding to the Ti concentrations of quartz ribbons in sample 107b (up to 49 ± 3 ppm Ti) only cross a small portion of Field I at high *P*, several kbar above the inferred peak *P* (Fig. 2.13b).

Retrograde quartz in these two samples share similar features, as both are interstitial patches and/or overgrowths of very Ti-poor quartz. The isopleths of the Ti concentrations of this quartz, < MDL to ~ 20 ppm, fall at much lower *T* and/or higher *P* than Field I. In the pseudosection for sample 100, where conditions of melt crystallisation are well-constrained by the retrograde muscovite-in boundary, there is a large discrepancy between expected and measured Ti contents. Quartz intergrown with retrograde muscovite (Fig. 2.5c) exhibits very weak blue CL intensity indicating < 20 ppm Ti, in sharp contrast with the 90 to 100 ppm Ti expected from Ti-in-quartz thermobarometry at the muscovite-in boundary (Fig. 2.13a).

2.6.2.2 Samples 244 and 320

Most Ti isopleths corresponding to the Ti concentrations of prograde quartz in samples 244 and 320 (up to the maximum values of 68 ± 2 and 53 ± 2 ppm respectively) fall at higher *P*/lower *T* than peak conditions interpreted for these samples (Fig. 2.13c and d). The isopleths of the highest concentrations from retrograde quartz (up to 87 ± 2 ppm in 320 and up to 112 ± 2 ppm in sample 244), however, overlap with the near-peak *P–T* conditions of these samples. Of note is the microstructural position of this Ti-rich retrograde quartz – in both samples, all Ti values consistent with near-peak *P–T* conditions were measured in quartz associated with biotite, save for a single analysis associated with kyanite in sample 320.

2.6.2.3 Sample HJ60b

Higher overall Ti-in-quartz concentrations are consistent with the lower peak *P* of sample HJ60b compared to the kyanite-bearing samples (Fig. 2.13e). Isopleths of the four highest Ti concentrations of prograde quartz, with a range of 155 ± 2 to 177 ± 2 ppm Ti, overlap with a portion of the interpreted prograde *P–T* path of this sample. Three of these analyses were measuring cores of prograde grains and one was taken at a rim near biotite. The isopleths corresponding to the range of Ti values from retrograde quartz (38 ± 2 to 92 ± 2 ppm) fall at significantly lower *T* and/or higher *P* than Field I.

2.6.3 Zr-in-rutile thermometry

Isopleths of Zr-in-rutile were calculated for the pseudosections (Fig. 2.14) using the experimentally-derived equation of Tomkins et al. (2007),

$$T(°C) = \frac{83.9 + 0.410 \times P(kbar)}{0.1428 - RlnZr(ppm)} - 273,$$

valid for the stability field of α-quartz. The Tomkins et al. (2007) calibration was chosen because it incorporates the effect of *P* on Zr-in-rutile. The difference between the α-quartz and β-quartz equations is minor and the transition transects Field I, hence the chosen equation is sufficient for evaluating the results. The Zr-in-rutile isopleths have a steeper d*P*/d*T* than Ti-in-quartz isopleths, and also become more closely spaced with a slightly shallower d*P*/d*T* as Zr increases with increasing *T*. Field I generally overlaps with a range between 1000-1500 and 2000-3000 ppm Zr.

Based on the isopleths, most of the Zr concentrations measured in these samples are consistent with temperatures much lower than the range of Field I. Three rutile grains within garnet in sample 244 gave a range of 1687 ± 16 to 1751 ± 16 ppm Zr, and the isopleths of these values cross a small portion of the low *T* side of Field I (Fig. 2.14c). Results from sample HJ60b show the best agreement between Zr-in-rutile and phase equilibria modelling. Three groundmass crystals and both inclusions in garnet collectively range from 1700 ± 16 to 2181 ± 17 ppm Zr, and the corresponding isopleths overlap with the inferred *P–T* path of this sample (Fig. 2.14e). Rutile in HJ60b is the most Zr-rich of all samples, which is consistent with the minor *P*-dependence of Zr-in-rutile inferred by Tomkins et al. (2007).

2.7 Discussion

2.7.1 Summary and interpretation of results

Cathodoluminescence mapping of quartz in the anatectic rocks investigated not only revealed the Ti distribution within quartz crystals, but also proved to be a valuable tool for distinguishing prograde and retrograde quartz. Although quartz produced by melt crystallisation in some samples crystallised as distinct films or pools visible using a petrographic microscope, this was not true for samples 100 and 107b. Only by CL mapping could the retrograde quartz overgrowths in these samples be identified and their interstitial form made clear (Figs 2.5 and 2.8). For these samples, CL maps provided the context necessary for interpretation of the Ti-in-quartz thermobarometric data. Holness and Sawyer (2008) similarly identified quartz overgrowths as products of melt crystallisation using CL imaging in a quartz-rich migmatite.

Our results have implications for the practicality of using Ti-in-quartz as a complementary tool to phase equilibria models for assessing the *P–T* paths of anatectic aluminous granulites. Ideally, Ti-in-quartz could be used to add additional constraints to peak *P–T* conditions and the *P–T* range of melt crystallisation. However, for most Ti concentrations measured in prograde quartz, the corresponding Ti-in-quartz isopleths occupy a *P–T* field at higher *P*/lower *T* than Field I. In samples 100 and HJ60b, which record the lowest peak *P*, the highest Ti concentrations of prograde quartz overlap with the interpreted *P–T* path in Field I; for the other samples, there is only minor overlap with Field I at a couple of kbar higher than the estimated peak *P*. Therefore, in some cases, prograde quartz may have been capable of re-equilibrating at high *T*. However, over 100 analyses in each of samples 100 and HJ60b were required for these results, and combined

with CL mapping of each quartz grain prior to analysis, this process can be time consuming. In addition, uncertainty is associated with the positions of the topologies in the pseudosections, and therefore the degree of overlap between the Ti-in-quartz isopleths and Field I is also subject to uncertainty. However, the large range of Ti concentrations measured in prograde quartz, which reaches very low values in some samples, suggests that many of these crystals have retained Ti concentrations inherited from the earlier prograde history of these rocks, or even their detrital source. This is consistent with the complex patterns of Ti distribution revealed by CL in some prograde grains (e.g., Fig. 2.5a, b) and the narrow ranges of low Ti values measured in quartz ribbons in samples 100 and 107b, as quartz ribbons within a thin section likely formed at the same time with similar Ti content. Given that quartz is predicted to be a reactant in most prograde reactions from amphibolite to granulite facies (Storm & Spear, 2009), the origin of Ti concentrations and distribution within prograde quartz is difficult to interpret. Therefore, although 'low Ti' prograde quartz may record values consistent with some part of the prograde *P–T* path, these are not useful without more context.

Given that there are uncertainties associated with phase equilibria modelling that have not been included in the diagrams in Fig. 2.13, an exact match between *P–T* conditions predicted in the pseudosections and those from Ti-in-quartz thermobarometry may be an unrealistic expectation. However, *P–T* trends inferred from phase equilibria modelling are relatively robust, and should also be recorded by Ti-in-quartz. As all the samples are interpreted to record significant decompression (excluding sample 100), retrograde quartz would be expected to grow at relatively lower pressures and thus

contain higher concentrations of Ti relative to those expected at the thermal peak, based on the strongly *P*-dependent Ti-in-quartz isopleths (Fig. 2.13; Appendix 10). Overall, our data show the opposite trend, with most prograde quartz giving higher Ti values than retrograde quartz; in most cases, the Ti isopleths for retrograde quartz are clearly outside of a geologically reasonable *P–T* field for melt crystallisation (Fig. 2.13). These low Ti-in-quartz values provide strong evidence for $a_{TiO2} < 1.0$, or disequilibrium between quartz and rutile, during melt crystallisation.

According to the interpretation that rutile inclusions in garnet could have been trapped during biotite dehydration melting, the Zr concentrations of these inclusions may be consistent with any part of the prograde *P–T* path within Field I. This is only the case for HJ60b, and rutile from the other samples contains much lower Zr. Some of the rutile may have been included in pre-anatectic garnet, and these therefore may record early prograde temperatures. Moreover, the residual character of the bulk compositions of these samples causes Field I to be restricted to higher *T* in the pseudosections than would be expected during prograde metamorphism (see melt-reintegrated pseudosections of Indares et al., 2008 and Lasalle & Indares, 2014). The rutile in garnet in samples 244 and 107b gave Zr-in-rutile temperatures only slightly lower than the solidus in these pseudosections (Fig. 2.14b and c), which may indeed be realistic prograde temperatures of early stages of biotite dehydration melting.

Although groundmass rutile could have grown or re-equilibrated at peak *T*, Zr concentrations from all samples but HJ60b are consistent with temperatures significantly lower than Field I. The low Zr values, particularly in rutile that became unstable during

retrogression (Fig. 2.11b and c), suggests that the Zr-values of groundmass grains were susceptible to retrograde resetting. However, it may also be possible that both groundmass rutile and inclusions in garnet did not achieve equilibrium with zircon, as even relatively pristine groundmass rutile in sample HJ60b (Fig. 2.11d) failed to record peak conditions, and rutile in samples 100 and 320 is very Zr-poor (Fig. 2.14a and d).

2.7.2 Assessing equilibrium

The presence of rutile is generally considered to buffer the Ti content of quartz, and likewise, coexisting quartz and zircon are thought to buffer Zr-in-rutile. In the experiments done to calibrate these thermobarometers, the relevant phases are typically precipitated together from a saturated fluid to ensure equilibrium among them (Wark & Watson, 2006; Ferry & Watson, 2007; Tomkins et al., 2007; Thomas et al., 2010; Huang & Audétat, 2012). In these relatively simple systems, the textural relationships among the minerals in the run products can provide clear evidence for equilibrium (e.g., Thomas et al., 2015). However, in natural samples, assessing whether equilibrium was achieved in these trace element systems is more complicated, and coexistence of the phases of interest within a thin section may not be sufficient.

2.7.2.1 Ti-in-quartz

The samples investigated here were undergoing biotite dehydration melting at the metamorphic peak; quartz and rutile would need to achieve equilibrium in this environment in order for Ti-in-quartz to record peak *P–T* conditions. The biotite dehydration melting reaction consumes quartz, and, given that Ti solubility in the other

phases produced during melting is relatively low (e.g., melt, garnet; Hayden & Watson, 2007; Ackerson et al., 2017), rutile is likely to be produced as biotite releases Ti (Fig. 2.15a), which is generally considered to ensure $a_{TiO2} = 1.0$. During melt crystallisation, new quartz grows along with new biotite, which would be expected to gain Ti by rutile dissolution. As rutile was found in the groundmass of all samples, it was not completely consumed by retrograde biotite, and was thus present during retrograde quartz production. Despite the production and/or presence of rutile during metamorphism, our results suggest that in most cases, quartz and rutile did not achieve equilibrium. Notably, the low Ti concentrations found in retrograde quartz are incompatible with the reasonably well-constrained *P–T* range of melt crystallisation, and although the transition of rutile to ilmenite in sample HJ60b could suggest that a_{TiO2} was only slightly less than 1.0 (Ghent & Stout, 1984; Ashley & Law, 2015), our results indicate that it was much lower.

Disequilibrium between quartz and rutile could result from several factors, including a small equilibration volume associated with rutile, the lack of a driving force for equilibration, and slow volume diffusion of Ti through the quartz structure (Cherniak et al., 2007), although the latter would not apply to new quartz grown during melt crystallisation. The locally Ti-rich prograde quartz in samples HJ60b and 100 may indicate that Ti saturation was achieved in microdomains near rutile (Fig. 2.15a). Moreover, in sample 107b, Ti-poor quartz ribbons and nearly Ti-free retrograde overgrowths are surrounded by K-feldspar and isolated from aluminous domains (Fig. 2.1d), in which biotite dehydration melting and rutile production were localized. This is in agreement with the experimental work of Bromiley & Hiscock (2016) on grain

boundary diffusion of Ti. Another important factor, particularly during retrogression, may be the activation energy required for exchange between rutile and quartz, as rutile crystals not participating in a reaction may essentially be inert (Fig. 2.15b). This is consistent with the Ti-poor quartz pseudomorphs after melt pockets in sample 100; the K-feldspar clusters that host this quartz are commonly also host to rutile.

2.7.2.2 Zr-in-rutile

For most samples in this study, the Zr concentrations of rutile inclusions in garnet could be compatible with prograde temperatures of garnet growth; however, no groundmass crystals recording peak *T* were found. Locally, retrograde resetting appears to have been important, as rutile associated with retrograde biotite and ilmenite (Fig. 2.11b and c) have particularly low Zr contents. Resetting of Zr-in-rutile during retrogression has been documented in other granulite-facies rocks, aluminous or mafic in composition (e.g., Luvizotto & Zack, 2009; Meyer et al., 2011; Ewing et al., 2013; Mitchell & Harley, 2017), in which rutile contains exsolutions of zircon or is in contact with small zircon grains. In the samples investigated here, rutile showed no exsolution features and was rarely adjacent to zircon; retrograde resetting here appears to have been driven mainly by interaction of rutile with biotite or ilmenite (Fig. 2.15b). The local nature of this feature indicates that resetting likely did not take place in equilibrium with zircon, and thus the grains do not record the temperatures of these retrograde reactions.

In addition to retrograde resetting, it is possible that rutile failed to achieve equilibrium with zircon at peak metamorphic conditions. During anatexis of aluminous rocks, zircon is predicted to at least partially dissolve in order to saturate the anatectic

melt in Zr (Bea & Montero, 1999; Kelsey et al., 2008; Yakymchuk & Brown, 2014). Therefore, during biotite dehydration melting, rutile is expected to grow coeval with zircon dissolution (Fig. 2.15a). If zircon is abundant and not exhausted before peak metamorphic conditions, saturation of both rutile and anatectic melt with respect to Zr should be possible at peak *P–T*. However, for lower than average initial bulk rock concentrations of Zr, solubility modelling suggests that zircon may dissolve completely in anatectic melt at temperatures less than or close to the inferred peak *T* of the samples under investigation here (Kelsey et al., 2008; Yakymchuk & Brown, 2014). If zircon is exhausted during biotite dehydration melting before peak *P–T* conditions, rutile may be undersaturated in Zr as a result. Even with stable zircon at peak *P–T*, equilibrium among all rutile, melt, and zircon at the scale of a thin section may be difficult to achieve, as small zircon and rutile are scattered sparsely and melt extraction may outpace equilibration (Yakymchuk & Brown, 2014). The distribution of zircon grains in the rock is also an important factor, as those included within major phases are less available to melt and rutile than those at grain boundaries (Sawyer, 1999). Kooijman et al. (2012) also argued for undersaturation of Zr in rutile at peak conditions in aluminous granulites despite the presence of zircon, based on the preservation of prograde or earlier Zr zonation in rutile.

2.8 Conclusions

For anatectic aluminous granulites, CL imaging is an indispensable tool for distinguishing quartz that survived prograde melting reactions from new retrograde

quartz. Quartz pseudomorphs after former melt may be cryptic features not obvious or visible by petrographic observation, as we have shown that they may form overgrowths on existing quartz. Without documentation of quartz with the aid of CL, specifically the blue emission, the significance of measured Ti-in-quartz cannot be assessed. With the growing popularity of trace element thermobarometers, testing their utility by applying them to well-characterised samples with previously established *P–T* paths is essential to gain an understanding of the possible limitations of these techniques. Although many features of anatectic aluminous granulites can make them good candidates for Ti-in-quartz in particular, our work suggests that these data should be interpreted with care. The co-existence of the phases required for application of these thermobarometers does not ensure that equilibrium was achieved among them. Despite the presence of rutile in all samples investigated, we have demonstrated unequivocally that quartz crystallised from partial melt in a Ti-undersaturated environment. Similarly, some prograde quartz and possibly rutile did not re-equilibrate to the respective Ti and Zr values expected for the peak *P–T* conditions reached by these rocks. Co-existence of quartz, rutile, and zircon has been traditionally regarded as evidence for equilibrium among these phases during synthesis experiments, however natural systems are more complex and dynamic, and the possibility of disequilibrium must be considered.

Acknowledgements

The authors acknowledge Wanda Aylward for assistance in the EPMA lab and David Grant and Dylan Goudie for assistance with the collection of SEM mineralogical maps.

We are very grateful to John Hanchar (MUN), Andreas Audétat (Bayreuth), and John Craven (Edinburgh) for providing the invaluable secondary Ti standards, and to John Hanchar again for providing the ZrO_2 standard. This research benefitted from fruitful discussions with Roger Mason and John Hanchar. A thorough review of the manuscript by John Hanchar and comments from Roger Mason and Dave Pattison were greatly appreciated. We thank Chiara Groppo and two anonymous reviewers for their formal reviews, which helped to improve the clarity and quality of this paper, and Reto Gieré for editorial handling.

References

Ackerson, M. R., Watson, E. B., Tailby, N. D. & Spear, F. S. (2017). Experimental investigation into the substitution mechanisms and solubility of Ti in garnet. American Mineralogist, 102, 158–172.

Ashley, K. T. & Law, R. D. (2015). Modeling prograde TiO_2 activity and its significance for Ti-in-quartz thermobarometry of pelitic metamorphic rocks. Contributions to Mineralogy and Petrology, 169, 23.

Ashworth, J. R. (1972). Myrmekites of exsolution and replacement origins. Geological Magazine, 109, 45–62.

Audétat, A., Garbe-Schönberg, D., Kronz, A., Pettke, T., Rusk, B., Donovan, J. J. & Lowers, H. A. (2014). Characterisation of a natural quartz crystal as a reference

material for microanalytical determination of Ti, Al, Li, Fe, Mn, Ga and Ge. Geostandards and Geoanalytical Research, 39, 171–184.

Bea, F. & Montero, P. (1999). Behavior of accessory phases and redistribution of Zr, REE, Y, Th, and U during metamorphism and partial melting of metapelites in the lower crust: An example from the Kinzigite Formation of Ivrea-Verbano, NW Italy. Geochimica et Cosmochimica Acta, 63, 1133–1153.

Bromiley, G. D. & Hiscock, M. (2016). Grain boundary diffusion of titanium in polycrystalline quartz and its implications for titanium in quartz (TitaniQ) geothermobarometry. Geochimica et Cosmochimica Acta, 178, 281–290.

Cherniak, D. J., Watson, E. B. & Wark, D. A. (2007). Ti diffusion in quartz. Chemical Geology, 236, 65–74.

Coggon, R. & Holland, T. J. B. (2002). Mixing properties of phengitic micas and revised garnet-phengite thermobarometers. Journal of Metamorphic Geology, 20, 683–696.

Donovan, J. J., Lowers, H. A. & Rusk, B. G. (2011). Improved electron probe microanalysis of trace elements in quartz. American Mineralogist, 96, 274–282.

Ewing, T. A., Hermann, J. & Rubatto, D. (2013). The robustness of the Zr-in-rutile and Ti-in-zircon thermometers during high-temperature metamorphism (Ivrea-Verbano Zone, northern Italy). Contributions to Mineralogy and Petrology, 165, 757–779.

Ferry, J. M. & Watson, E. B. (2007). New thermodynamic models and revised calibrations for the Ti-in-zircon and Zr-in-rutile thermometers. Contributions to Mineralogy and Petrology, 154, 429–437.

Fournelle, J. H. (2007). The problem of secondary fluorescence in EPMA in the application of the Ti-in-zircon geothermometer and the utility of PENEPMA Monte Carlo program. Microscopy and Microanalysis, 13, 1390–1391.

Ghent, E. D. & Stout, M. Z. (1984). TiO_2 activity in metamorphosed pelitic and basic rocks: Principles and applications to metamorphism in southeastern Canadian Cordillera. Contributions to Mineralogy and Petrology, 86, 248–255.

Hayden, L. A. & Watson, E. B. (2007). Rutile saturation in hydrous siliceous melts and its bearing on Ti-thermometry of quartz and zircon. Earth and Planetary Science Letters 258, 561–568.

Holland, T. J. B. & Powell, R. (1998). An internally consistent thermodynamic data set for phases of petrological interest. Journal of Metamorphic Geology, 16, 309–343.

Holland, T. J. B. & Powell, R. (2003). Activity-composition relations for phases in petrological calculations: An asymmetric multicomponent formulation. Contributions to Mineralogy and Petrology, 145, 492–501.

Holness, M. B. & Sawyer, E. W. (2008). On the pseudomorphing of melt-filled pores during the crystallization of migmatites. Journal of Petrology, 49, 1343–1363.

Huang, R. & Audétat, A. (2012). The titanium-in-quartz (TitaniQ) thermobarometer: A critical examination and re-calibration. Geochimica et Cosmochimica Acta, 84, 75–89.

Indares, A. & Dunning, G. (2001). Partial melting of high-P–T metapelites from the Tshenukutish Terrane (Grenville Province): Petrography and U–Pb geochronology. Journal of Petrology, 42, 1547–1565.

Indares, A., White, R. W. & Powell, R. (2008). Phase equilibria modelling of kyanite-bearing anatectic paragneisses from the central Grenville Province. Journal of Metamorphic Geology, 26, 815–836.

Jordan, S. L., Indares, A. & Dunning, G. (2006). Partial melting of metapelites in the Gagnon terrane below the high-pressure belt in the Manicouagan area (Grenville Province): Pressure-temperature (P–T) and U–Pb age constraints and implications. Canadian Journal of Earth Sciences, 38, 1309–1329.

Kelsey, D. E., Clark, C. & Hand, M. (2008). Thermobarometric modelling of zircon and monazite growth in melt-bearing systems: Examples using model metapelitic and metapsammitic granulites. Journal of Metamorphic Geology, 26, 199–212.

Kooijman, E., Smit, M. A., Mezger, K. & Berndt, J. (2012). Trace element systematics in granulite facies rutile: Implications for Zr geothermometry and provenance studies. Journal of Metamorphic Geology, 30, 397–412.

Lasalle, S. & Indares, A. (2014). Anatectic record and contrasting P–T paths of aluminous gneisses from the central Grenville Province. Journal of Metamorphic Geology, 32, 627–646.

Leeman, W. P., MacRae, C. M., Wilson, N. C., Torpy, A., Lee, C.-T. A., Student, J. J., Thomas, J. B. & Vicenzi, E. P. (2012). A study of cathodoluminescence and trace

element compositional zoning in natural quartz from volcanic rocks: Mapping titanium content in quartz. Microscopy and Microanalysis, 18, 1322–1341.

Luvizotto, G. L. & Zack, T. (2009). Nb and Zr behavior during high-grade metamorphism and retrogression: An example from the Ivrea–Verbano Zone. Chemical Geology, 261, 303–317.

Mitchell, R. J. & Harley, S. L. (2017). Zr-in-rutile resetting in aluminosilicate bearing ultra-high temperature granulites: Refining the record of cooling and hydration in the Napier Complex, Antarctica. Lithos, 272–273, 128–146.

Meyer, M., John, T., Brandt, S. & Klemd, R. (2011). Trace element composition of rutile and the application of Zr-in-rutile thermometry to UHT metamorphism (Epupa Complex, NW Namibia). Lithos, 126, 388–401.

Morgan, D. J., Jollands, M. C., Lloyd, G. E. & Banks, D. A. (2014). Using titanium-in-quartz geothermometry and geospeedometry to recover temperatures in the aureole of the Ballachulish Igneous Complex, NW Scotland. Geological Society, London, Special Publications, 394, 145–165.

Müller, A., Lennox, P. & Trzebski, R. (2002). Cathodoluminescence and micro-structural evidence for crystallisation and deformation processes of granites in the Eastern Lachlan Fold Belt (SE Australia). Contributions to Mineralogy and Petrology, 143, 510–524.

Palin, R. M., Weller, O. M., Waters, D. J. & Dyck, B. (2016). Quantifying geological uncertainty in metamorphic phase equilibria modelling; a Monte Carlo assessment and implications for tectonic interpretations. Geoscience Frontiers, 7, 591–607.

Powell, R. & Holland, T. J. B. (1988). An internally consistent dataset with uncertainties and correlations: 3. applications to geobarometry, worked examples and a computer program. Journal of Metamorphic Geology, 6, 173–204.

Sawyer, E. W. (1999). Criteria for the recognition of partial melting. Physics and Chemistry of the Earth, Part A: Solid Earth and Geodesy, 24, 269–279.

Spear, F. S. & Wark, D. A. (2009). Cathodoluminescence imaging and titanium thermometry in metamorphic quartz. Journal of Metamorphic Geology, 27, 187–205.

Spear, F. S., Kohn, M. J. & Cheney, J. T. (1999). P-T paths from anatectic pelites. Contributions to Mineralogy and Petrology, 134, 17–32.

Storm, L. C. & Spear, F. S. (2009). Application of the titanium-in-quartz thermometer to pelitic migmatites from the Adirondack Highlands, New York. Journal of Metamorphic Geology, 27, 479–494.

Thomas, J. B., Watson, E. B., Spear, F. S., Shemella, P. T., Nayak, S. K. & Lanzirotti, A. (2010). TitaniQ under pressure: The effect of pressure and temperature on the solubility of Ti in quartz. Contributions to Mineralogy and Petrology, 160, 743–759.

Thomas, J. B., Watson, E. B., Spear, F. S. & Wark, D. A. (2015). TitaniQ recrystallized: Experimental confirmation of the original Ti-in-quartz calibrations. Contributions to Mineralogy and Petrology, 169, 27.

Tomkins, H. S., Powell, R. & Ellis, D. J. (2007). The pressure dependence of the zirconium-in-rutile thermometer. Journal of Metamorphic Geology, 25, 703–713.

Walderhaug, O. & Rykkje, J. (2000). Some examples of the effect of crystallographic orientation on the cathodoluminescence colors of quartz. Journal of Sedimentary Research, 70, 545–548.

Wark, D. A. & Watson, E. B. (2006). TitaniQ: A titanium-in-quartz geothermometer. Contributions to Mineralogy and Petrology, 152, 743–754.

Waters, D. J. (2001). The significance of prograde and retrograde quartz-bearing intergrowth microstructures in partially melted granulite-facies rocks. Lithos, 56, 97–110.

White, R. W. & Powell, R. (2002). Melt loss and the preservation of granulite facies mineral assemblages. Journal of Metamorphic Geology, 20, 621–632.

White, R. W., Powell, R. & Holland, T. J. B. (2007). Progress relating to calculation of partial melting equilibria for metapelites. Journal of Metamorphic Geology, 25, 511–527.

Yakymchuk, C. & Brown, M. (2014). Behaviour of zircon and monazite during crustal melting. Journal of the Geological Society, London, 171, 465–479.

Zack, T., Moraes, R. & Kronz, A. (2004). Temperature dependence of Zr in rutile: Empirical calibration of a rutile thermometer. Contributions to Mineralogy and Petrology, 148, 471–488.

Zhang, C., Holtz, F., Koepke, J., Berndt, J. & Ma, C. (2014). Decompressional anatexis in the migmatite core complex of northern Dabie orogen, eastern China: Petrological evidence and Ti-in-quartz thermobarometry. Lithos, 202–203, 227–236.

Table 2.1. Sample bulk compositions (mol. %) after Indares et al. (2008) and Lasalle & Indares (2014). The proportion of H_2O was calculated using the modal proportion of biotite and the H–Ti substitution scheme of White et al. (2007).

Sample	H_2O	SiO_2	Al_2O_3	CaO	MgO	FeO	K_2O	Na_2O	TiO_2	Total
100	2.07	69.24	10.57	2.66	3.19	6.36	2.62	2.57	0.72	100.00
244	1.38	64.92	11.71	2.22	7.32	6.95	3.03	1.59	0.63	99.75
320	2.15	64.59	13.31	1.19	5.58	7.58	2.77	1.83	0.71	99.71
107b	1.27	74.76	8.99	1.29	3.69	4.16	3.32	2.01	0.52	100.01
HJ60b	1.67	69.22	11.47	0.79	4.57	7.93	2.64	1.03	0.68	100.00

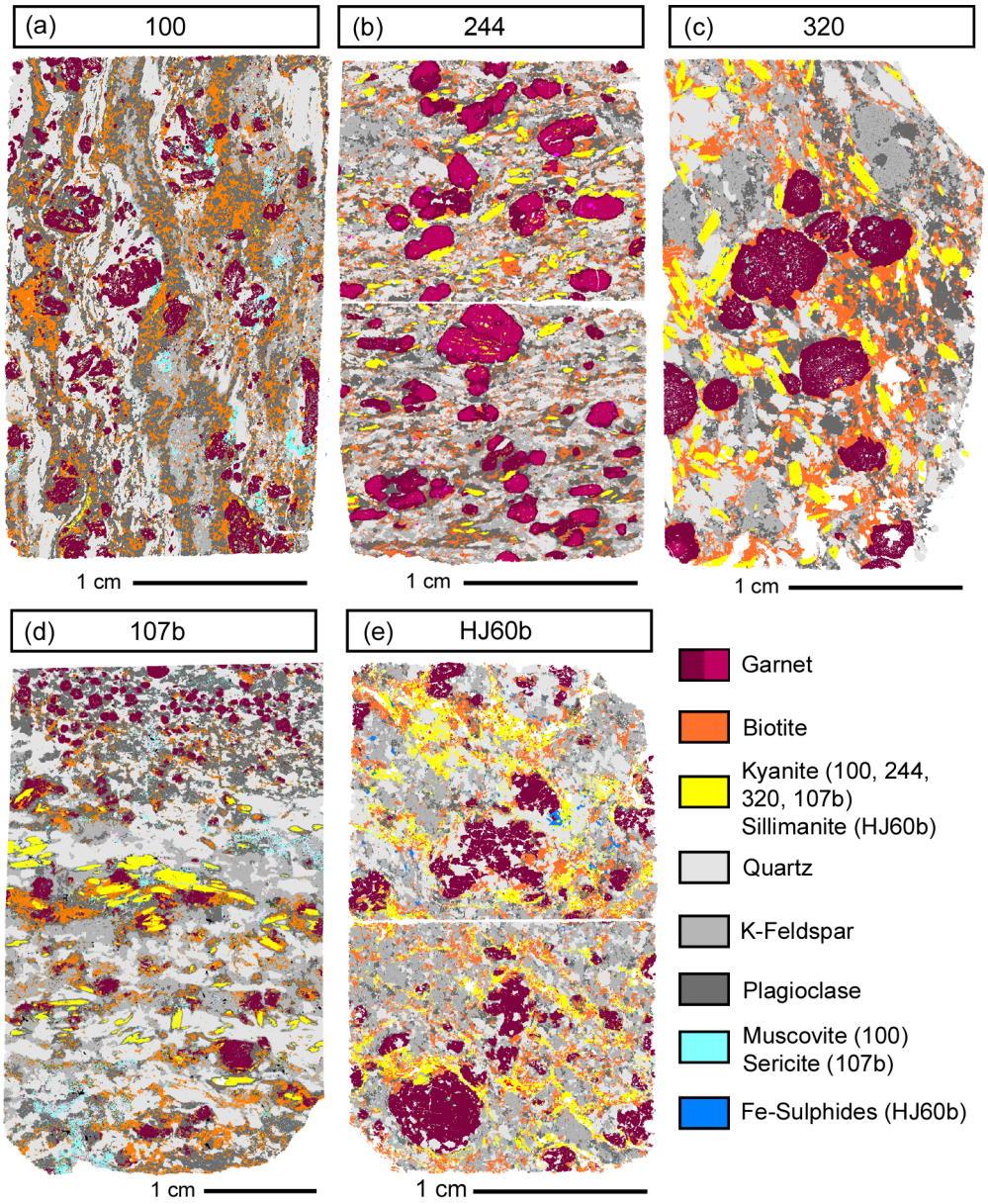

Figure 2.1. SEM false colour mineralogical maps of samples (a) 100, (b) 244, (c) 320, (d) 107b, and (e) HJ60b.

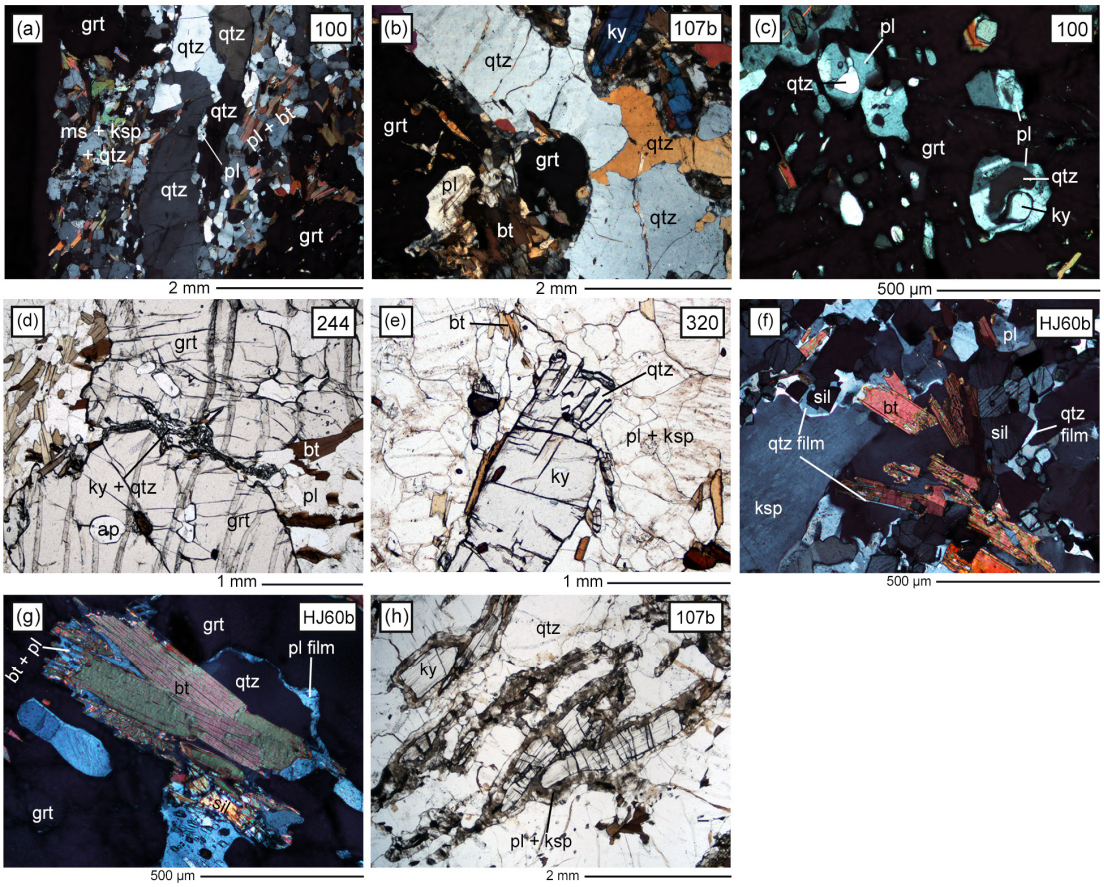

Figure 2.2. Selected photomicrographs: quartz ribbons (a–b), microstructures involving quartz related to the former presence of partial melt (c–h). (a) Quartz ribbon comprising several large subgrains (sample 100; XPL). (b) Quartz ribbon with embayed edges, composed of several distinct quartz grains (sample 107b; XPL). (c) Composite inclusions in garnet; prograde quartz and kyanite surrounded by optically continuous plagioclase (sample 100; XPL). (d) A pod of skeletal kyanite intergrown with quartz between two garnet porphyroblasts (sample 244; PPL). (e) Kyanite porphyroblast with elongate overgrowths intergrown with quartz (sample 320; PPL). (f) Quartz films and pools around sillimanite and biotite (sample HJ60b; XPL). (g) Quartz separated from garnet by a plagioclase film, and skeletal biotite + plagioclase after a garnet rim (sample HJ60b; XPL). (h) Kyanite porphyroblasts separated from quartz by successive rims of plagioclase and K-feldspar with brown alteration (sample 107b; PPL). Abbreviations: garnet (grt), quartz (qtz), plagioclase (pl), kyanite (ky), biotite (bt), muscovite (ms), K-feldspar (ksp), sillimanite (sil), apatite (ap).

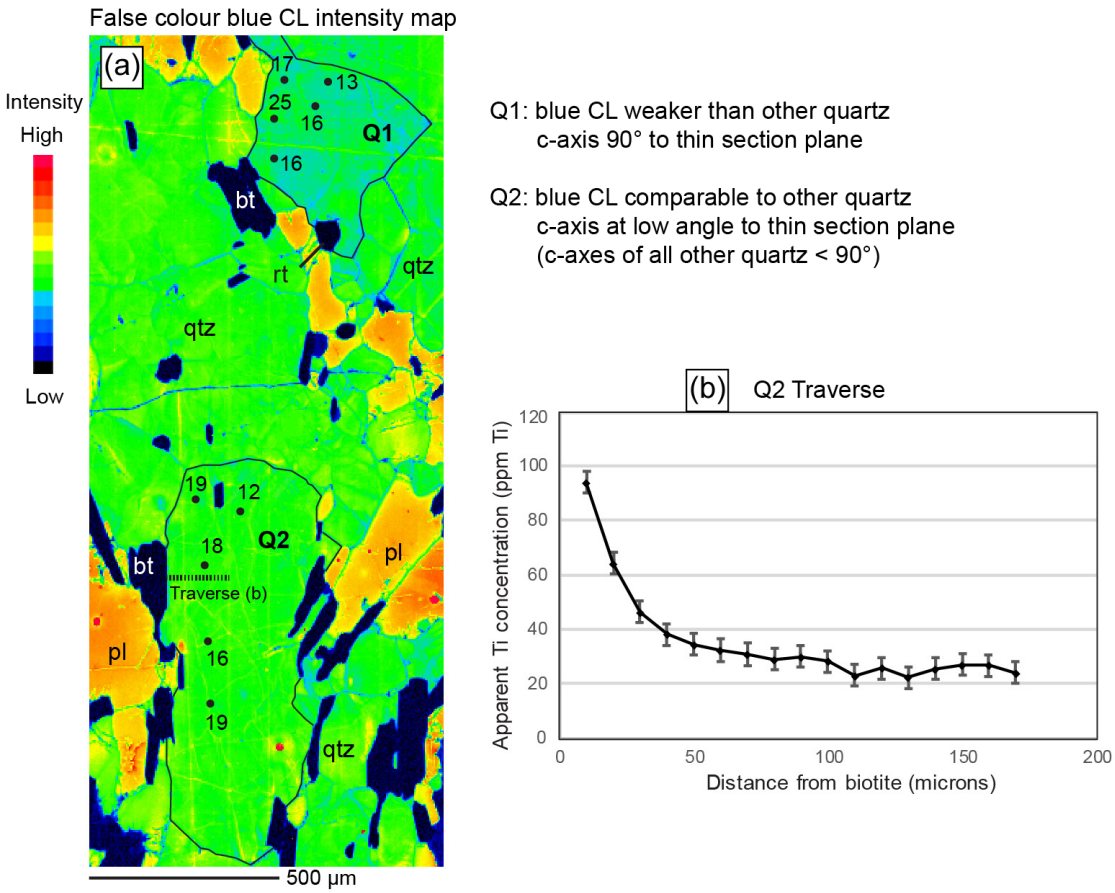

Figure 2.3. (a) False colour map showing the intensity of the blue CL emission of quartz in a recrystallised quartz ribbon in sample 100. Two grains (Q1 and Q2, outlined) have comparable Ti contents but different CL intensity, interpreted to be caused by the significantly different optical orientations of these grains. (b) A traverse of 17 points, each spaced 10 µm apart, were analysed (at 20 kV) orthogonal to the interface between biotite and quartz. This interface was determined by optical microscopy to be approximately perpendicular to the plane of the thin section, and thus the biotite itself did not contaminate the analyses. Given the homogeneity of the quartz grain in (a), the sharp increase in Ti toward the biotite-quartz interface beginning at ~ 50 µm distance is interpreted to have been caused by secondary fluorescence of Ti in biotite.

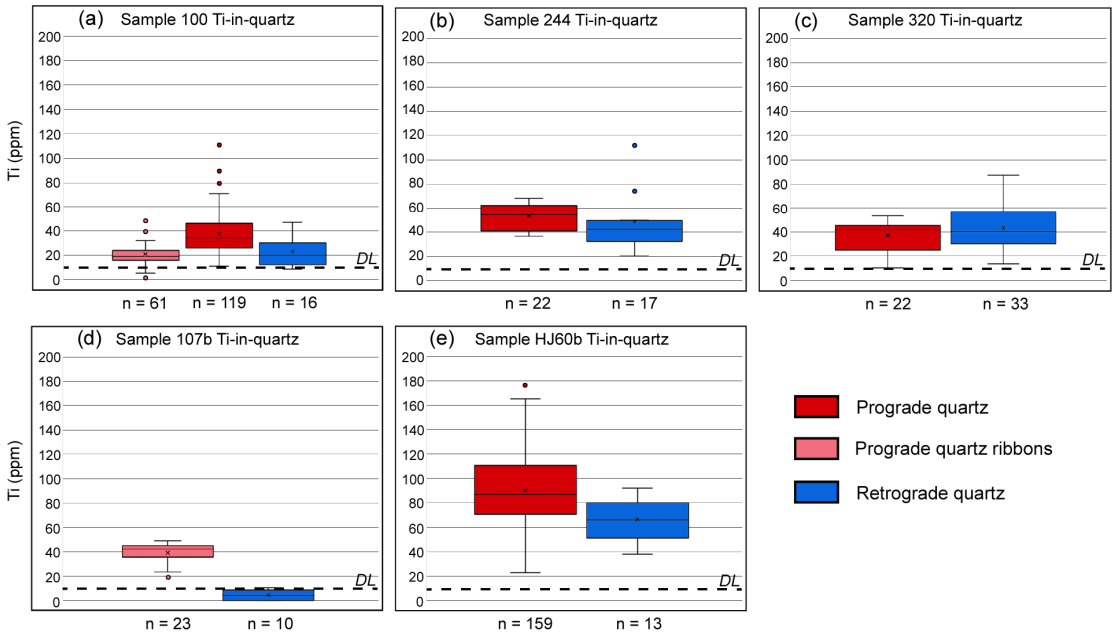

Figure 2.4. Box and whisker plots depicting Ti contents (ppm) of prograde and retrograde quartz; n = number of analyses, multiple measurements were taken from sufficiently large grains. Boxes were calculated with the median excluded, whiskers extend to 1.5 times the interquartile range at maximum (above and below the box), and outliers are data points outside 1.5 times the interquartile range. (a) Prograde quartz is generally richer in Ti than retrograde in sample 100; prograde quartz ribbons are a separate Ti-poor population. (b) In sample 244, prograde and retrograde quartz are similar, with the former slightly richer in Ti. (c) Retrograde quartz tends to have a higher Ti content than prograde quartz in sample 320. (d) Sample 107b has distinct populations with narrow ranges; all prograde quartz has higher Ti than retrograde. (e) Prograde quartz has a large range, with most values higher than retrograde in sample HJ60b.

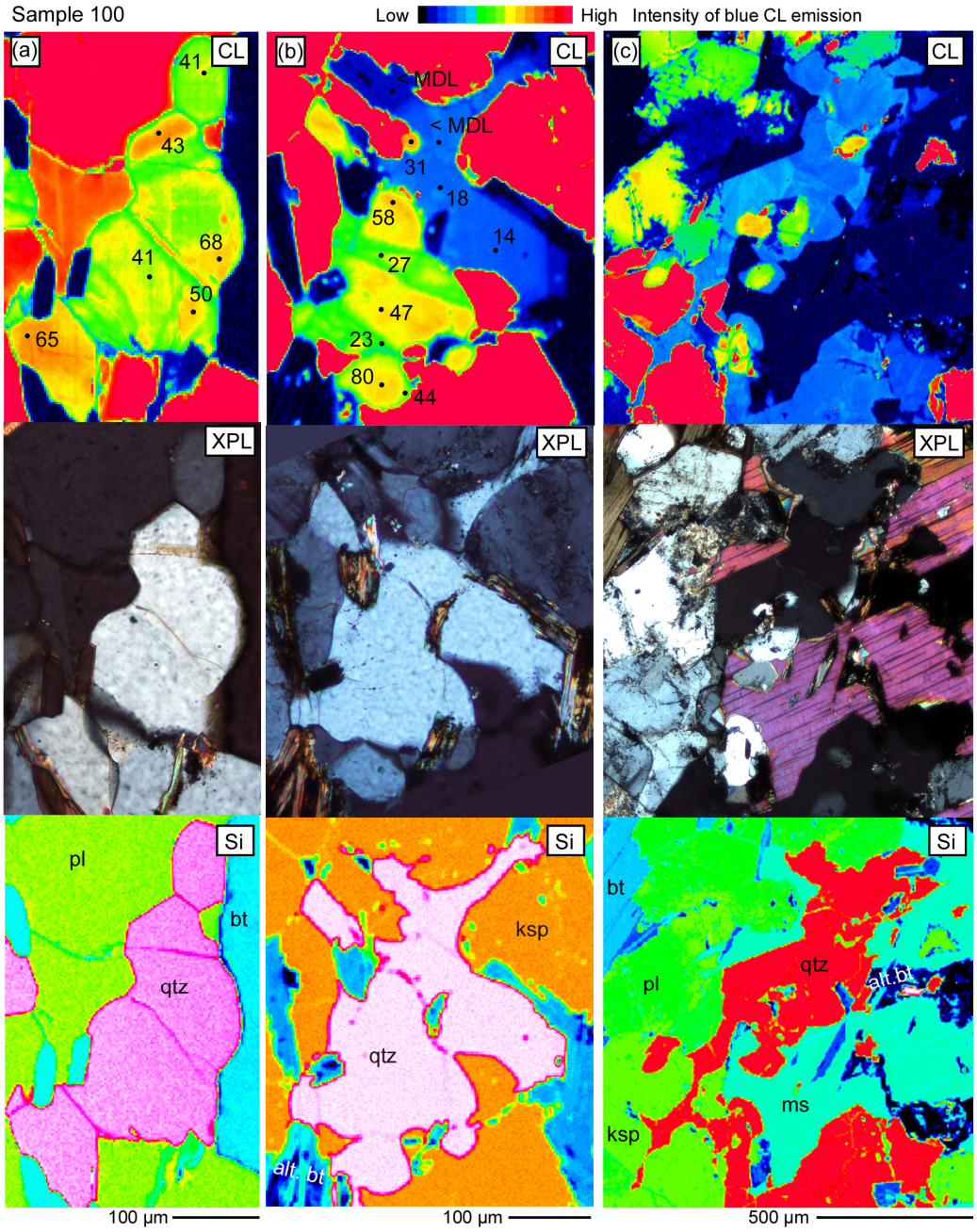

Figure 2.5. Quartz in sample 100 with measured Ti values (uncertainties ± 2 to 3 ppm). Top row: CL maps (false colour); middle row: photomicrographs; bottom row: Si x-ray maps (false colour; quartz has a different appearance in each due to differences in scale). (a) Prograde quartz in a biotite + plagioclase + kyanite domain, with a patchy appearance in the CL map. (b) A Ti-rich prograde quartz grain with Ti-poor overgrowth filling interstices in a K-feldspar cluster. (c) A retrograde patch of quartz with a weak blue CL emission intergrown with muscovite.

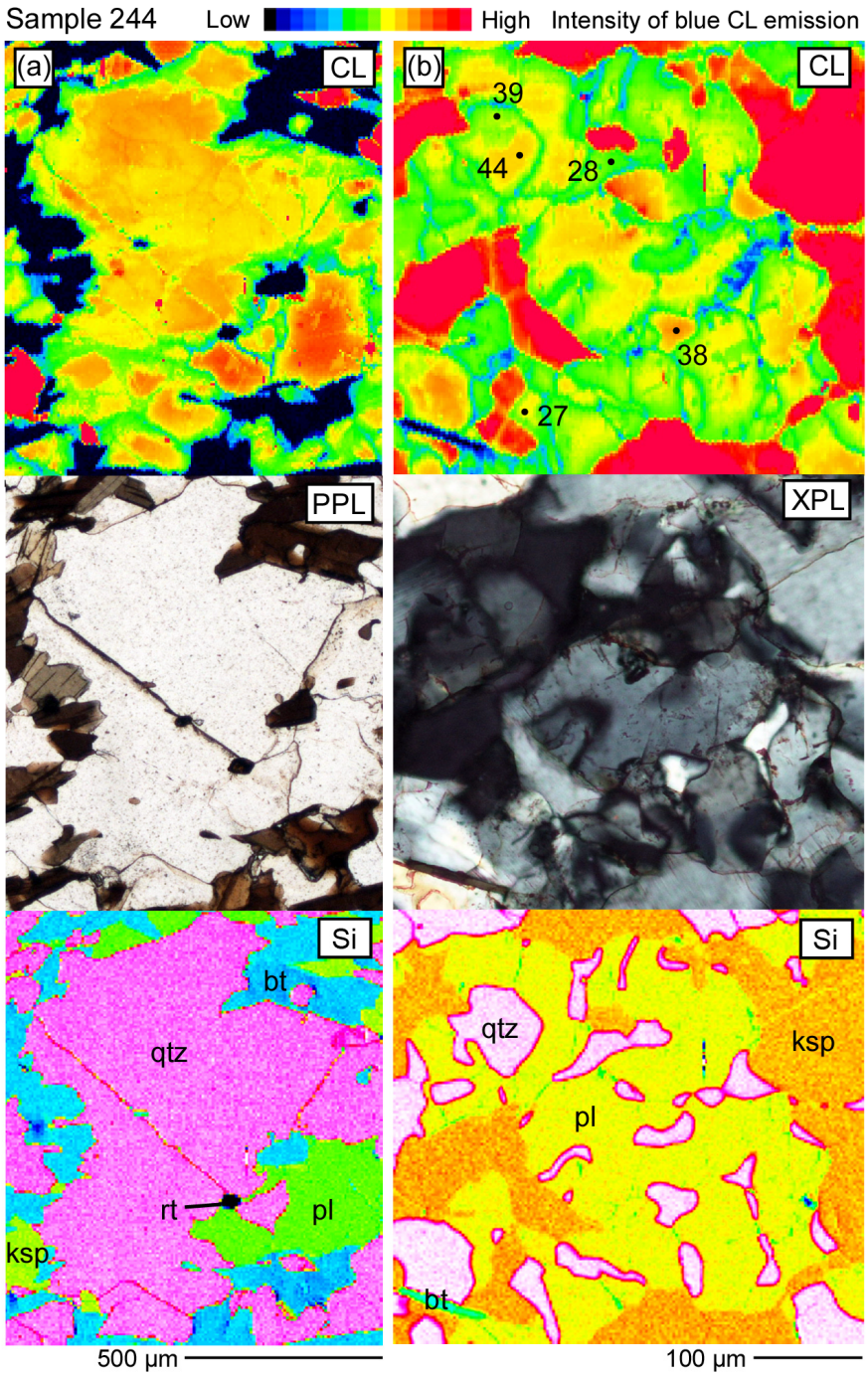

Figure 2.6. Quartz in sample 244 with measured Ti values (uncertainties ± 2 ppm); image types and configuration as in Fig. 2.5. (a) A prograde quartz grain zoned toward rims emitting weaker blue CL. (b) A plagioclase + quartz intergrowth, where quartz has an interstitial character (visible in XPL). Both minerals emit blue CL with similar intensity.

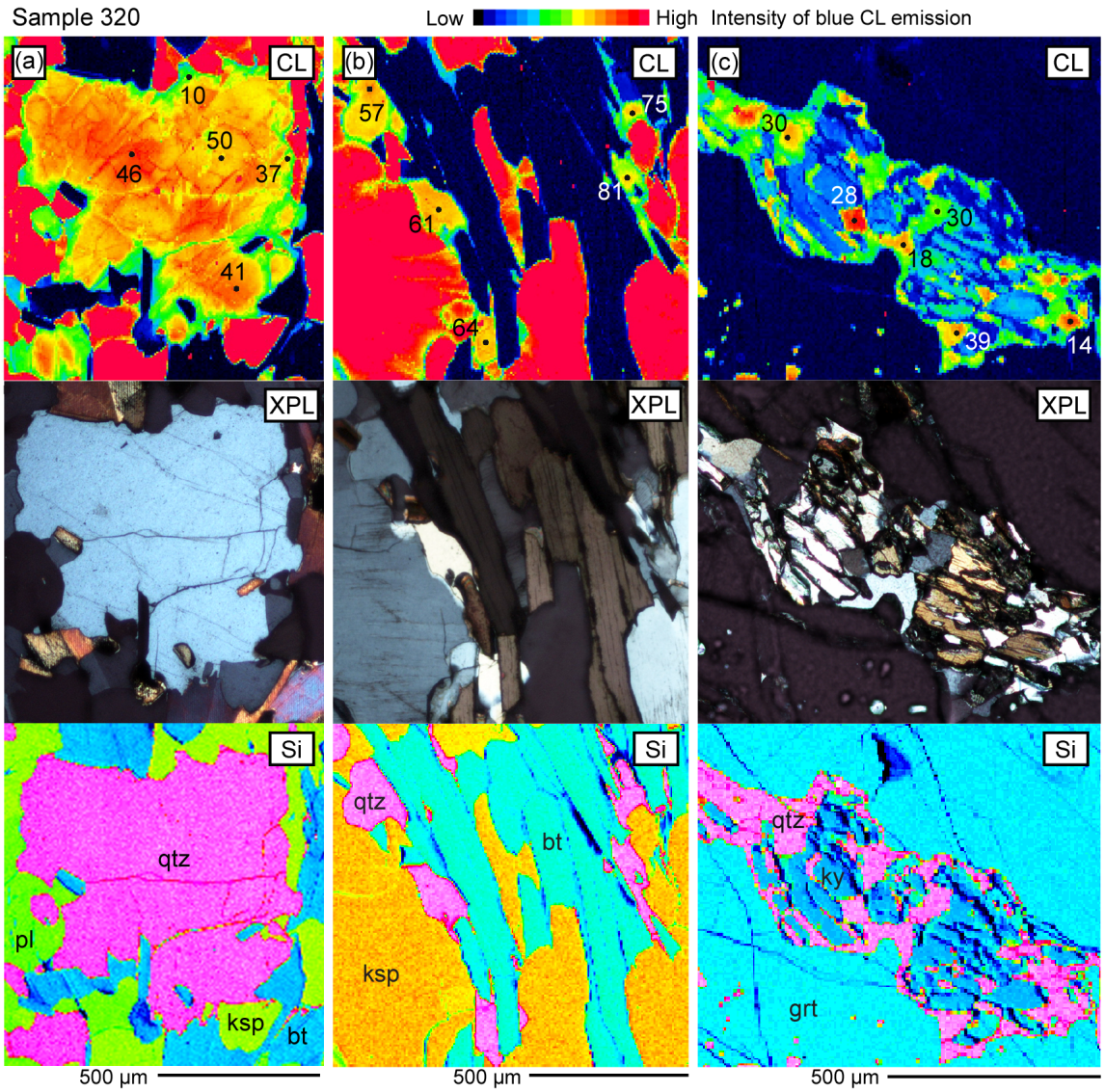

Figure 2.7. Quartz in sample 320 with measured Ti values (uncertainties ± 2 ppm); image types and configuration as in Fig. 2.5. (a) Prograde quartz crystal with a strong blue CL emission in the core. (b) A biotite cluster and associated pools of quartz with interstitial features. (c) Skeletal kyanite + quartz pod between two garnet crystals.

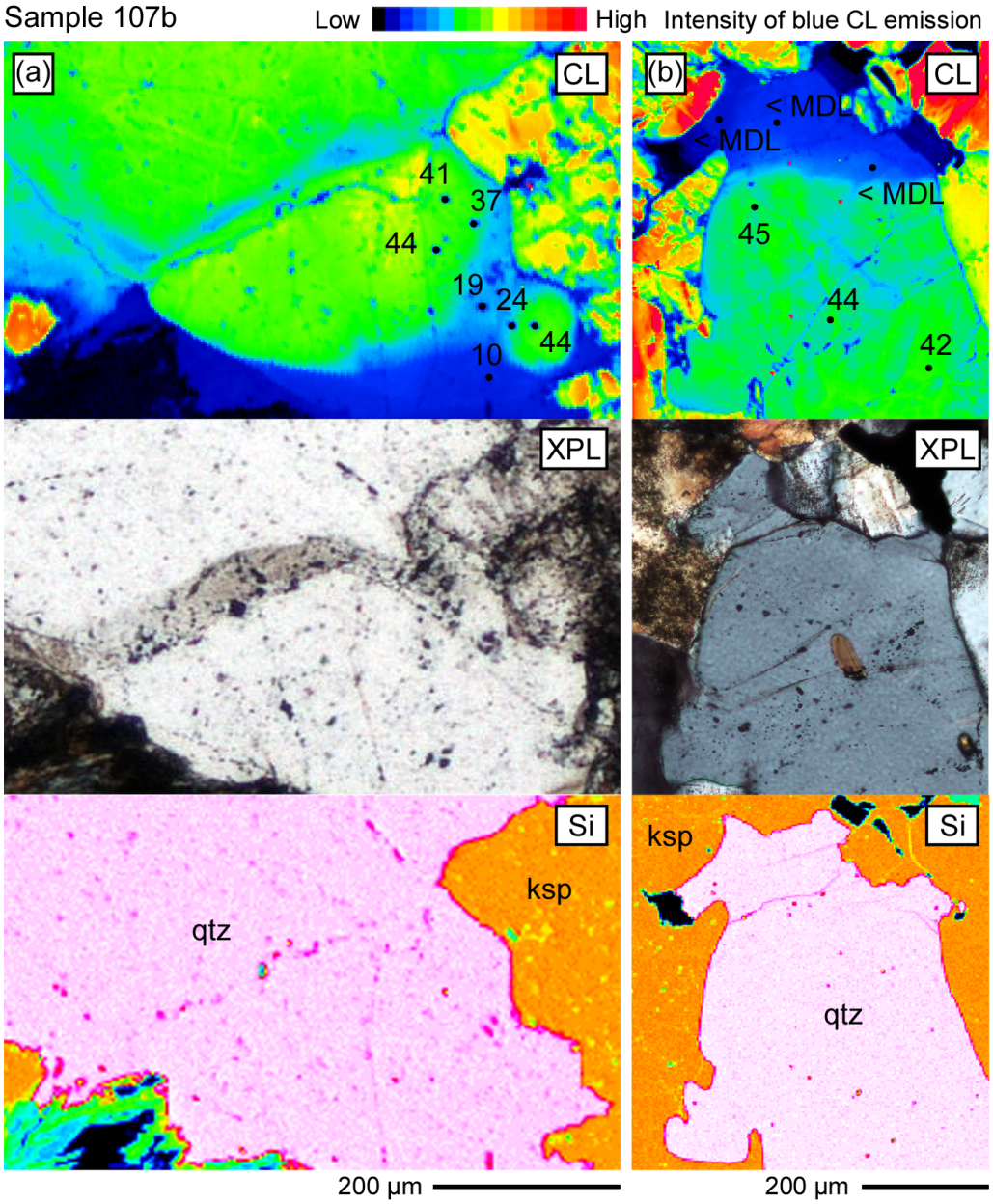

Figure 2.8. Quartz in sample 107b with measured Ti values (uncertainties ± 3 ppm); image types and configuration as in Fig. 2.5. (a) Part of a large prograde grain, which is truncated and overgrown by quartz with a weak blue CL emission (bottom). (b) End of a prograde quartz ribbon, which has a sharp boundary with a Ti-poor overgrowth showing an interstitial morphology.

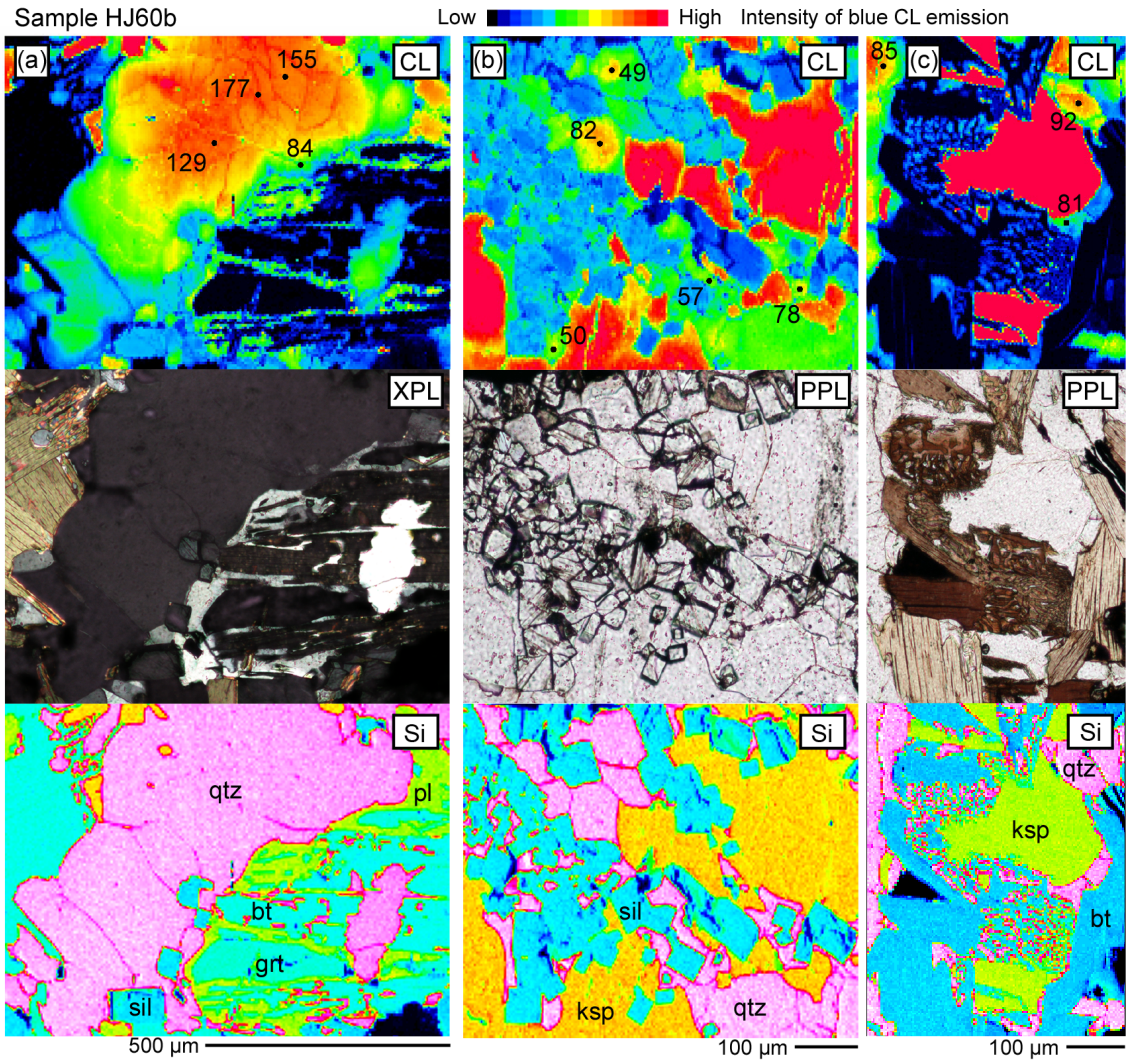

Figure 2.9. Quartz in sample HJ60b with measured Ti values (uncertainties ± 2 ppm); image types and configuration as in Fig. 2.5. (a) Prograde quartz grain with a core emitting strong blue CL. (b) A sillimanite cluster with films and pools of quartz, surrounded by K-feldspar. (c) Symplectic intergrowth of biotite and quartz associated with K-feldspar.

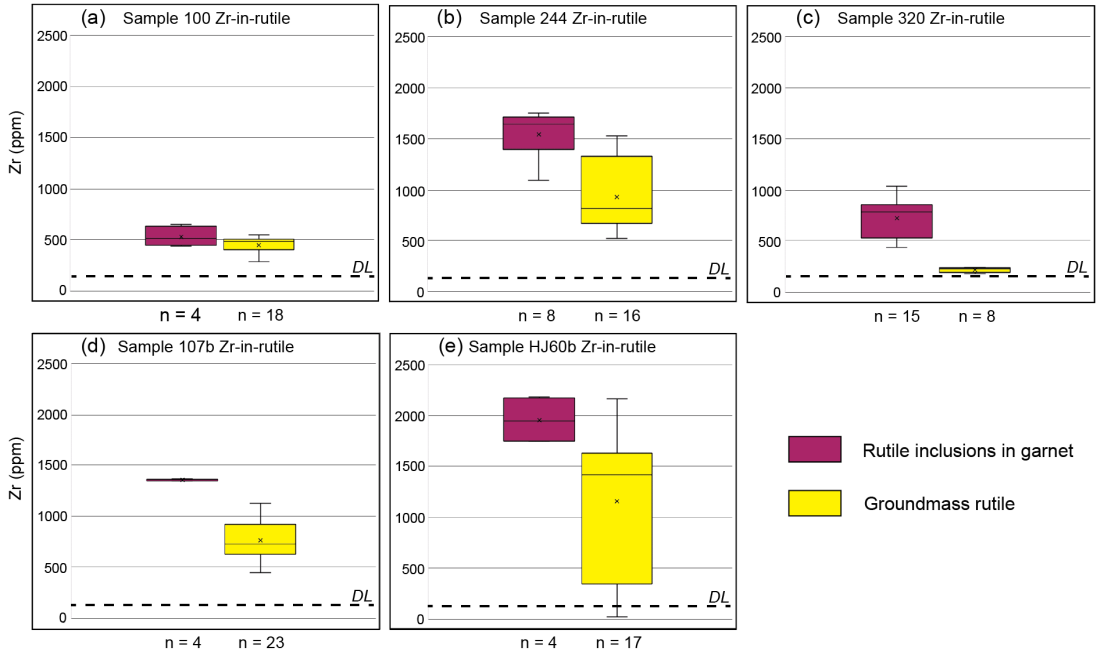

Figure 2.10. Box and whisker plots with measured Zr contents (ppm) of rutile in garnet and groundmass rutile. (a) In sample 100, both types of rutile have comparable Zr contents. (b) Most rutile inclusions in garnet have higher Zr concentrations than groundmass grains in sample 244. (c) In sample 320, all analysed rutile inclusions in garnet are more Zr-rich than groundmass grains. (d) One rutile inclusion in garnet in sample 107b is significantly more Zr-rich than the analysed groundmass grains. (e) Groundmass rutile has a large Zr range and overlaps with inclusions in garnet in sample HJ60b.

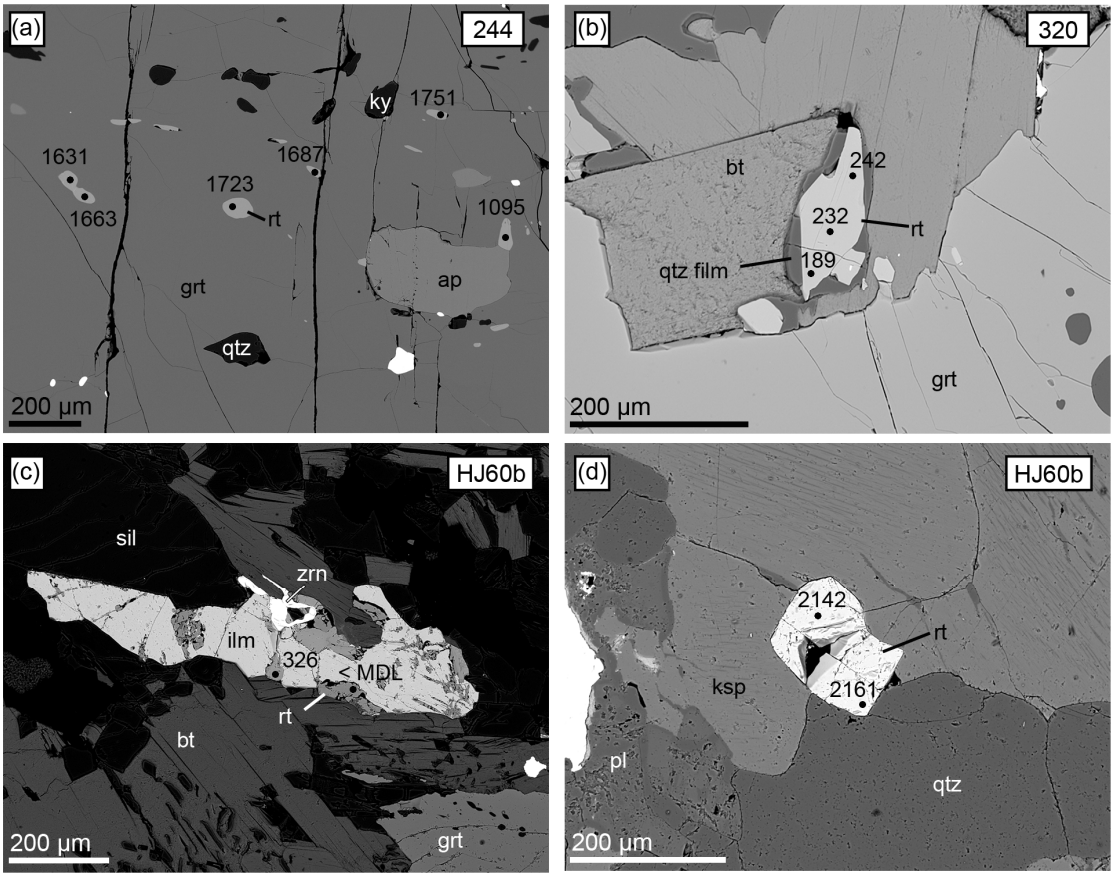

Figure 2.11. Backscatter electron (BSE) images of some examples of rutile (Zr values ± 12 to 17 ppm). (a) Small rutile inclusions in garnet in sample 244, most with high Zr contents. (b) Xenomorphic groundmass rutile, separated from biotite by a film of quartz, in sample 320. (c) Rutile mostly replaced by ilmenite (ilm) in sample HJ60b, associated with zircon (zrn) with an interstitial morphology. (d) Zirconium-rich rutile with idiomorphic faces in the groundmass of sample HJ60b.

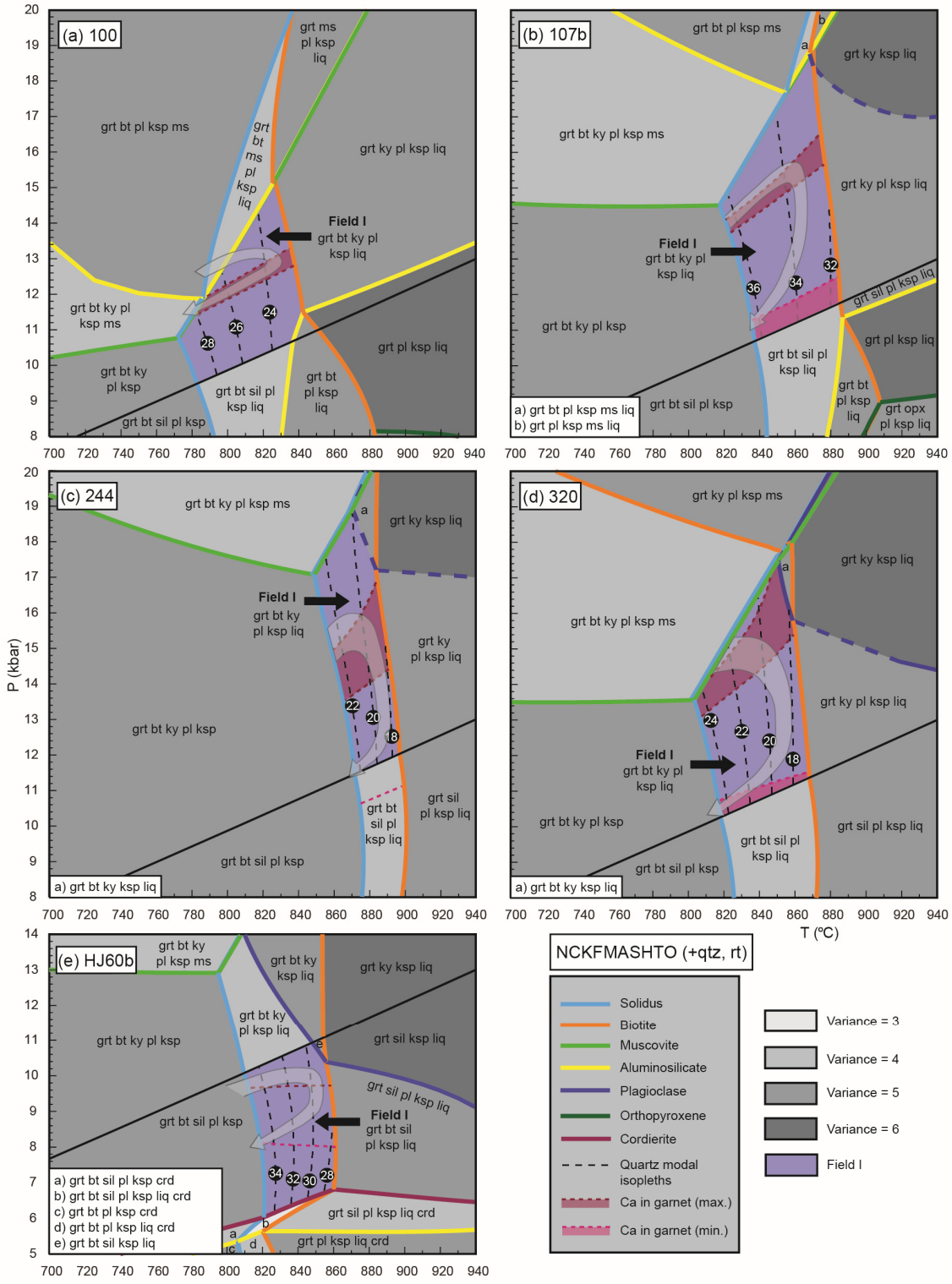

Figure 2.12. *P–T* pseudosections for all samples, with the interpreted *P–T* path and modal proportions of quartz within the stability field of the assemblage grt–bt–ky/sil–pl–ksp–liq–qtz–rt (Field I).

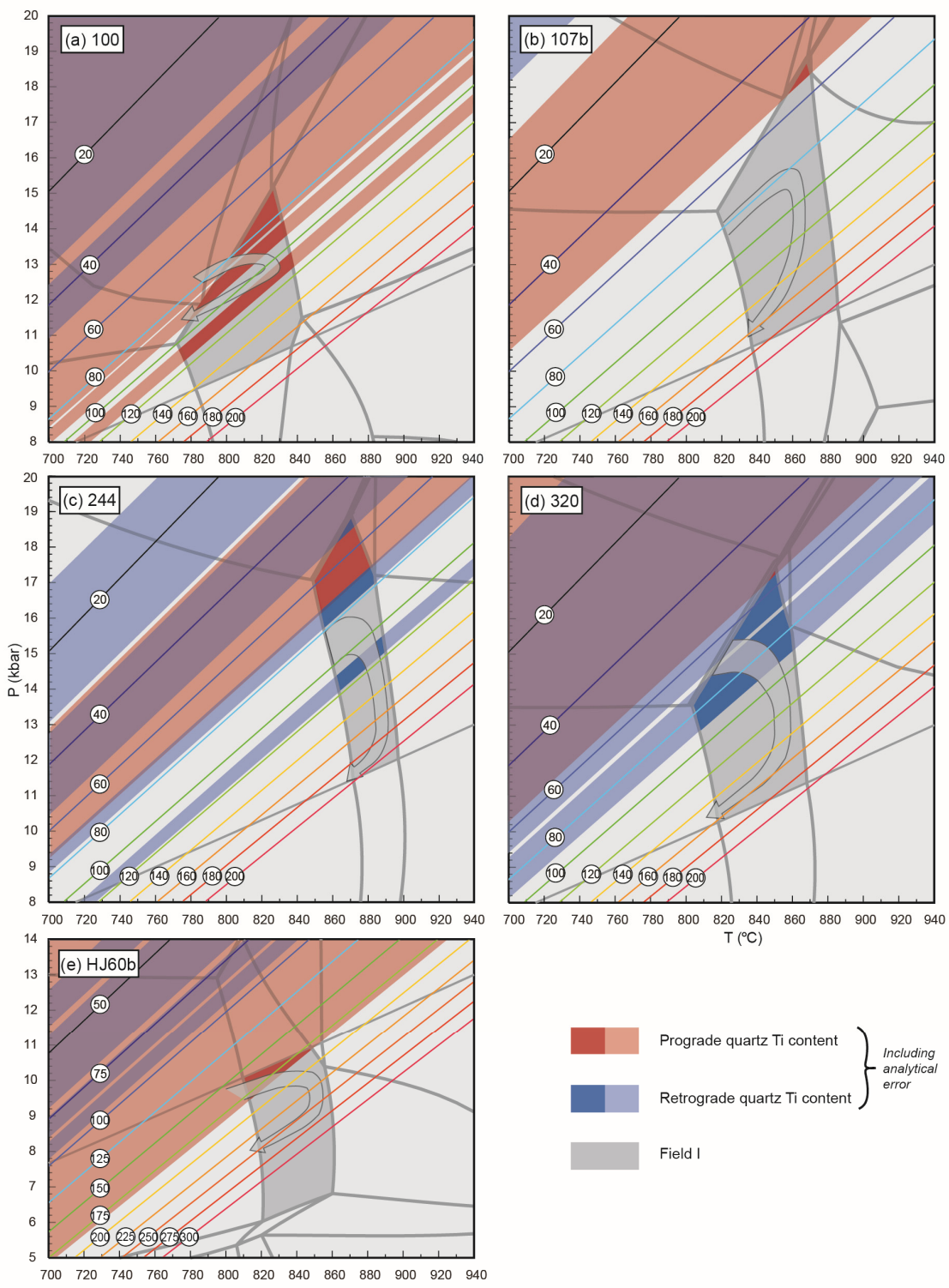

Figure 2.13. *P–T* pseudosections overlain by Ti-in-quartz isopleths (after Thomas et al., 2010). Measured Ti-in-quartz values are indicated on the diagrams with analytical error included.

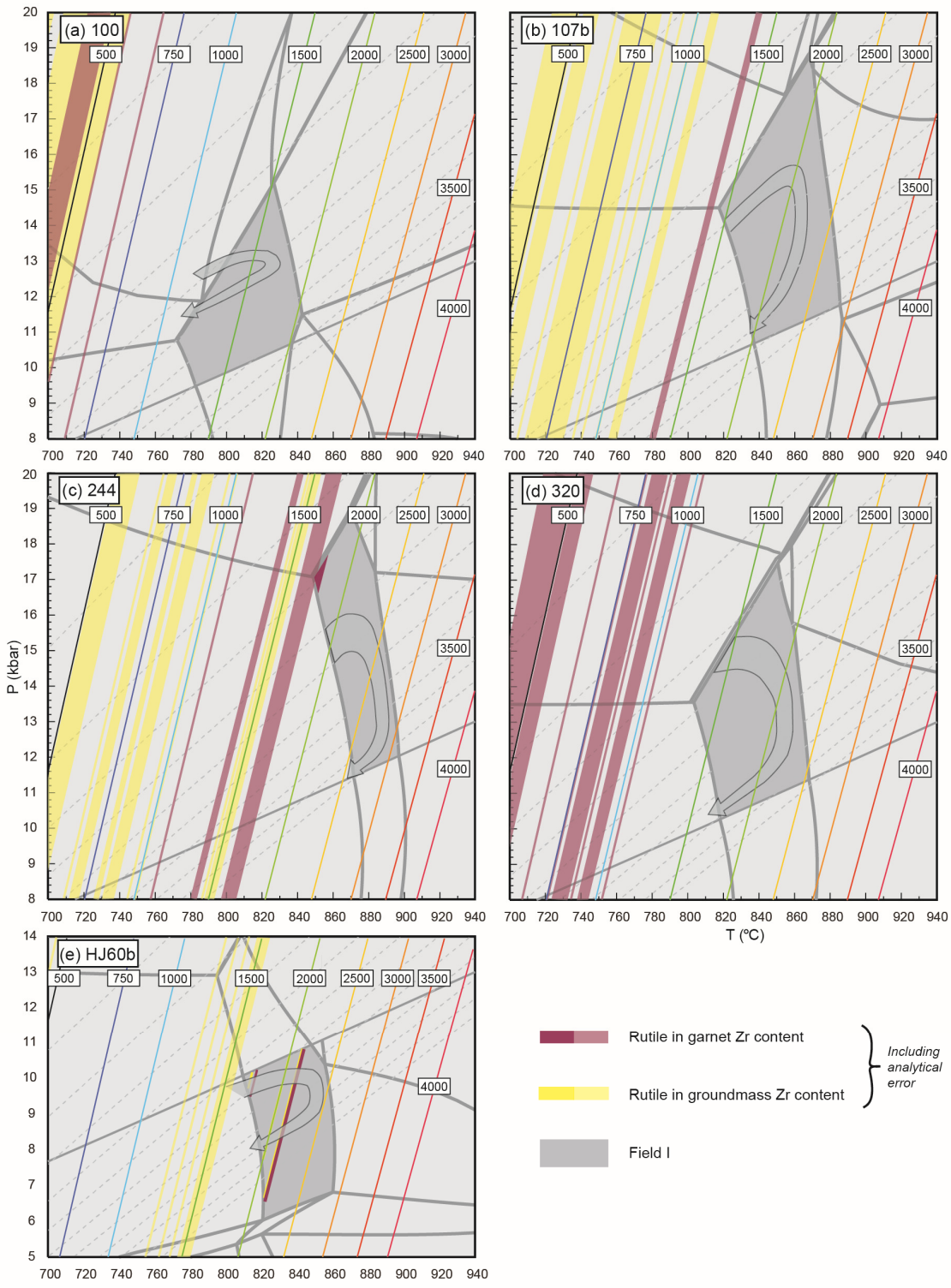

Figure 2.14. *P–T* pseudosections overlain by Zr-in-rutile isopleths (after Tomkins et al, 2007); the Ti-in-quartz isopleths are shown as dashed grey lines for comparison. The measured values of Zr-in-rutile indicated on the diagrams include analytical error.

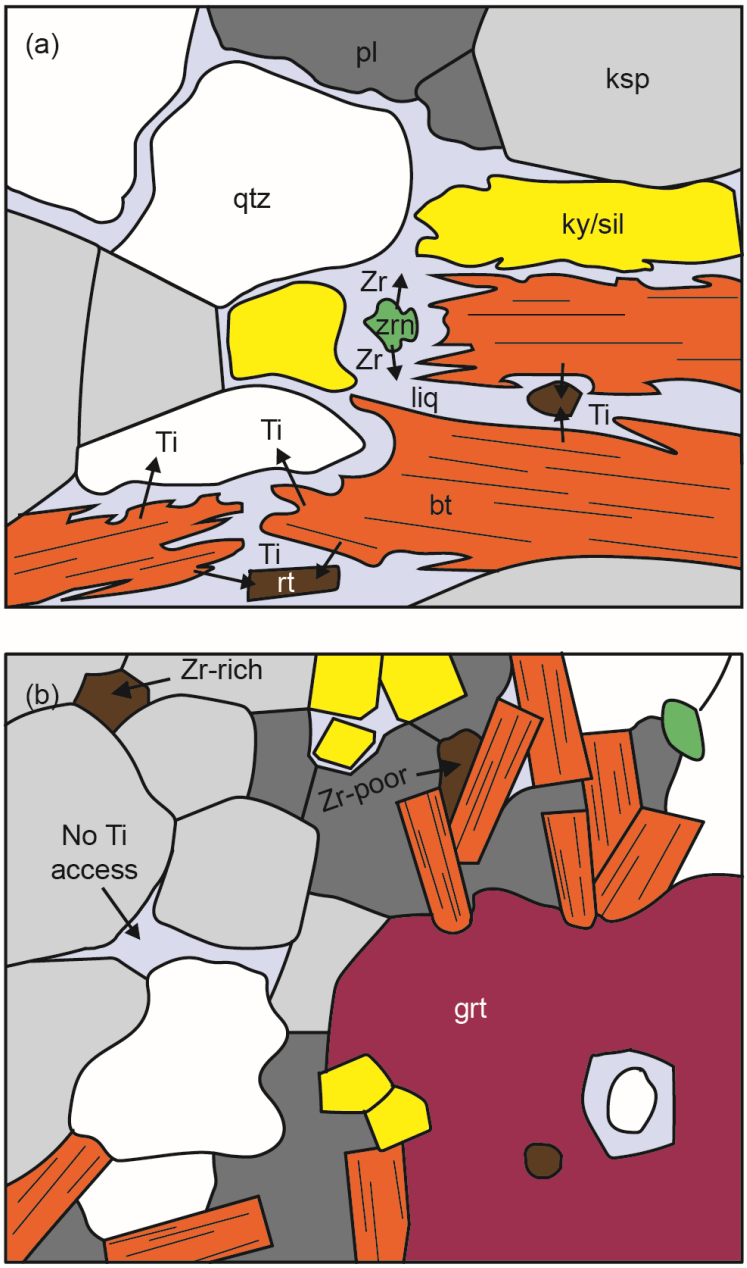

Figure 2.15. Schematic diagram showing key (a) near-peak prograde and (b) retrograde textures, with focus on quartz, rutile, and zircon.

CHAPTER 3: THE REACTION HISTORY OF KYANITE IN HIGH-PRESSURE ALUMINOUS GRANULITES

Abstract

Cathodoluminescence (CL) mapping of kyanite in high-*P*, aluminous granulites from the central Grenville Province reveals internal structures that are linked to their metamorphic reaction history. In most samples, individual kyanite crystals are shown to be composite porphyroblasts comprising three distinct generations, defined by their CL intensity and Cr (± V, Ti, Fe, and Ga) content, and each separated by resorbed interfaces. In contrast, one sub-aluminous sample contains two types of kyanite; one as resorbed inclusions in garnet, and another in the groundmass or replacing garnet. These textural variants of kyanite are interpreted within the framework of phase equilibria modelling. In *P–T* pseudosections, a first generation of kyanite, which is only present in the most aluminous samples, is potentially linked to the breakdown of staurolite, and its resorption is consistent with a subsequent increase in pressure. This kyanite represents the earliest remnant of prograde metamorphism identifiable in these rocks. The second generation, present in the porphyroblasts in the same samples and as inclusions in garnet in the sub-aluminous sample, is interpreted to be the peritectic product of muscovite dehydration melting. Resorption of this kyanite is consistent with subsequent continuous dehydration melting of biotite, which is also inferred based on microstructural considerations. The final generation of kyanite, present as rims on porphyroblasts in aluminous samples and as part of the groundmass or replacing garnet in the sub-aluminous rock, is interpreted to

have grown during melt crystallisation upon retrogression. The presence of retrograde kyanite implies that the melt crystallised over a wide range of temperatures, and provides an important constraint on the *P–T* conditions of the metamorphic peak and on the retrograde *P–T* paths. Cathodoluminescence mapping is crucial for identifying retrograde kyanite in aluminous samples, as it preferentially overgrows existing kyanite rather than replacing other prograde phases. The scarcity of kyanite in sub-aluminous rocks allows retrograde kyanite to grow as discrete crystals that can be identified by optical microscopy. This work attests to the potential of unconventional tools such as CL imaging for deciphering the metamorphic history of rocks.

3.1 Introduction

High-pressure (high-*P*) granulites are minor but important constituents of large hot orogens (LHO) and their metamorphic record can provide insights into the tectonic processes operating in deep orogenic crust (O'Brien & Rötzler, 2003; Rivers et al., 2002; Rivers et al., 2012). Aluminous high-*P* granulites typically record evidence of anatexis at deep crustal levels and commonly contain kyanite, which participates in key metamorphic reactions, including those producing melt (e.g., Guilmette et al., 2011; Indares et al., 2008; Spear et al., 1999). The growth history of kyanite can therefore provide a window into the metamorphic evolution of high-*P* aluminous rocks.

Kyanite has a simple chemistry (Al_2SiO_5), but it may contain significant concentrations of trace elements, in particular Cr, Ti, V, and Fe, along with others (Chinner, et al., 1969; Herz & Dutra, 1964; Hietanen, 1956; Müller et al., 2016; Pearson

& Shaw, 1960). Trace elements have been found to record and reveal growth zonation particularly well relative to major elements in some metamorphic minerals, most notably garnet (Spear & Kohn, 1996). As kyanite typically forms large porphyroblasts, trace element zonation highlighting its internal structures may be the key to interpreting its history. Patterns in trace elements may be subtle in chemical X-ray maps; however, luminescence studies of kyanite have shown an intense cathodoluminescence (CL) emission directly linked to trace Cr^{3+} replacing Al^{3+} in its structure (Müller et al., 2016; Wojtowicz, 1991). With CL imaging, subtle chemical variations become more apparent and fine details can be highlighted. Although few studies have investigated the internal patterns of kyanite crystals, they have found intriguing results. Yang & Rivers (2001) produced Cr X-ray maps of kyanite in subsolidus, amphibolite-facies rocks that revealed concentric, discontinuous, high-Cr zones and bifurcating Cr zones, which were interpreted to be inherited from micas that kyanite had replaced. These maps were relatively low resolution compared to CL images, and the low-Cr zones appeared featureless. Schertl et al. (2004) imaged kyanite in ultrahigh-pressure metamorphic rocks using CL and identified a low CL core and high CL rim in individual crystals, interpreted to represent two generations of kyanite growth. They proposed possible kyanite-forming reactions, prograde for the core and retrograde for the outer domain, based on inclusions. An investigation of kyanite CL by Müller et al. (2016) focused on a variety of rock types including metapelites, felsic granulites, and metamorphosed alteration zones, and also found some examples of a core and rim with distinct CL signatures in kyanite grains. These findings attest to the potential of CL imaging for highlighting the subtle changes in

trace element chemistry that delineate kyanite growth zones, which can then be linked to the metamorphic history.

In high-*P* anatectic aluminous rocks, kyanite has the potential to preserve a detailed metamorphic record, including key melt-producing (and/or -consuming) reactions and potentially subsolidus reactions. The sequence of melting reactions in aluminous rocks is predictable based on numerous studies of natural samples and experimental data, and thermodynamic modelling (e.g., Brown, 2013; Brown & Korhonen, 2009; Carrington & Harley, 1995; Gardien et al., 1995; Huang & Wyllie, 1974; Huang & Wyllie, 1975; Le Breton & Thompson, 1988; Patiño Douce & Johnston, 1991; Spear et al., 1999; Vielzeuf & Clemens, 1992; Vielzeuf & Holloway, 1988). Melt-producing reactions in the kyanite stability field have a steep d*P*/d*T*, and are therefore expected to proceed in sequence with increasing temperature. Given that free H_2O is scarce in high grade metamorphic environments (Spear et al., 1999), melt is mostly produced under fluid-absent conditions, by breakdown of micas; examples of such melting reactions are presented by Clemens (2006). In high-*P* aluminous rocks, dehydration melting of muscovite commonly takes place by a simplified kyanite-producing reaction such as:

Muscovite ± Plagioclase + Quartz = Kyanite ± K-feldspar + Liquid.

At higher temperature, biotite dehydration melting proceeds continuously by the generalised kyanite-consuming reaction

Biotite + Kyanite + Plagioclase + Quartz = Garnet ± K-feldspar + Liquid.

In addition, significant kyanite can also be produced at subsolidus conditions, as for instance by a final staurolite-out reaction of the type

$$\text{Staurolite} + \text{Muscovite} + \text{Quartz} = \text{Kyanite} + \text{Biotite} \pm \text{Garnet} + H_2O$$

(Chinner, 1965). Staurolite may not be an exclusively subsolidus phase, as it has been shown to be capable of persisting in a narrow *P–T* range after the onset of anatexis (Ferri et al., 2009; García-Casco et al., 2003). The involvement of kyanite in all the above reactions makes it a potentially valuable mineral for investigating kyanite-bearing high-*P* granulites.

In this contribution, we present the results of an investigation of kyanite in two aluminous and one sub-aluminous high-*P*, anatectic granulites from the Manicouagan area of the central Grenville Province in Québec. Cathodoluminescence images combined with trace element analyses reveal complex internal structures that are otherwise obscure. These internal structures can be linked to a reaction history consistent with phase equilibria models, and highlight the control of bulk composition on reaction history and kyanite production. In addition, by modelling trends of kyanite production and consumption in *P–T* space, internal patterns in kyanite were used to add constraints to *P–T* paths of metamorphism previously estimated by phase equilibria modelling.

3.2 Geological setting

The Grenville Province represents the remnants of the Mesoproterozoic Grenville Orogen, which formed by continental collision of Amazonia with Laurentia (Tohver et

al., 2004) from c. 1090 to 980 Ma (Rivers et al., 2012). It is interpreted to have been the first LHO on Earth, analogous to the modern Himalaya-Tibet Orogen (Rivers et al., 2012). Much of the Grenville Province comprises amphibolite- to granulite-facies rocks, which are thought to represent the middle to lower crust of a former orogenic plateau in the hinterland of the Grenville Orogen (Rivers et al., 2012). The Grenville Province therefore provides a window into the architecture of the lower levels of continental crust in an LHO, and an opportunity to investigate crustal processes involved in orogenesis. The Manicouagan area in the central Grenville Province (Fig. 3.1) hosts two distinct high-*P* domains, each containing suites of high-*P* aluminous gneisses that have been previously well-documented, and investigated by phase equilibria modelling (Indares et al., 2008; Lasalle & Indares, 2014).

The Gagnon terrane represents the Parautochthonous Belt in the central Grenville Province (Fig. 3.1; Rivers et al., 1989). At its southern contact with the overlying hinterland, this terrane reached high-*P* granulite to eclogite-facies conditions (Indares, 1993; Indares, 1995; Rivers, 1983) at c. 985 Ma, during the Rigolet phase of the Grenville Orogeny (Jordan et al., 2006). High-*P* metamorphism of aluminous rock was accompanied by partial melting by breakdown of muscovite followed by biotite, with *P*–*T* conditions estimated to have reached ~ 13 kb and ~ 840°C and a metamorphic evolution characterised by a hairpin-shaped *P*–*T* path with a moderate d*P*/d*T* (Indares et al., 2008; Jordan et al., 2006).

The Manicouagan Imbricate Zone, exposed north of the Manicouagan impact structure (dated at 214 ± 1 Ma, Hodych & Dunning, 1992; Fig. 3.1), comprises stacked

tectonic slices of the former Grenvillian hinterland. These rocks are part of a high-*P* belt discontinuously exposed in the Allochthonous Belt of the Grenville Province (Rivers et al., 2002), and are host to high-*P* granulite and eclogite. Anatectic aluminous rocks in the southern Manicouagan Imbricate Zone were estimated to have reached peak conditions of ~ 15–16 kb and ~ 840–870°C during the Ottawan phase of the orogeny at c. 1040–1030 Ma, followed by a steep retrograde *P–T* path (Dunning & Indares, 2010; Indares & Dunning, 2001; Indares et al., 2008; Lasalle & Indares, 2014).

3.3 Petrography

As mentioned above, three high-*P*, kyanite-bearing anatectic rocks were the focus of this research: samples 320 and 244 from the southern MIZ with relatively high modal proportions of kyanite (3.7–8.5 %; Table 3.1), referred to here as "aluminous", and the kyanite-poor sample 100 from the Gagnon terrane (with less than 1% kyanite; Table 3.1), referred to as "sub-aluminous". The sample locations are shown in Fig. 3.1. These samples, together with evidence for anatexis at the outcrop and sample scale, have been previously documented by Jordan et al. (2006; sample 100), Indares & Dunning (2001; sample 320, referred to as BNS3b), Indares et al. (2008; 320 and 100, referred to as BNS3b and GT100 respectively), and Lasalle & Indares (2014; sample 244). Additionally, phase equilibria modelling of these samples was done by Indares et al. (2008) and Lasalle & Indares (2014); the bulk compositions they calculated are given in Table 3.2.

3.3.1 Methods

A false color mineralogical map of each thin section was produced and modal mineralogy calculated using an FEI Quanta 400 scanning electron microscope (SEM) at Memorial University of Newfoundland with Mineral Liberation Analysis (MLA) software (JKTech, University of Queensland, Australia), at operating conditions of 25 kV accelerating voltage and 10 nA beam current. With these maps, contrasting textural domains and associations between minerals at the thin section scale are highlighted. To image internal kyanite structures, CL maps of individual crystals were acquired using the xCLent IV system coupled to a JEOL JXA-8230 electron probe microanalyzer (EPMA) at Memorial University, with mapping conditions of 20 kV, 200 nA, and 80 ms dwell time with step sizes of 2 μm to 7 μm depending on the area mapped. This system collects a CL spectrum from each pixel from the UV to the IR and produces a polychromatic false colour map of CL intensity, where the different colors represent different levels of CL intensity.

3.3.2 Mineralogy and microstructures

Sample 320 (Fig. 3.2a) has the largest proportion of kyanite (8.54 modal %, Table 3.1). Garnet (up to 8 mm), kyanite (up to 4 mm), and K-feldspar (up to 6 mm) porphyroblasts are set in a finer-grained groundmass of biotite, quartz, K-feldspar, and plagioclase (Fig. 3.3a). Garnet cores contain abundant inclusions of quartz, biotite, and rutile, and polygonal, composite inclusions consisting of lobate quartz surrounded by pools of altered feldspar (Fig. 3.3a, b). The garnet rims are typically inclusion-poor and show minor replacement by biotite. Aluminous sample 244 (Fig. 3.2b) is petrographically similar, though generally finer-grained with elongate garnet porphyroblasts (most 3-4

mm; Fig. 3.3c) containing inclusions of kyanite and apatite, and locally composite inclusions of lobate quartz surrounded by plagioclase (Fig. 3.3d). In both aluminous samples, pods of skeletal kyanite within pools of quartz are found at the interface between adjacent garnet porphyroblasts (e.g. Fig. 3.3d). This feature and the composite inclusions in garnet have been previously interpreted to represent former pools of melt pseudomorphed by quartz or feldspar, enclosing resorbed reactants of the melting reaction. (Indares & Dunning, 2001; Indares et al., 2008; Lasalle & Indares, 2014). In both samples, abundant quartz films around kyanite and biotite and local films of plagioclase or quartz separating garnet and kyanite (Fig. 3.3a, c) are interpreted to be pseudomorphs after melt films. These interpretations are based on the description of such features given by Holness & Sawyer (2008) and Holness et al. (2011).

Sample 100 (Fig. 3.2c) is distinguished from the others by the scarcity of kyanite (0.34 modal %, Table 3.1). Garnet porphyroblasts (up to 4 mm; Fig. 3.3e) show extensive replacement by biotite + plagioclase ± kyanite and are surrounded by a heterogeneous groundmass with three main domains: elongate clusters of biotite + plagioclase + kyanite (Fig. 3.3e); K-feldspar + quartz + muscovite clusters; and quartz ribbons. Small kyanite grains (up to 500 μm) in the groundmass are idioblastic and typically form clusters with biotite, locally replacing garnet (Figs 3.2c, 3.3e); kyanite also appears as xenomorphic inclusions in garnet (Fig. 3.3f), and may themselves be inclusion-rich. Polymineralic, polygonal inclusions in garnet with resorbed kyanite and/or quartz surrounded by a pool of feldspar after former melt (Jordan et al., 2006) are abundant (Fig. 3.3f). Additionally,

interstitial quartz found between K-feldspar crystals is interpreted to represent pseudomorphs after former melt.

In addition, rutile is present in all samples but no ilmenite or magnetite was found, either in the groundmass or as inclusions in other phases (Table 3.1). Therefore, the oxidation state during metamorphism is inferred to have been low. Other minor phases in these samples include Fe-sulphides, which are most abundant in sample 320 (Fig. 3.3b).

As indicated earlier, all samples show evidence for the former presence of partial melt at the thin section scale. The mineral assemblages and microstructures are indicative of biotite dehydration melting, with garnet representing a peritectic product that trapped melt with reactant quartz and/or kyanite, resulting in composite inclusions. Fine-grained, lath-like biotite in the groundmass of each sample and biotite ± plagioclase ± kyanite replacing garnet are inferred to be retrograde, formed during melt crystallisation. The scarcity or lack of retrograde muscovite, which is only present in sample 100, and the preservation of the peak metamorphic assemblage are consistent with melt loss during metamorphism (Indares et al., 2008; White & Powell, 2002), a common feature in rocks undergoing anatexis in a tectonically active setting (Brown, 1994). Possible pre-melt loss bulk compositions of these rocks were calculated by Indares et al. (2008) and Lasalle & Indares (2014; Table 3.2).

3.3.3 CL intensity maps of kyanite

Cathodoluminescence mapping of kyanite crystals revealed complex internal zonation and other structures in samples 320 and 244. All mapped kyanite porphyroblasts

are composite grains, with distinct domains defined by the intensity of the CL emission and truncation of zonation patterns. A small, low CL core is present in some crystals (blue in Fig. 3.4a-c), truncated by a more voluminous, complexly zoned domain with intermediate CL (green, yellow, and/or yellow-orange in Fig. 3.4a-e). This domain, and the low CL core in some grains, are in turn truncated by a high CL, relatively homogeneous rim of variable continuity and thickness (orange or red in Fig. 3.4a-e). In sample 320, one large kyanite grain features protruding overgrowths intergrown with quartz (Fig. 3.4d); these emit strong CL at their cores, comparable to the rim of the main grain. Twins in kyanite can be distinguished by a contrast in CL intensity across a straight, sharp divide, with zonation maintained (Fig. 3.4e). This demonstrates that the crystallographic orientation of the kyanite with respect to the CL detector affects its CL intensity.

Internal structures of kyanite in sample 100 are comparatively simple. Small, xenomorphic inclusions of kyanite in garnet typically have an irregular, mottled pattern in the CL intensity maps (Fig. 3.4f), which may in part result from the numerous inclusions within these kyanite grains. In the groundmass, small, idioblastic kyanite with variable CL intensity among crystals may exhibit subtle oscillatory zonation (Fig. 3.4g). As illustrated by the CL intensity maps of twins, the variability among grains may result from differences in crystallographic orientation. Rarely, these grains have a small core with a mottled CL texture (Fig. 3.4g).

3.3.3.1 Interpretation of kyanite patterns revealed by CL intensity maps

In aluminous rocks, the earliest kyanite produced during prograde metamorphism can be formed by subsolidus reactions (e.g., Chinner, 1965; Spear & Pattison, 2017). Additional kyanite is produced by a muscovite dehydration melting reaction and at higher temperatures, continuous biotite dehydration melting consumes kyanite. However, after the metamorphic peak, new growth of kyanite may occur by operation of the biotite dehydration melting reaction in reverse, during melt crystallisation. Internal structures in kyanite porphyroblasts in samples 320 and 244 are consistent with this general reaction history, revealing three generations of kyanite, Ky1a, Ky1b, and Ky2 (Fig. 3.5); two prograde and one retrograde. The bulk compositions of these samples on an AFM diagram projected from muscovite plot above biotite and below garnet and chlorite (both with and without reintegration of lost melt; Table 3.2 and Fig. 3.6) indicating that the rocks were sufficiently aluminous for production of subsolidus kyanite. Several subsolidus kyanite-producing reactions are therefore possible, such as staurolite breakdown reactions. A subsequent kyanite-consuming reaction caused Ky1a to be strongly embayed (Fig. 3.5) before it was overgrown by Ky1b, creating composite prograde porphyroblasts. Ky1b typically forms the bulk of the porphyroblasts, and is consistent with growing by muscovite dehydration melting, which can produce a large quantity of aluminosilicate. Truncation of the Ky1b porphyroblasts in the CL intensity maps is consistent with resorption by biotite dehydration melting prior to being overgrown by Ky2 rims during melt crystallisation on cooling. Protruding overgrowths such as those observed on one kyanite crystal in sample 320 (Fig. 3.4d) have been previously attributed to melt crystallisation (e.g., Lofgren, 1974). However, aside from this rare feature, retrograde kyanite in these samples is only evident with CL imaging, as

it appears to have preferentially grown as rims on existing kyanite rather than replacing other prograde phases.

In sample 100, only two generations of kyanite are present: inclusions in garnet and groundmass kyanite. The position of the bulk composition of sample 100 projected from muscovite on the AFM diagram (Fig. 3.6) suggests that kyanite was not stable in this rock prior to muscovite breakdown. Consequently, the kyanite inclusions in garnet (Fig. 3.4f) are interpreted to have formed by muscovite dehydration melting and are referred to as Ky1b. This kyanite was subsequently resorbed and encapsulated in peritectic garnet as a result of the biotite dehydration melting reaction. Finally, idioblastic kyanite (Ky2) in the groundmass and replacing garnet rims (Fig. 3.4g) is consistent with renewed production during melt crystallisation upon retrogression. Oscillatory zoning in Ky2 grains further supports growth in the presence of melt, as this feature in metamorphic minerals has been interpreted to result from crystallisation in the presence of a fluid phase (e.g. Yardley et al., 1991). Unlike samples 320 and 244, retrograde kyanite is abundant relative to prograde, and composite kyanite grains are rare. Small, mottled cores in groundmass grains may represent the last vestiges of Ky1b outside of garnet porphyroblasts, and these were too scarce to accommodate all retrograde kyanite. Thus, retrograde kyanite developed as discrete grains locally replacing garnet rims only in sample 100.

3.3.3.2 Calculation of retrograde kyanite proportions

Cathodoluminescence maps of kyanite grains with clear Ky2 rims in samples 320 and 244 were used to estimate the proportion of retrograde kyanite in these samples.

Prograde kyanite cores were cropped from the images, leaving only the retrograde rims, and the areas of the rims were compared to the areas of the whole kyanite grains using ImageJ (Rasband, 2016). These retrograde proportions can be applied to the whole kyanite population of each sample if two assumptions are made: a) that the mapped kyanite crystals are representative; and b) that the cross-sections of the selected kyanite are approximately through the centre of the crystals, thereby exposing the most realistic thickness of Ky2 rims. Unusually high proportions of retrograde kyanite (relative to other crystals in the same sample) are interpreted to indicate significantly off-centre cross-sections; lower proportions are more representative. The results of this exercise indicate that ~ 30 % of the kyanite in sample 320 and ~ 20 % of the kyanite in sample 244 is retrograde (Table 3.3). Owing to the above assumptions and error inherent in processing the images manually, these results are to be considered rough estimates.

The proportion of retrograde kyanite in sample 100 was estimated by a variation of the method above. All kyanite in the groundmass was assumed to be retrograde and all kyanite inclusions in garnet were assumed to be prograde. Thus, the total area of kyanite in the SEM mineralogical map (Fig. 3.2c) was compared to the area of kyanite after cropping out inclusions in garnet. Retrograde groundmass grains were found to be 69 % of all kyanite in the SEM mineralogical map of sample 100. This result is also approximate, as the small prograde cores in a few groundmass grains were not subtracted, though the change would likely be minor.

3.4 Kyanite chemical composition

3.4.1 Methods

Trace elements in kyanite were measured by EPMA and laser ablation-inductively coupled plasma-mass spectrometry (LA-ICP-MS) at Memorial University of Newfoundland. The JEOL JXA-8230 EPMA was operated at 20 kV and 200 nA, with 240 s count time on peak and 120 s on each background, and measured Fe, Ti, V, Mg, Cr, Ba, K, Ca, Na, and Mn during each analysis; Al_2O_3 and SiO_2 were fixed to total 100 % using pure kyanite stoichiometry. Standards were a mix of synthetic and natural materials. A Finnigan Element2 high resolution single collector ICP-MS and a GEOLAS 193 nm ArF Excimer laser were used for in situ LA-ICP-MS analysis, and analyses were internally standardized to the stoichiometric Al content of pure kyanite, with NIST 610 glass (National Institute of Standards and Technology) as the measured primary standard and BCR-2G glass (United States Geological Survey) as a secondary standard (BCR-2G results are given in Table 3.4). The data were processed using the Iolite software (Paton et al., 2011). Spot sizes were 40 μm (a few 30 μm) with an ablation time of 40 s following a ~ 30 s background measurement, fluence of 4 j/cm^2, and pulse frequency of 5 Hz. Aluminium, Si, Cr, Ti, V, Fe, Ba, K, Ca, Na, Mg, Mn, Ga, Li, Zr, Zn, Cu, Ni, and Sc were measured, and of these, the only trace elements consistently above detection limit were Cr, Ti, V, Fe, Mg, and Ga.

All samples were analyzed by both LA-ICP-MS and EPMA, and the same general trends were found in each set of data (all data for each method are available in Appendices 11 and 12 respectively, with analysis positions given in Appendices 13 to 15). Here, LA-ICP-MS data are presented for samples 320 and 244, whereas EPMA data

are presented for sample 100. The LA-ICP-MS data are preferable as the detection limits are lower, however the kyanite inside garnet in sample 100 typically contained abundant inclusions. Most LA-ICP-MS analyses of these grains were contaminated, leaving few usable data for Ky1b; EPMA data are preferred for sample 100 due to the smaller spot size and excitation volume during analysis. Results are reported in Table 3.4.

3.4.2 Trace element patterns

Trace element trends with respect to the different generations of kyanite from samples 320 and 244 are broadly similar. Within the kyanite grains, Cr increases from core to rim, matching CL intensity maps (Fig. 3.7, Table 3.4). Vanadium, Ga, and Fe are generally enriched in the rims (Ky2) relative to intermediate domains (Ky1b), and the low CL cores (Ky1a) tend to have the most variable concentrations of these elements (Fig. 3.7, Table 3.4). In sample 320, Ti shows a general increase from intermediate CL zones (Ky1b) to high CL rims (Ky2; Fig. 3.7); however, in sample 244, the Ti content of rims (Ky2) is equal to or less than that within intermediate domains (Ky1b; Fig. 3.7). Kyanite rims (Ky2) are the most chemically distinct and apparently homogenous group in both samples, as indicated by their tight clustering on V vs. Cr vs. Fe ternary plots (Fig. 3.8a,b); in contrast, core (Ky1a) and intermediate domains (Ky1b) typically overlap considerably. Notably, the kyanite in sample 244 is overall richer in trace elements than those in sample 320, with higher sample averages of Mg, Ti, Cr, Fe, and Ga (Fig. 3.7, Table 3.4).

The two types of kyanite in sample 100 show only minor chemical variation. Groundmass kyanite (Ky2) is generally richer in Ti, poorer in Fe, and more homogenous than kyanite inclusions (Ky1b) (Fig. 3.8c, Table 3.4).

3.4.3 Interpretation of kyanite chemical composition

Linking the trace elements trends in kyanite to particular source minerals is difficult, as in aluminous metamorphic rocks, at least trace amounts of Cr, Ti, Fe, Mg, and V can be found for instance in chlorite, staurolite, muscovite, biotite, and garnet (e.g. Griffen & Ribbe, 1973; Hickmott & Spear, 1992; Yang & Rivers, 2000; Zane et al., 1998). Oxide phases such as ilmenite, magnetite, and rutile may also be reservoirs for these elements (e.g., Dare et al., 2014; Grigsby, 1992; Zack et al., 2004); however, only the latter is present in the samples investigated here. Gallium behaves similarly to Al, and consequently the significance of its patterns is unclear. However, systematic trends within composite kyanite grains in samples 320 and 244 suggest changing partitioning behaviour of some elements with respect to kyanite during metamorphism. Ky2 shows the clearest trends and is generally enriched in Cr, V, and Ga, suggesting that these elements most strongly partitioned into kyanite during melt crystallisation. The source is inferred to be garnet, and the presence of partial melt and high temperatures probably allowed these trace elements to be transported efficiently to sites of kyanite growth. In addition, garnet grown by biotite dehydration melting has been previously identified by the presence of Cr-rich rims on existing garnet porphyroblasts by Spear & Kohn (1996). As garnet is consumed during melt crystallisation, these rims partially break down, which may explain the characteristic Cr enrichment of retrograde kyanite. Differences in

average Cr in kyanite between samples may be a function of the bulk composition of the samples (Müller et al., 2016). Iron in kyanite, assumed to be Fe^{3+}, has been suggested by Chinner et al. (1969) and Müller et al. (2016) to be linked to oxygen fugacity during kyanite growth, as they observed elevated Fe in kyanite in oxidised rocks. The subtle Ky1b to Ky2 Fe enrichment could therefore be indicative of changing fO_2 conditions during metamorphism, though the zonation could also be caused by minerals with different Fe contents breaking down in kyanite-forming reactions (e.g., muscovite vs. garnet). However, overall Fe contents of kyanite in sample 244 are nearly double those in sample 320, suggesting that fO_2 may have varied between the two rocks. The Ti patterns of the porphyroblasts are more complex, as Ky2 is enriched in Ti relative to Ky1b in sample 320, whereas Ky2 may be depleted in sample 244. Müller et al. (2016) found a positive correlation between trace Ti in kyanite and growth temperature, and suggested that Ti incorporation in kyanite is dependent on temperature. Here, however, retrograde rims in each sample formed by the same reaction at similar temperatures, and show different trends relative to prograde kyanite. This suggests that Ti partitioning was not solely dependent on temperature, and that local Ti availability may have been a factor.

Ky1a and Ky1b in samples 320 and 244 can generally be distinguished by Cr content; however, their concentrations of other trace elements typically overlap considerably. This may be the result of two factors: a) the strongly embayed contact between Ky1a and Ky1b, which increases the likelihood of laser ablation analyses sampling both Ky1a and Ky1b in a single pit; and b) irregular zonation in CL images of Ky1a and Ky1b, suggesting more pronounced chemical heterogeneity in the prograde

cores than in Ky2. Chemical heterogeneity in Ky1a and Ky1b can be explained as an inherited feature from reactant minerals that kyanite may have replaced (Yang & Rivers, 2001). In contrast, the relative homogeneity of Ky2 in chemical plots and CL images is consistent with rims overgrowing existing porphyroblasts during melt crystallisation.

Unlike samples 320 and 244, in which kyanite generations are readily distinguished by their contents of Cr and other elements, Ky1b and Ky2 show relatively little chemical distinction in sample 100. This indicates that trace element partitioning between kyanite and other phases proceeded differently in the sub-aluminous sample compared to the aluminous samples, despite each recording similar kyanite-producing and -consuming reactions. The reason for this is unclear, however differences in the reaction history before muscovite dehydration melting and the scarcity of kyanite in sample 100 compared to the aluminous samples could have affected trace element distribution throughout the rock and in the kyanite.

3.5 Phase equilibria modelling

P–T pseudosections were constructed to link internal structures of kyanite and their interpreted reaction history to the predicted equilibrium relationships of mineral assemblages in *P–T* space. Pseudosections were previously produced for these rocks in the NCKFMASHTO system for both measured and melt-reintegrated bulk compositions (Indares et al., 2008; Lasalle & Indares 2014) in order to account for the possibility of melt loss (White & Powell, 2002) using THERMOCALC version 3.33 (updated from Powell & Holland, 1988), the thermodynamic database tcds55 (Holland & Powell, 1998;

updated in 2003), and activity–composition (a–x) models of White et al. (2007) for garnet, biotite, and melt; Holland & Powell (2003) for plagioclase and K-feldspar; and Coggon & Holland (2002) for muscovite. Those calculated with the measured bulk composition (referred to here as residual) were used for modelling the near peak and retrograde history, whereas the melt-reintegrated pseudosections were used to constrain the prograde *P–T* path. However, as these pseudosections could not be modelled with Mn (White et al., 2007), they are not adequate for interpreting prograde kyanite history.

The pseudosections of Indares et al. (2008) and Lasalle & Indares (2014) using the older set of files (referred to as DS55 pseudosections) are reproduced here, along with another set of pseudosections using the updated tcds62 dataset (updated from Holland & Powell, 2011) and set of a–x models for pelitic systems by White et al. (2014a) and White et al. (2014b) (referred to as DS62 pseudosections), which now allow for modelling of anatectic rocks in the MnNCKFMASHTO system. The rock bulk compositions used for these pseudosections are reported in Table 3.2, with O set to 0.05. This minimal O value was chosen to reflect the presence of rutile as the only Fe^{3+}-bearing minor phase in all samples, as there are no independent constraints on bulk Fe^{2+}/Fe^{3+}. Given that the position of the ilmenite in/out boundary is strongly sensitive to O and has little meaning if this value is not quantified, ilmenite has been omitted from the diagrams. The stability field of rutile is therefore expanded to relatively low pressures (~ 6 kb). The effect of increasing O on the relevant assemblages is explored in Appendix 16, with only minor changes to the overall topologies predicted. The pseudosections are used here qualitatively to illustrate kyanite-consuming and -producing reactions, and therefore a

representative O value consistent with the low-Fe^{3+} mineral assemblage is sufficient. The mineral abbreviations used are garnet (g), liquid (liq), biotite (bi), kyanite (ky), sillimanite (sill), plagioclase (pl), K-feldspar (ksp), quartz (q), muscovite (mu), staurolite (st), rutile (ru), ilmenite (ilm), orthopyroxene (opx), and cordierite (cd). In addition to topologies, the calculated pseudosections include isopleths of mol. % kyanite, which on a 1-oxygen basis approximate vol. %.

3.5.1 Aluminous samples

In melt-reintegrated pseudosections (Figs 3.9a,b and 3.10a,b), the lowest *P–T* kyanite-bearing assemblage is pl–liq–mu–ky–bi (± g, ru), in Field I. This field is bound at high pressure by the loss of kyanite, and at high temperature by the muscovite-out and K-feldspar-in boundaries. In the DS62 pseudosections, the appearance of staurolite, disappearance of kyanite, and the water-saturated solidus mark the low *P–T* boundary, whereas garnet-absent topologies partially obscure the low-*P* portion of Field I in DS55 pseudosections, save for the small staurolite-in boundary in the sample 320 pseudosection. Proportions of kyanite calculated in the pseudosections for sample 320 reach a maximum of 8 mol. % at the low-*P* side of Field I, with isopleths of kyanite proportions parallel to the kyanite-out boundary at higher pressure. In contrast, ≤ 1 mol. % is predicted in Field I in pseudosections for sample 244 – the field is too narrow to accommodate significant amounts of kyanite. In pseudosections for both samples, kyanite proportions increase significantly upon crossing the muscovite-out and K-feldspar-in boundaries at the high-*T* side of Field I. Notably, Field I is larger in DS55 pseudosections relative to DS62 pseudosections, as the kyanite-out boundary reaches higher pressures.

Kyanite is predicted to be stable in every field of the residual pseudosections (Figs 3.9c,d and 3.10c,d), most importantly including Field II (g–pl–liq–ksp–ky–bi–ru), in which biotite dehydration melting proceeds with increasing temperature. Field II boundaries are similar in pseudosections for both aluminous samples and regardless of dataset used, bound at high temperature by the loss of biotite, at low temperature by the dry solidus, and at high pressure by the appearance of muscovite and/or loss of plagioclase. However, the location of Field II in *P–T* space differs between datasets, as the dry solidus and biotite-out boundary calculated using DS62 are shifted down-temperature by 30°C to 40°C relative to those in DS55 pseudosections, causing the pressure extent of Field II to decrease by ~ 3 kb. Isopleths of kyanite proportions in this field have a steep d*P*/d*T*, and their locations differ minorly between DS55 and DS62 pseudosections. For sample 320, kyanite predicted at the solidus is ~ 12.5 mol. % with a minimum of ~ 9.5 mol. % at the biotite-out boundary in the DS62 pseudosection, and a range of ~ 7 mol. % to ~ 9.5 mol. % is predicted in the DS55 pseudosection. Kyanite proportions are significantly lower in sample 244 pseudosections, with ~ 2.5 mol. % to ~ 5.5 mol. % in the DS62 pseudosection and ~ 1.5 mol. % to ~ 4.5 mol. % in the DS55 pseudosection.

Pressures reached in Field II were previously estimated by comparing the measured grossular component (X_{grs}) of garnet to calculated X_{grs} isopleths in the pseudosections (Indares et al., 2008; Lasalle & Indares, 2014). The pressure difference corresponding to X_{grs} from cores and rims is ~ 3-5 kb and ~ 2-4 kb from DS55 pseudosections for samples 320 and 244 respectively. Although X_{Fe} of garnet was used to

determine temperatures reached in Field II, the temperatures were inferred to represent minima owing to possible resetting of Mg/Fe in the garnet during cooling (Indares et al., 2008; Lasalle & Indares, 2014). The minimum measured X_{Fe} is predicted relatively near the dry solidus in pseudosections for both samples (Figs 3.9c,d and 3.10c,d); combined with the predicted pressure differences, the retrograde *P–T* paths were interpreted to have a steep d*P*/d*T* with a small temperature range of melt crystallisation.

3.5.1.1 Kyanite reaction history

As the early prograde evolution of the aluminous samples is modelled most accurately with Mn in the system, the kyanite reaction history is evaluated based on DS62 pseudosections (Figs 3.9b,d and 3.10b,d). In melt-reintegrated pseudosections for both aluminous samples, the earliest production of kyanite can be linked to the breakdown of staurolite, which is predicted just beyond the water-saturated solidus. The maximum normalized molar proportion of staurolite predicted before the kyanite-in boundary is 8 mol. % in the sample 320 pseudosection and 0.5 mol. % in the sample 244 pseudosection, comparable to the amount of kyanite predicted just beyond the staurolite-out boundary. With increasing pressure in Field I, kyanite proportions decrease by the multivariant reaction

Kyanite + Biotite ± Plagioclase + Quartz = Garnet + Muscovite

(Spear et al., 1999). This is consistent with the resorption of Ky1a observed in the CL images. The muscovite-out and K-feldspar-in boundaries are reached with an increase in temperature in Field I, representing muscovite dehydration melting. A large fraction of

kyanite is predicted to form at this boundary, corresponding to Ky1b. Kyanite proportions then decrease with increasing temperature through Field II, consistent with resorption of Ky1b by biotite dehydration melting, and increase upon retrograde cooling and melt crystallisation in the same field, resulting in renewed production of kyanite (Ky2).

The internal structures and proportions of different generations of kyanite in these samples can provide information about the *P–T* history of the rocks. The prograde *P–T* path of these rocks is inferred to have included a pressure increase in Field I based on the resorption of Ky1a. In addition, the scarcity of Ky1a is consistent with crossing the muscovite-out boundary at high pressure within Field I. For the near peak and retrograde *P–T* paths in these rocks, proportions of Ky2 are useful. In the DS62 pseudosection for sample 320, kyanite normalized molar proportions calculated in Field II range from ~ 9.5 mol. % at the biotite-out boundary to ~ 12.5 mol. % at the dry solidus; therefore, the maximum amount of retrograde kyanite predicted is ~ 3 mol. %. For sample 244, kyanite proportions calculated for the DS62 pseudosection in Field II range from 3.5 mol. % to 4 mol. % at the biotite-out boundary and 4 mol. % to 5.5 mol. % at the dry solidus, corresponding to 0 to 2 mol. % retrograde kyanite, depending on peak *P–T* and conditions of melt crystallisation. For both samples, the possible proportions of retrograde kyanite calculated in the pseudosections are comparable to the amounts of Ky2 estimated from image analysis (Table 3.3). Although both types of calculations are estimates associated with significant error, they imply a meaningful trend. Minimum proportions of retrograde kyanite (~ 0 mol. %) are achieved with a minimal temperature range of melt crystallisation, and in contrast, maximum retrograde kyanite production

requires a large temperature range of melt crystallisation in Field II. The observed amount of retrograde kyanite in both aluminous samples suggests a significant difference between peak temperature and temperature of melt crystallisation; consequently, the kyanite provides strong evidence that retrograde resetting of X_{Fe} in garnet resulted in underestimation of peak temperatures by Indares et al. (2008) and Lasalle & Indares (2014).

3.5.2 Sub-aluminous sample

Fig. 3.11 shows melt-reintegrated and residual pseudosections calculated for sample 100. Field I, observed in melt-reintegrated pseudosections for the aluminous samples, is not predicted in the sample 100 melt-reintegrated pseudosections and kyanite first appears at the muscovite-out boundary (Fig. 3.11a,b). The *P–T* extent of kyanite stability is relatively limited in the residual pseudosections and although Field II boundaries are similar to those for the aluminous samples, important exceptions include a kyanite-out boundary at high-*T* and low-*P* and the muscovite-in boundary extending to lower pressures (Fig. 3.11c,d). Maximum normalized molar kyanite proportions in Field II are ~ 1.3 mol. % in the DS55 pseudosection and ~ 1.4 mol. % in the DS62 pseudosection, and the isopleths of equal proportion have a steep d*P*/d*T*.

For sample 100, peak pressure conditions were estimated in Field II using isopleths of X_{grs} and minimum peak temperature was estimated from X_{Fe} isopleths (Indares et al., 2008). Conditions of melt crystallisation are further constrained by the appearance of retrograde muscovite (Indares et al., 2008) and the segment of the muscovite-in boundary coinciding with the dry solidus represents the possible range of

melt crystallisation *P–T* conditions. In the DS55 pseudosection, part of this segment also coincides with the measured X_{grs}, consistent with the lack of a X_{grs} decrease at the garnet rims (Indares et al., 2008); however, in the DS62 pseudosection, this segment of the muscovite-in boundary falls below the kyanite/sillimanite transition boundary. As recognized in pseudosections produced for the aluminous samples, the biotite-out boundary and dry solidus are calculated at lower temperatures using DS62 compared to DS55, which causes an overall decrease in the pressure extent of Field II. The pseudosections for sample 100 have been affected more dramatically than the others; the shift has caused Field II to become too narrow to accommodate the *P–T* path inferred from mineral assemblages and garnet chemistry.

3.5.2.1 Kyanite reaction history

The kyanite record in sample 100 is relatively simple and can be explained by the dehydration melting reactions of muscovite and biotite. However, this growth history cannot be accommodated in the DS62 pseudosections for the reasons explained above, and is therefore instead illustrated using the DS55 pseudosections (Fig. 3.11a,c). The first kyanite is predicted to appear with muscovite dehydration melting, consistent with the inferred origin of Ky1b. As shown with the aluminous samples, kyanite proportions decrease in Field II with increasing temperature, consistent with resorption of Ky1b by biotite dehydration melting during heating and production of Ky2 during cooling.

The observed Ky1b and Ky2 proportions in sample 100 can be explained using the pseudosections and have implications for the *P–T* path. However, only near-peak and retrograde *P–T* trends can be inferred, as kyanite appears too late in the prograde history

to add any constraints to the prograde *P–T* path. The low Ky1b:Ky2 ratio suggests that high temperatures were reached in Field II, resulting in extensive consumption of Ky1b. The ~ 70 % proportion of retrograde kyanite estimated from image analysis could have then been produced by a retrograde *P–T* path with a moderate d*P*/d*T*, crossing a large temperature range before reaching the dry solidus. This type of retrograde *P–T* path for sample 100 was previously proposed by Jordan et al. (2006) and Indares et al. (2008).

3.5.3 Discussion

The internal structures of kyanite in these samples are consistent with phase equilibria models, and add constraints to the *P–T* paths of the rocks (Fig. 3.12). In the aluminous samples, the earliest kyanite cores have implications for the prograde evolution prior to muscovite dehydration melting. The first kyanite (Ky1a) may be linked to staurolite breakdown, though not necessarily near the water-saturated solidus as depicted in the pseudosections – significant error is associated with the position of the staurolite field in *P–T* space, as a–x relations for staurolite are difficult to model (White et al., 2014b). Although Ky1a trace element composition may have been inherited from the phase it replaced, the trace elements found in Ky1a cannot be used to identify it, because many other minerals in aluminous metamorphic rocks can contain these elements. Therefore, a staurolite-out reaction is inferred here as the origin of the earliest kyanite in these samples based solely on the pseudosections. Reaction overstepping could have allowed for production of kyanite before or alongside staurolite (Spear & Pattison, 2017), however the likelihood of this cannot be assessed here. Next, the resorbed form of Ky1a is consistent with increasing pressure in Field I and the small amount of Ky1a

observed suggests that the rocks reached high pressures in this field (Fig. 3.12). This evolution is evidently reasonable for sample 320, however Field I is too small in the 244 DS62 pseudosection for kyanite to be consumed by increasing pressure, inconsistent with resorbed Ky1a cores in this sample. The pressure increase may be plausible if the size of Field I has been underestimated for sample 244. Overall, identifying Ky1a and linking it to phase equilibria models has provided for the first time firm constraints on the prograde *P–T* path before muscovite dehydration melting in these rocks.

Identifying retrograde kyanite in these samples has allowed for better constraints on the retrograde *P–T* path in Field II. As isopleths of kyanite proportions have a steep d*P*/d*T* in this field, a *P–T* path with a small temperature range of melt crystallisation would produce little to no retrograde kyanite; by contrast, significant cooling within Field II would allow retrograde kyanite to grow. In sub-aluminous rocks like sample 100, kyanite may disappear before biotite at the high-*T* and low-*P* corner of Field II. The small amount of Ky1b predicted to be produced combined with a relatively high peak temperature in this field would cause little kyanite to remain after prograde metamorphism. Although kyanite has been shown here to preferentially nucleate on existing kyanite, the small amount of Ky1b would provide few nucleation sites for Ky2, and thus most retrograde kyanite would nucleate instead on garnet rims, as was observed in sample 100. For aluminous samples like 320 and 244, kyanite is predicted to outlast biotite during biotite dehydration melting, and a relatively large proportion of kyanite should remain after prograde metamorphism. Retrograde kyanite in such rocks would therefore be expected to appear as overgrowths on existing kyanite rather than

replacements after garnet. Without the means to identify retrograde kyanite in composite porphyroblasts, Indares et al. (2008) and Lasalle & Indares (2014) previously interpreted that the amount of retrograde kyanite in samples 320 and 244 was negligible, consistent with peak temperatures close to the dry solidus and steep *P–T* paths. However, the results of this work suggest that this evolution should be modified to include a larger temperature range of melt crystallisation, and consequently higher peak temperature (Fig. 3.12). The peak temperature need not be restricted to Field II, as there are no clear constraints on whether the biotite-out boundary was exceeded. These results suggest that in high-*P,* anatectic, aluminous granulites similar to those investigated here, it is difficult to evaluate the amount of retrograde kyanite without CL imaging, which in turn can mislead interpretations of retrograde *P–T* paths.

Although the pseudosections suggest that prograde dissolution and retrograde growth of kyanite are gradual, continuous processes, kinetic barriers may have caused overstepping of the isopleths of equal kyanite proportions in Fields I and II (Pattison et al., 2011). Significant overstepping would result in apparently continuous reactions proceeding episodically. Although the CL images can only provide the net result of kyanite resorption/growth during metamorphism, Ky2 rims in the aluminous samples provide possible evidence of episodic growth. The relative homogeneity of Ky2 in the CL images (Fig. 3.4a-e) is more consistent with a single growth phase rather than continuous growth during melt crystallisation, and the Ky2 rim with protruding overgrowths on one kyanite crystal (Fig. 3.4d) is suggestive of Ky2 growth in two episodes.

3.5.4 Remarks on THERMOCALC datasets

This work has revealed significant differences between pseudosections produced using the older DS55 dataset and the new DS62 dataset for these samples. The latter shows a relative shift toward lower pressure for most fields by ~ 3 kb, that in this case is mainly the result of the biotite-out boundary and dry solidus moving toward lower temperature by 30° to 40° C relative to the muscovite-out boundary, which is identical in both diagrams. The result is the *P–T* extent of Fields I and II above the kyanite/sillimanite boundary becoming smaller. Although the comparison between the two datasets is made here using pseudosections produced in different chemical systems, DS62 pseudosections including Mn and DS55 pseudosections without, DS62 pseudosections produced without Mn (not shown here) indicate that the discrepancies persist regardless of the chemical system used. The very narrow Field I in the sample 244 melt-reintegrated pseudosection is inconsistent with the presence of resorbed Ky1a in this sample and Field II in the residual pseudosection for sample 100 is unable to accommodate retrograde muscovite. Consequently, DS55 pseudosections are overall preferable for representing the *P–T* paths of these samples. Melting experiments have shown that significant fluorine in biotite stabilizes it to higher temperatures (Dooley & Patiño Douce, 1996; Peterson et al., 1991), and thus the absence of fluorine in the models may have caused the biotite-out boundary to shift toward unrealistically low temperatures in the DS62 pseudosections. This effect may have been obscured in the DS55 pseudosections by other issues that have been addressed by the substantially updated new activity models for biotite and other minerals (White et al., 2014b).

Significant differences between pseudosections produced for the same rock using the DS55 and DS62 datasets have been recognized by previous workers for sillimanite-bearing UHT aluminous rocks (Guevara & Caddick, 2016; Korhonen et al., 2014). Korhonen et al. (2014) found that UHT assemblages predicted by the DS62 pseudosection were more compatible with observations from the sample than the DS55 pseudosections. They noted that several topologies had shifted toward lower pressure, and that the biotite-out boundary decreased in temperature by 50°C. In contrast, Guevara & Caddick (2016) found that some UHT equilibrium assemblages observed in the rock were predicted by DS55 pseudosections, but not found in DS62 pseudosections.

3.6 Summary and conclusions

Kyanite is an essential constituent of high-*P* anatectic aluminous rocks, and may contain a record of the metamorphic history of a rock within a single crystal. In the aluminous samples examined here, CL imaging has revealed that kyanite porphyroblasts are composite crystals, with three distinct generations separated by resorbed interfaces. In contrast, kyanite in the sub-aluminous sample is found in two separate textual settings, one as inclusions in garnet and the second in the groundmass and replacing garnet. Kyanite in all samples contains the same suite of trace elements, with different relative abundances between generations in composite crystals, giving rise to their contrasting CL signatures. Kyanite and its growth structures can be linked to a reaction history consistent with phase equilibria models. The earliest cores (Ky1a) in aluminous samples are the oldest identifiable relicts of prograde metamorphism in these rocks, and may be linked to

the breakdown of a subsolidus phase such as staurolite. The next two generations are connected to the two most significant anatectic reactions in these rocks, with the second (Ky1b) produced by muscovite dehydration melting and subsequently resorbed by continuous dehydration melting of biotite. The latest kyanite (Ky2) in both aluminous and sub-aluminous samples formed during melt crystallisation during retrograde metamorphism, and the amount of retrograde kyanite can add constraints to the temperature range of melt crystallisation. In aluminous rocks, retrograde kyanite appears only in composite porphyroblasts and cannot be recognized without CL imaging.

This contribution has highlighted three key points regarding high-*P*, anatectic, aluminous granulites. First, CL imaging or mapping holds great potential for revealing details of mineral growth history, as it can highlight internal structures in metamorphic minerals preserved only by trace element distribution. Trace elements can preserve primary growth zonation in detail; however, this chemical variation may be too subtle to be seen clearly by other methods such as X-ray mapping. In chemically simple minerals, such as aluminosilicates, trace element distribution may be the only information preserving a record of growth history. For instance, we have shown here that Cr, and to a lesser extent V, Ti, Fe, and Ga, have the potential to record growth zoning, and reveal other internal structures, within kyanite porphyroblasts, and that CL maps match Cr distribution closely. Cathodoluminescence imaging of growth zonation is already routine for geochronologic studies involving metamorphic zircon, and application to metamorphic quartz is proving to be fruitful (e.g., Kendrick & Indares, submitted; Korchinski et al., 2012; Storm & Spear, 2009).

Second, we have demonstrated that kyanite porphyroblasts can be remarkably complex, resulting from the tendency of new kyanite to overgrow existing kyanite. In high grade metamorphic rocks, similar complexity has long been recognized in zircon and has also been investigated in garnet (e.g., Spear & Kohn, 1996), but is typically not considered for most other minerals. Examination of composite kyanite porphyroblasts can add constraints to the *P–T* evolution and metamorphic history of the rock; however, without the proper imaging tools, this information can easily be missed.

Lastly, we have shown that the newest Holland & Powell (2011) database and a–x models of White et al. (2014b) may have limitations for phase equilibria modelling of high-*P*, anatectic, aluminous rocks. Although all the necessary topologies can be modelled, changes to the thermodynamic dataset and a–x models have caused a decrease in the pressure extent of important fields above the kyanite/sillimanite transition. As a result, these fields become unable to accommodate the *P–T* evolution of the rocks inferred from mineralogy and textures. This finding warrants further studies comparing the two datasets for the same bulk compositions to determine the extent of such discrepancies.

Acknowledgments

This research was funded by an NSERC discovery grant to AI, and all samples were previously collected by AI. We gratefully acknowledge the assistance of Wanda Aylward in the EPMA lab, Markus Wälle in the LA-ICP-MS lab, and David Grant and

Dylan Goudie with the collection of SEM mineralogical maps. This work has benefitted from several insightful discussions with Greg Dunning, and we thank Roger Mason and John Hanchar for comments on the manuscript. Constructive reviews by Tim Johnson and an anonymous reviewer improved the clarity of this work, and Michael Brown is thanked for editorial handling of the manuscript.

References

Brown, M. (1994). The generation, segregation, ascent and emplacement of granite magma: The migmatite-to-crustally-derived granite connection in thickened orogens. Earth-Science Reviews, 36, 83–130.

Brown, M. (2013). Granite: From genesis to emplacement. Geological Society of America Bulletin, 125, 1079–1113.

Brown, M., & Korhonen, F.J. (2009). Some remarks on melting and extreme metamorphism of crustal rocks. In A.K. Gupta & S. Dasgupta (Eds.), Physics and chemistry of the Earth's interior (pp. 67–87). New York, NY: Springer.

Carrington, D.P., & Harley, S.L. (1995). Partial melting and phase relations in high-grade metapelites: An experimental petrogenetic grid in the KFMASH system. Contributions to Mineralogy and Petrology, 120, 270–291.

Chinner, G.A. (1965). The kyanite isograd in Glen Clova, Angus, Scotland. Mineralogical Magazine, 34, 132–143.

Chinner, G.A., Smith, J.V., & Knowles, C.R. (1969). Transition-metal contents of Al2SiO5 polymorphs. American Journal of Science, 267, 96–113.

Clemens, J. D. (2006). Melting of the continental crust: Fluid regimes, melting reactions, and source-rock fertility. In M. Brown & T. Rushmer (Eds.), Evolution and differentiation of the continental crust (pp. 297–331). Cambridge, UK: Cambridge University Press.

Coggon, R., & Holland, T.J.B. (2002). Mixing properties of phengitic micas and revised garnet-phengite thermobarometers. Journal of Metamorphic Geology, 20, 683–696.

Dare, S.A.S., Barnes, S.-J., Beaudoin, G., Méric, J., Boutroy, E., & Potvin-Doucet, C. (2014). Trace elements in magnetite as petrogenetic indicators. Mineralium Deposita, 49, 785–796.

Dooley, D.F., & Patiño Douce, A.E. (1996). Fluid-absent melting of F-rich phlogopite + rutile + quartz. American Mineralogist, 81, 202–212.

Dunning, G., & Indares, A. (2010). New insights on the 1.7–1.0 Ga crustal evolution of the central Grenville Province from the Manicouagan – Baie Comeau transect. Precambrian Research, 180, 204–226.

Ferri, F., Poli, S., & Vielzeuf, D. (2009). An experimental determination of the effect of bulk composition on phase relationships in metasediments at near-solidus conditions. Journal of Petrology, 50, 909–931.

García-Casco, A., Haissen, F., Castro, A., El-Hmidi, H., Torres-Roldán, R.L., & Millán, G. (2003). Synthesis of staurolite in melting experiments of a natural metapelite: Consequences for the phase relations in low-temperature pelitic migmatites. Journal of Petrology, 44, 1727–1757.

Gardien, V., Thompson, A.B., Grujic, D., & Ulmer, P. (1995). Experimental melting of biotite + plagioclase + quartz ± muscovite assemblages and implications for crustal melting. Journal of Geophysical Research, 100, 15581–15591.

Griffen, D.T., & Ribbe, P.H. (1973). The crystal chemistry of staurolite. American Journal of Science, 273, 479–495.

Grigsby, J.D. (1992). Chemical fingerprinting in detrital ilmenite: A viable alternative in provenance research? Journal of Sedimentary Petrology, 62, 331–337.

Guevara, V.E., & Caddick, M.J. (2016). Shooting at a moving target: Phase equilibria modelling of high-temperature metamorphism. Journal of Metamorphic Geology, 34, 209–235.

Guilmette, C., Indares, A., & Hébert, R. (2011). High-pressure anatectic paragneisses from the Namche Barwa, Eastern Himalayan Syntaxis: Textural evidence for partial melting, phase equilibria modeling and tectonic implications. Lithos, 124, 66–81.

Herz, N., & Dutra, C.V. (1964). Geochemistry of some kyanites from Brazil. The American Mineralogist, 49, 1290–1305.

Hickmott, D., & Spear, F.S. (1992). Major- and trace-element zoning in garnets from calcareous pelites in the NW Shelburne Falls Quadrangle, Massachusetts: Garnet growth histories in retrograded rocks. Journal of Petrology, 33, 965– 1005.

Hietanen, A. (1956). Kyanite, andalusite, and sillimanite in the schist in Boehls Butte Quadrangle, Idaho. The American Mineralogist, 41, 1–27.

Hodych, J.P., & Dunning, G.R. (1992). Did the Manicouagan impact trigger end-of-Triassic mass extinction? Geology, 20, 51–54.

Holland, T.J.B., & Powell, R. (1998). An internally consistent thermodynamic data set for phases of petrological interest. Journal of Metamorphic Geology, 16, 309–343.

Holland, T.J.B., & Powell, R. (2003). Activity-composition relations for phases in petrological calculations: An asymmetric multicomponent formulation. Contributions to Mineralogy and Petrology, 145, 492–501.

Holland, T.J.B., & Powell, R. (2011). An improved and extended internally consistent thermodynamic dataset for phases of petrological interest, involving a new equation of state for solids. Journal of Metamorphic Geology, 29, 333–383.

Holness, M.B., & Sawyer, E.W. (2008). On the pseudomorphing of melt-filled pores during the crystallization of migmatites. Journal of Petrology, 49, 1343–1363.

Holness, M.B., Cesare, B., & Sawyer, E.W. (2011). Melted rocks under the microscope: Microstructures and their interpretation. Elements, 7, 247–252.

Huang, W.L., & Wyllie, P.J. (1974). Melting relations of muscovite with quartz and sanidine in the K2O-Al2O3-SiO2-H2O system to 30 kilobars and an outline of paragonite melting relations. American Journal of Science, 274, 378–395.

Huang, W.L., & Wyllie, P.J. (1975). Melting reactions in the system NaAlSi3O8-KAlSi3O8-SiO2 to 35 kbar, dry and with excess water. Journal of Geology, 83, 737–748.

Indares, A. (1993). Eclogitized gabbros from the eastern Grenville Province: Textures, metamorphic context, and implications. Canadian Journal of Earth Sciences, 30, 159–173.

Indares, A. (1995). Metamorphic interpretation of high-pressure–temperature metapelites with preserved growth zoning in garnet, eastern Grenville Province, Canadian Shield. Journal of Metamorphic Geology, 13, 475–486.

Indares, A., & Dunning, G. (2001). Partial melting of high-P–T metapelites from the Tshenukutish terrane (Grenville Province): Petrography and U–Pb geochronology. Journal of Petrology, 42, 1547–1565.

Indares, A., White, R.W., & Powell, R. (2008). Phase equilibria modelling of kyanite-bearing anatectic paragneisses from the central Grenville Province. Journal of Metamorphic Geology, 26, 815–836.

Jordan, S.L., Indares, A., & Dunning, G. (2006). Partial melting of metapelites in the Gagnon terrane below the high-pressure belt in the Manicouagan area (Grenville Province): Pressure–temperature (P–T) and U–Pb age constraints and implications. Canadian Journal of Earth Sciences, 38, 1309–1329.

Korchinski, M., Little, T.A., Smith, E., & Millet, M.-A. (2012). Variation of Ti-in-quartz in gneiss domes exposing the world's youngest ultrahigh-pressure rocks, D'Entrecasteaux Islands, Papua New Guinea. Geochemistry, Geophysics, Geosystems, 13, 1–27.

Korhonen, F.J., Clark, C., Brown, M., & Taylor, R.J.M. (2014). Taking the temperature of Earth's hottest crust. Earth and Planetary Science Letters, 408, 341–354.

Lasalle, S., & Indares, A. (2014). Anatectic record and contrasting P–T paths of aluminous gneisses from the central Grenville Province. Journal of Metamorphic Geology, 32, 627–646.

Le Breton, N., & Thompson, A.B. (1988). Fluid-absent (dehydration) melting of biotite in metapelites in the early stages of crustal anatexis. Contributions to Mineralogy and Petrology, 99, 226–237.

Lofgren, G. (1974). An experimental study of plagioclase crystal morphology: Isothermal crystallization. American Journal of Science, 274, 243–273.

Müller, A., van den Kerkhof, A.M., Selbekk, R.S., & Broekmans, M.A.T.M. (2016). Trace element composition and cathodoluminescence of kyanite and its petrogenetic implications. Contributions to Mineralogy and Petrology, 171, 70.

O'Brien, P.J., & Rötzler, J. (2003). High-pressure granulites: Formation, recovery of peak conditions and implications for tectonics. Journal of Metamorphic Geology, 21, 3–20.

Patiño Douce, A.E., & Johnston, A.D. (1991). Phase equilibria and melt productivity in the pelitic system: Implications for the origin of peraluminous granitoids and aluminous granulites. Contributions to Mineralogy and Petrology, 107, 202–218.

Paton, C., Hellstrom, J., Paul, B., Woodhead, J., & Hergt, J. (2011). Iolite: Freeware for the visualisation and processing of mass spectrometric data. Journal of Analytical Atomic Spectrometry, 26, 2508–2518.

Pattison, D.RM., De Capitani, C., & Gaidies, F. (2011). Petrological consequences of variations in metamorphic reaction affinity. Journal of Metamorphic Geology, 9, 953–977.

Pearson, G.R., & Shaw, D.M. (1960). Trace elements in kyanite, sillimanite and andalusite. The American Mineralogist, 45, 808–817.

Peterson, J.W., Chacko, T., & Kuehner, S.M. (1991). The effects of fluorine on the vapor-absent melting of phlogopite + quartz: Implications for deep-crustal processes. American Mineralogist, 76, 470–476.

Powell, R., & Holland, T.J.B. (1988). An internally consistent dataset with uncertainties and correlations: 3. applications to geobarometry, worked examples and a computer program. Journal of Metamorphic Geology, 6, 173–204.

Rasband, W.S. (2016). ImageJ, U. S. National Institutes of Health, Bethesda, Maryland, USA, https://imagej.nih.gov/ij/.

Rivers, T. (1983). Progressive metamorphism of pelitic and quartzofeldspathic rocks in the Grenville Province of western Labrador – tectonic implications of bathozone 6 assemblages. Canadian Journal of Earth Sciences, 20, 1791–1804.

Rivers, T., Culshaw, N., Hynes, A., Indares, A., Jamieson, R., & Martignole, J. (2012). The Grenville orogen – a post lithoprobe perspective. In J.A. Percival, F.A. Cook, & R.M. Clowes (Eds.), Tectonic Styles in Canada: The Lithoprobe Perspective (pp. 97–236). Geological Survey of Canada, Special Paper 49.

Rivers, T., Ketchum, J., Indares, A., & Hynes, A. (2002). The High Pressure belt in the Grenville Province: Architecture, timing, and exhumation. Canadian Journal of Earth Sciences, 39, 867–893.

Rivers, T., Martignole, J., Gower, C.F., & Davidson, A. (1989). New tectonic divisions of the Grenville Province, southeast Canadian Shield. Tectonics, 8, 63–84.

Schertl, H.-P., Neuser, R.D., Sobolev, N.V., & Shatsky, V.S. (2004). UHP-metamorphic rocks from Dora Maira/Western Alps and Kokchetav/Kazakhstan: New insights using cathodoluminescence petrography. European Journal of Mineralogy, 16, 49–57.

Spear, F.S., & Kohn, M.J. (1996). Trace elements zoning in garnet as a monitor of crustal melting. Geology, 24, 1099–1102.

Spear, F.S., Kohn, M.J., & Cheney, J.T. (1999). P-T paths from anatectic pelites. Contributions to Mineralogy and Petrology, 134, 17–32.

Spear, F.S., & Pattison, D.R.M. (2017). The implications of overstepping for metamorphic assemblage diagrams (MADs). Chemical Geology, 457, 38–46.

Storm, L.C., & Spear, F.S. (2009). Application of the titanium-in-quartz thermometer to pelitic migmatites from the Adirondack Highlands, New York. Journal of Metamorphic Geology, 27, 479–494.

Tohver, E., Bettencourt, J.S., Tosdal, R., Mezger, K., Leite, W.B., & Payolla, B.L. (2004). Terrane transfer during the Grenville orogeny: Tracing the Amazonian

ancestry of southern Appalachian basement through Pb and Nd isotopes. Earth and Planetary Science Letters, 228, 161–176.

Vielzeuf, D., & Clemens, J.D. (1992). The fluid-absent melting of phlogopite + quartz: Experiments and models. American Mineralogist, 77, 1206–1222.

Vielzeuf, D., & Holloway, J.R. (1988). Experimental determination of the fluid-absent melting relations in the pelitic system: Consequences for crustal differentiation. Contributions to Mineralogy and Petrology, 98, 257–276.

White, R.W., & Powell, R. (2002). Melt loss and the preservation of granulite facies mineral assemblages. Journal of Metamorphic Geology, 20, 621–632.

White, R.W., Powell, R., & Holland, T.J.B. (2007). Progress relating to calculation of partial melting equilibria for metapelites. Journal of Metamorphic Geology, 25, 511–527.

White, R.W., Powell, R., & Johnson, T.E. (2014a). The effect of Mn on mineral stability in metapelites revisited: New a–x relations for manganese-bearing minerals. Journal of Metamorphic Geology, 32, 809–828.

White, R.W., Powell, R., Holland, T.J.B., Johnson, T.E., & Green, E.C.R. (2014b). New mineral activity–composition relations for thermodynamic calculations in metapelitic systems. Journal of Metamorphic Geology, 32, 261–286.

Wojtowicz, A.J. (1991). Luminescence of Cr3+ in kyanite. Journal of Luminescence, 50, 221–230.

Yang, P., & Rivers, T. (2000). Trace element partitioning between coexisting biotite and muscovite from metamorphic rocks, Western Labrador: Structural, compositional and thermal controls. Geochimica et Cosmochimica, 64, 1451–1472.

Yang, P., & Rivers, T. (2001). Chromium and manganese zoning in pelitic garnet and kyanite: Spiral, overprint, and oscillatory (?) zoning patterns and the role of growth rate. Journal of Metamorphic Geology, 19, 455–474.

Yardley, B.W.D., Rochelle, C.A., Barnicoat, A.C., & Lloyd, G.E. (1991). Oscillatory zoning in metamorphic minerals: An indicator of infiltration metasomatism. Mineralogical Magazine, 55, 357–365.

Zack, T., von Eynatten, H., & Kronz, A. (2004). Rutile geochemistry and its potential use in quantitative provenance studies. Sedimentary Geology, 171, 37–58.

Zane, A., Sassi, R., & Guidotti, C.V. (1998). New data on metamorphic chlorite as a petrogenetic indicator mineral, with special regard to greenschist-facies rocks. The Canadian Mineralogist, 36, 713–726.

Table 3.1. Mineral modal proportions (mol. %) calculated by SEM-MLA.

Sample	Q	G	Ky	Bi	Ksp	Pl	Mu	Ap	Rt	Total
320	24.32	14.00	8.54	17.65	17.33	17.24	0.00	0.01	0.04	99.13
244	24.29	19.27	3.70	11.94	21.09	18.71	0.00	0.37	0.14	99.51
100	25.89	13.79	0.34	16.31	11.11	29.15	1.63	0.02	0.14	98.38

Table 3.2. Bulk compositions (mol.%) of each sample and bulk compositions after melt reintegration, from Indares et al. (2008) and Lasalle & Indares (2014). Details about calculating melt-reintegrated bulk compositions are in Indares et al. (2008). For sample 244, Lasalle & Indares (2014) removed CaO of apatite from the bulk CaO.

Sample bulk compositions											
Sample	H_2O	SiO_2	$Al2O_3$	CaO	MgO	FeO	K2O	Na_2O	TiO_2	MnO	Total
320	2.15	64.59	13.31	1.19	5.58	7.58	2.77	1.83	0.71	0.17	99.88
244	1.38	64.92	11.71	2.22	7.32	6.95	3.03	1.59	0.63	0.14	99.89
100	2.07	69.24	10.57	2.66	3.19	6.36	2.62	2.57	0.72	0.16	100.16
Melt-reintegrated bulk compositions											
320	5.99	63.48	12.52	1.13	4.81	6.56	2.72	2.19	0.61	0.15	100.16
244	6.39	63.73	10.98	2.07	5.77	5.52	3.09	1.92	0.49	0.11	100.07
100	5.40	67.70	10.16	2.42	2.79	5.58	2.67	2.66	0.63	0.14	100.15

Table 3.3. Proportions of retrograde (ret.) kyanite calculated by image analysis of CL maps (samples 320 and 244) or an SEM mineralogical map (sample 100), with the corresponding sample modal proportions of retrograde and prograde (pro.) kyanite.

* Representative value chosen for the kyanite population, justification in text.

Sample 320	Image % ret.	Modal % ret.	Modal % pro.
Kyanite 1	66		
Kyanite 2	30		
Kyanite 3	32		
Kyanite 4	32		
All kyanite*	30	2.56	5.98
Sample 244			
Kyanite 1	24		
Kyanite 2	36		
Kyanite 3	19		
Kyanite 4	17		
Kyanite 5	17		
All kyanite*	20	0.74	2.96
Sample 100			
All kyanite	69	0.23	0.11

Table 3.4. Kyanite trace element chemistry, all values in ppm. Sample SD is population standard deviation and technique SD is analysis standard error, 1σ. MDL = minimum detection limit.

[a] Based on 16 analyses.
[b] Based on 7 analyses.
[c] 7 analyses below MDL, reported as half of MDL (23 ppm).
[d] 3 analyses below MDL, reported as half of MDL (23 ppm).
[e] SD for range of kyanite trace element data

Sample 320 (LA-ICP-MS)	Mg	SD	Ti	SD	V	SD	Cr	SD	Fe	SD	Ga	SD	n
Lowest CL core	42	*16*	62	*27*	109	*37*	104	*61*	2549	*191*	55	*20*	5
Intermediate CL core	43	*11*	58	*20*	106	*38*	233	*72*	2386	*233*	50	*16*	11
High CL rim	54[a]	*9*	82	*13*	194	*9*	491	*48*	2654	*120*	65	*4*	17
All analyses	49	*12*	71	*21*	151	*51*	347	*166*	2549	*214*	58	*14*	33
Sample 244 (LA-ICP-MS)													
Lowest CL core	76[b]	*11*	120	*14*	111	*26*	288	*151*	5134	*509*	62	*9*	8
Intermediate CL core	72	*14*	128	*21*	134	*39*	541	*199*	5212	*486*	66	*12*	12
High CL rim	69	*17*	103	*49*	174	*22*	952	*171*	5497	*378*	72	*5*	9
All analyses	72	*15*	118	*33*	140	*40*	598	*314*	5279	*486*	67	*11*	29
Sample 100 (EPMA)													
Inclusion in garnet	<MDL	*N/A*	40[c]	*18*	210	*36*	610	*222*	2766	*1086*	N/A	*N/A*	14
Groundmass	<MDL	*N/A*	65[d]	*26*	203	*38*	689	*61*	1703	*254*	N/A	*N/A*	12
All analyses	<MDL	*N/A*	52	*25*	207	*37*	646	*173*	2275	*972*	N/A	*N/A*	26
BCR-2G (LA-ICP-MS)	20598	*361*	12651	*182*	429	*6*	16	*1*	97979	*1803*	23	*1*	

	Mg		Ti		V		Cr		Fe		Ga	
Technique	MDL	SD	MDL	SD	MDL	SD	MDL	SD	MDL	SD	MDL	SD
LA-ICP-MS[e]	2	1	1-2	2-3	<1	1-2	≤10	≤10	≤55	≤70	<1	1
EPMA	70	4	45	4	42	4	78	6-7	282	≤30	N/A	N/A

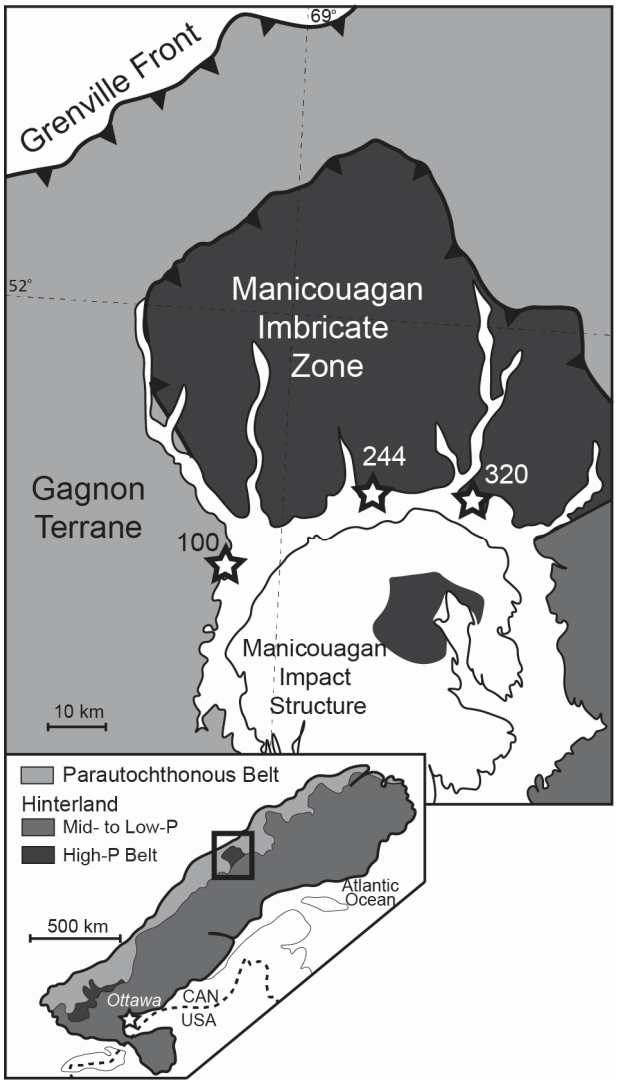

Figure 3.1. Schematic regional geological map (after Dunning & Indares, 2010) of the Manicouagan area in the central Grenville Province and location of the samples.

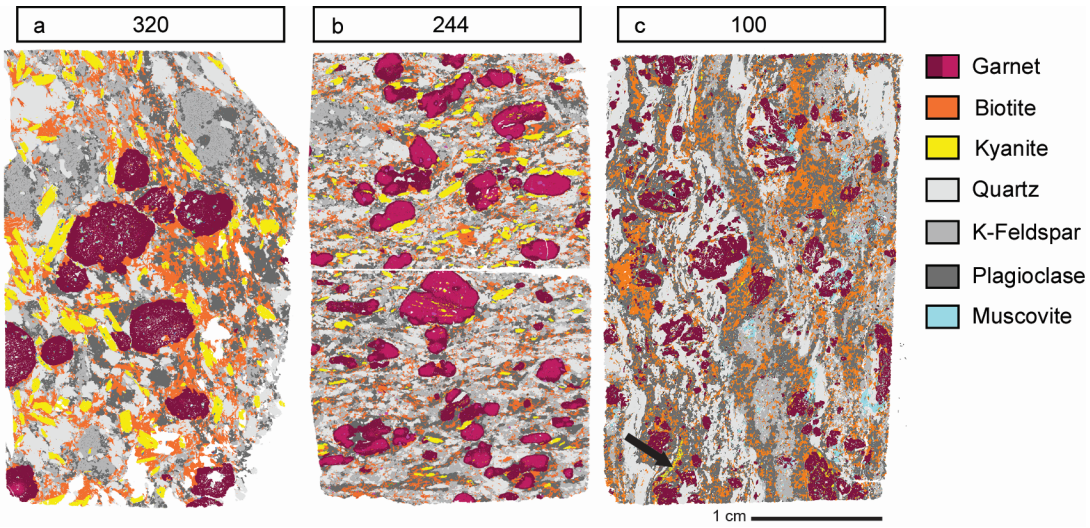

Figure 3.2. False-colour mineralogical maps of each thin section collected by SEM mapping. (a) Sample 320: large garnet and kyanite porphyroblasts are prominent, with randomly distributed groundmass phases. (b) Sample 244: elongate garnet and kyanite define a fabric in a fine-grained groundmass. (c) Sample 100: xenomorphic garnet grains are set in a heterogeneous groundmass with scarce, small kyanite; arrow indicates kyanite cluster.

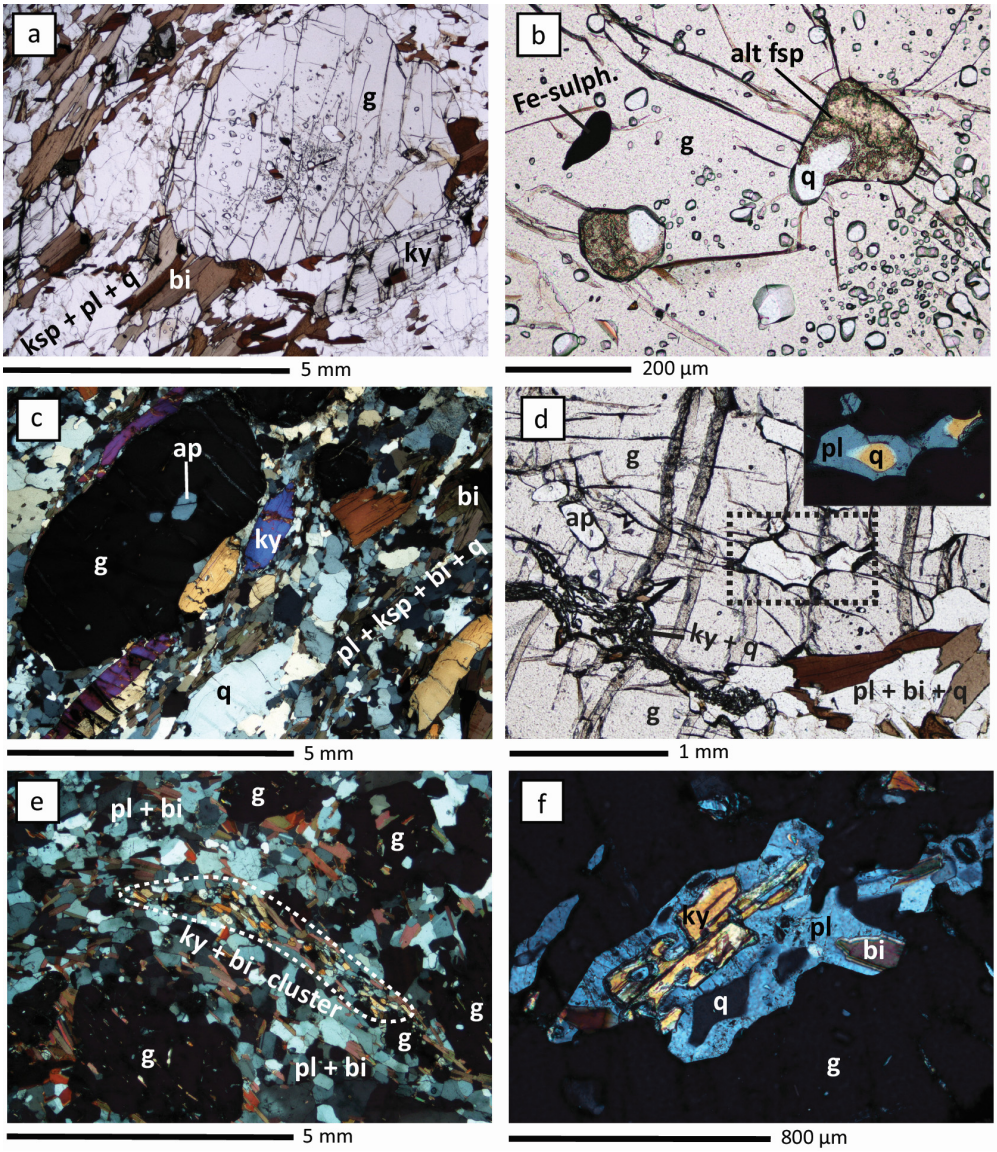

Figure 3.3. Photomicrographs showing key petrographic features in each thin section. (a) Sample 320: inclusion-rich garnet porphyroblast with rims partly replaced by biotite, adjacent to a kyanite porphyroblast, both surrounded by K-feldspar, plagioclase, quartz, and biotite (PPL). (b) Sample 320: magnified view of inclusions in garnet. Two composite inclusions comprise lobate quartz and brown, altered feldspar (PPL). (c) Sample 244: elongate garnet porphyroblast and kyanite porphyroblasts set in a fine-grained groundmass of plagioclase, K-feldspar, biotite, and quartz (XPL). (d) Sample 244: contact between two garnet porphyroblasts. Between them is an intergrowth of skeletal kyanite and quartz (PPL); inset shows composite inclusions in garnet comprising lobate quartz surrounded by a pool of plagioclase (XPL). (e) Sample 100: xenomorphic garnet associated with a biotite + plagioclase + kyanite domain. Fine-grained kyanite is associated with biotite in a discrete cluster (XPL). (f) Sample 100: composite inclusion within a garnet porphyroblast. Strongly resorbed kyanite and lobate quartz are surrounded by a continuous crystal of plagioclase (XPL). Abbreviations: q = quartz, g = garnet, ky = kyanite, bi = biotite, ksp = K-feldspar, pl = plagioclase, ap = apatite.

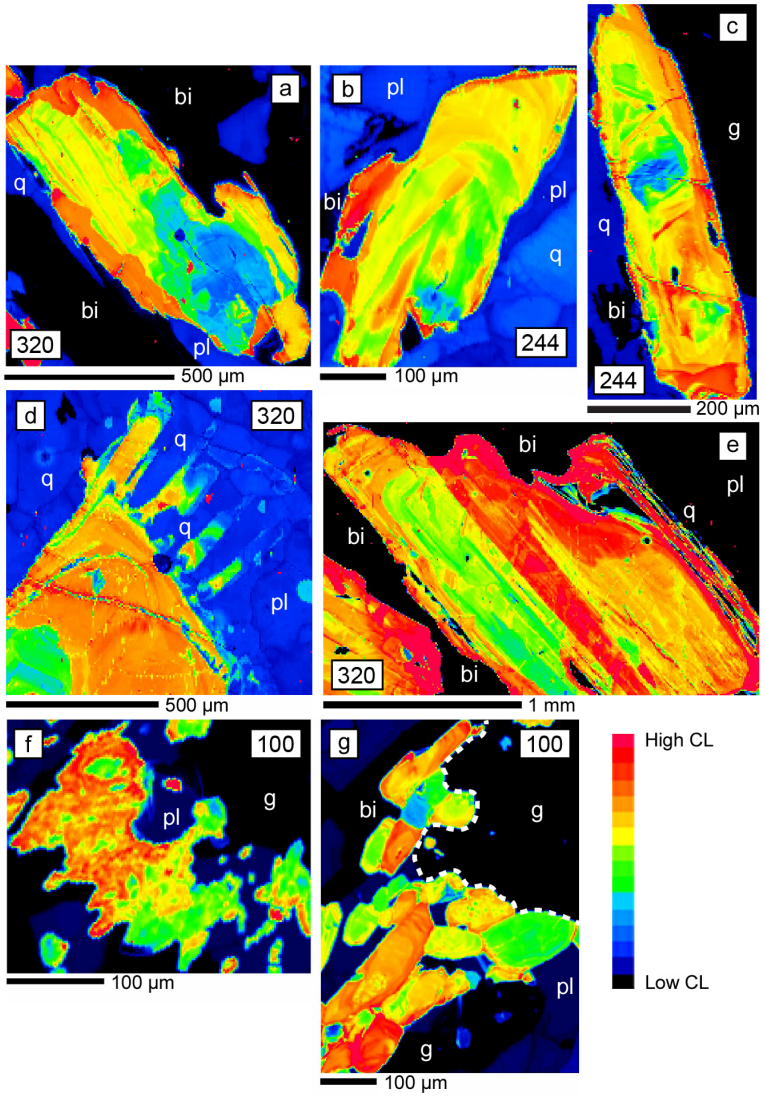

Figure 3.4. Cathodoluminescence intensity maps of kyanite. Intensity scales are comparable for each map aside from (e), where differences in intensity have been exaggerated. (a) Sample 320: kyanite crystal showing three distinct domains: a blue low CL core, crosscut by a green to yellow intermediate CL domain, crosscut by a homogeneous, orange to yellow, discontinuous rim. (b) Sample 244: kyanite porphyroblast showing similar structures to example in (a). (c) Sample 244: kyanite crystal showing three distinct domains with more complex internal patterns compared to (a) and (b), likely caused by the embayed interfaces between each domain. (d) Sample 320: composite kyanite porphyroblast with protruding, zoned overgrowths intergrown with quartz. A zoned, intermediate CL core is visible in the lower left, overgrown by a more subtly-zoned high CL domain. (e) Sample 320: a large kyanite crystal with an intermediate CL core and higher CL rim. A sharp divide in CL intensity marks a twin plane in the kyanite. (f) Sample 100: a small, xenomorphic, kyanite inclusion in garnet with mottled CL texture. (g) Sample 100: cluster of idiomorphic kyanite crystals partly replacing an embayed garnet porphyroblast (outlined). The kyanite display variable CL between crystals, some with oscillatory zonation and/or small cores with a mottled CL texture (e.g. large orange crystal in lower left).

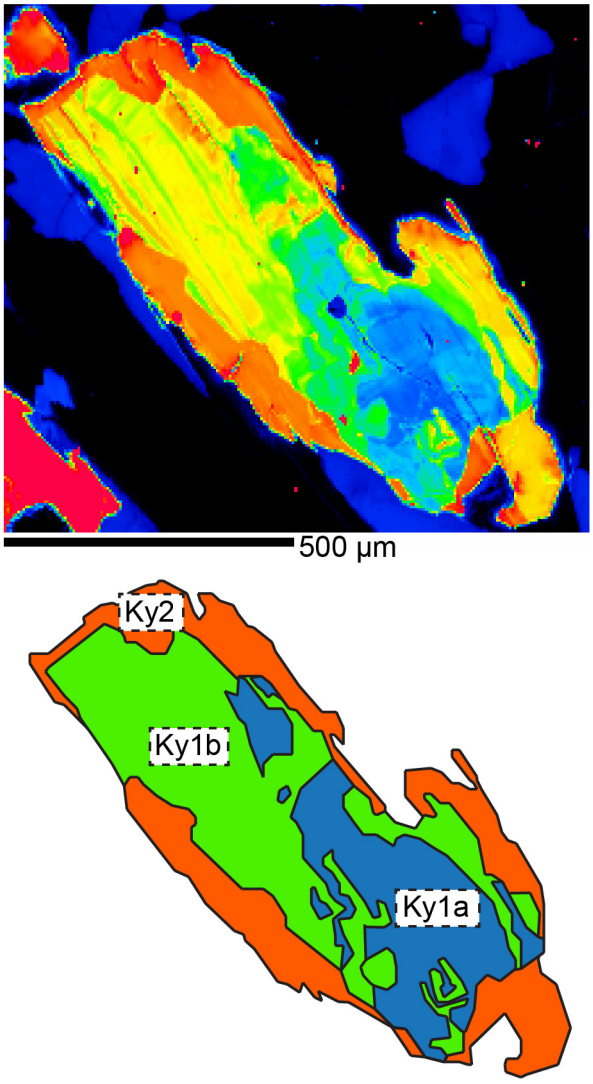

Figure 3.5. Sketch highlighting the distribution of and contacts between kyanite generations. Here, a highly irregular contact between Ky1a and Ky1b is apparent, with Ky1b infilling embayments in Ky1a.

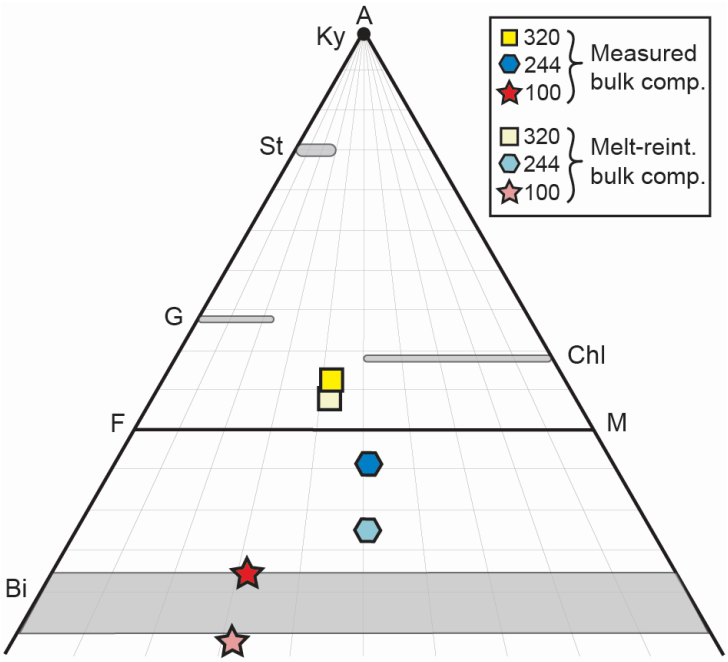

Figure 3.6. An AFM diagram with relevant phases (generalised compositions), measured sample bulk compositions, and melt-reintegrated bulk compositions projected from muscovite. St = staurolite, Chl = chlorite.

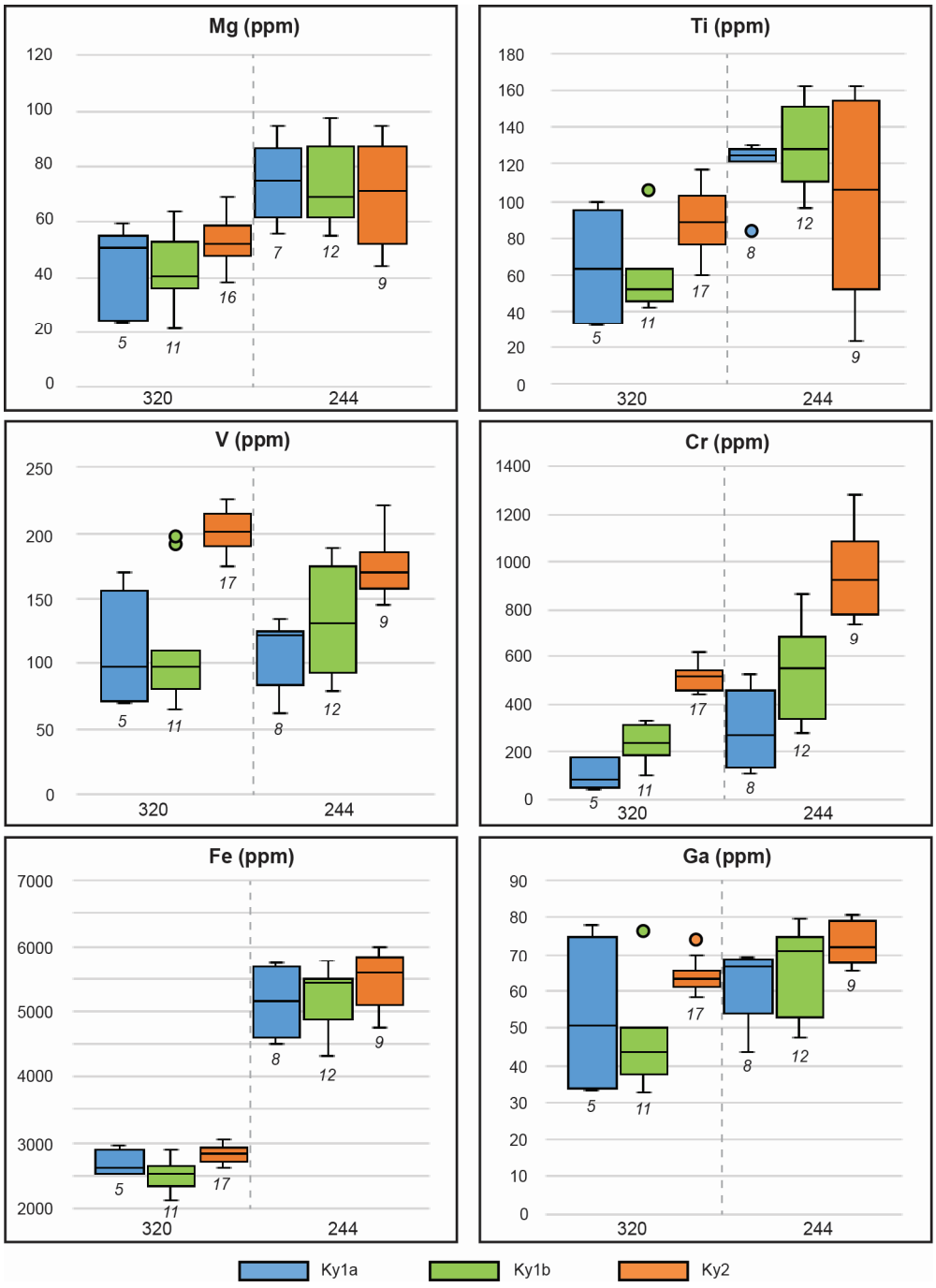

Figure 3.7. Box and whisker plots summarizing data collected for all trace elements detected in kyanite in samples 320 and 244. Each whisker extends to 1.5 times the interquartile range (above and below the box) at maximum, with outliers defined as data points beyond 1.5 times the interquartile range. The small numbers beneath each box indicate the number of analyses used to calculate the box, whiskers, and outliers.

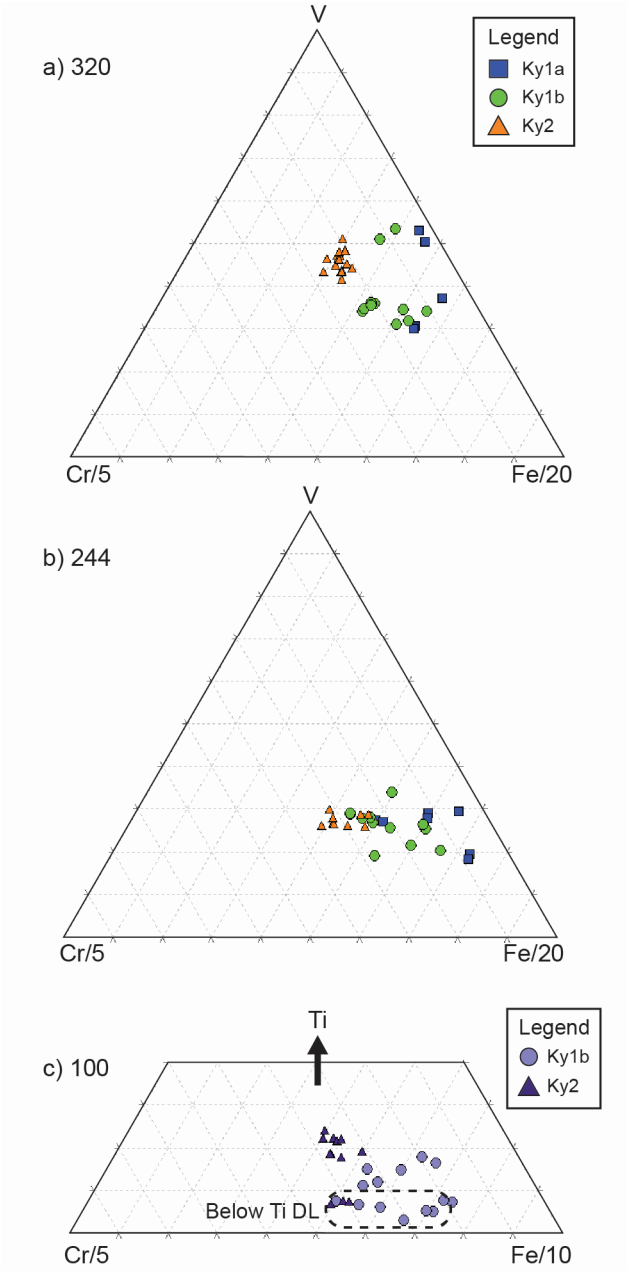

Figure 3.8. Ternary plots of kyanite trace element chemistry for each sample. Analytical error is smaller than the symbols. (a) Sample 320: V vs. Cr vs. Fe plot. Ky2 rims cluster together, and some Ky1b analyses form a distinct cluster. The Ky1a and some Ky1b data are more widely spread. (b) Sample 244: V vs. Cr vs. Fe plot. Ky2 rim analyses are the most tightly clustered group, with Ky1a and Ky1b analyses showing considerable overlap and spread. (c) Sample 100: Ti vs. Cr vs. Fe plot. Many Ky2 analyses are richer in Ti and poorer in Fe than Ky1b analyses. Analyses below Ti detection limit were given a value of 23 ppm Ti, half the EPMA detection limit for Ti.

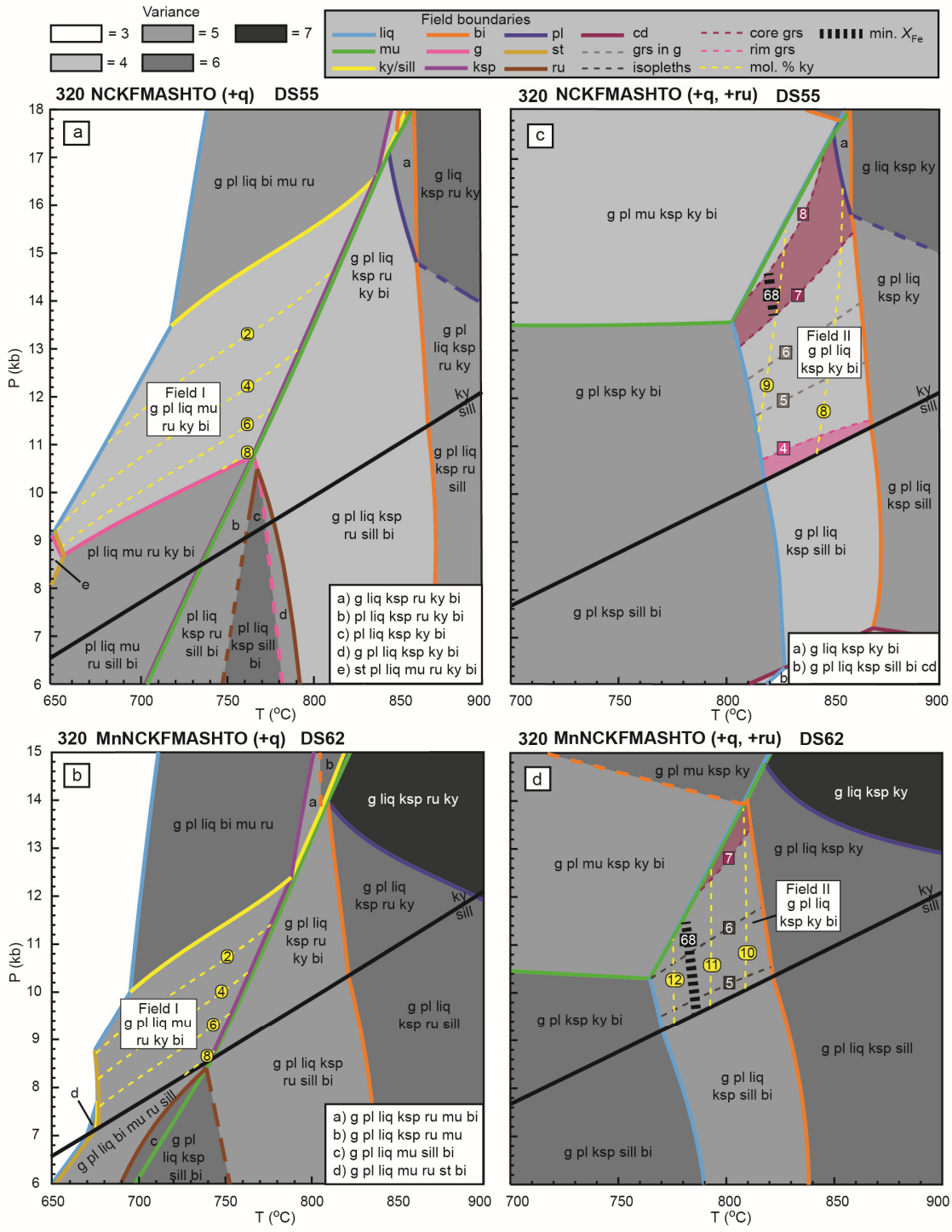

Figure 3.9. Pseudosections calculated for sample 320, with isopleths of equal proportion of kyanite, isopleths of X_{grs} in garnet, and an isopleth for the previously reported minimum X_{Fe} of garnet. (a) Melt-reintegrated pseudosection produced with DS55 dataset. (b) Melt-reintegrated pseudosection produced with DS62 dataset. (c) Residual pseudosection produced with DS55 dataset. (d)Residual pseudosection produced with DS62 dataset.

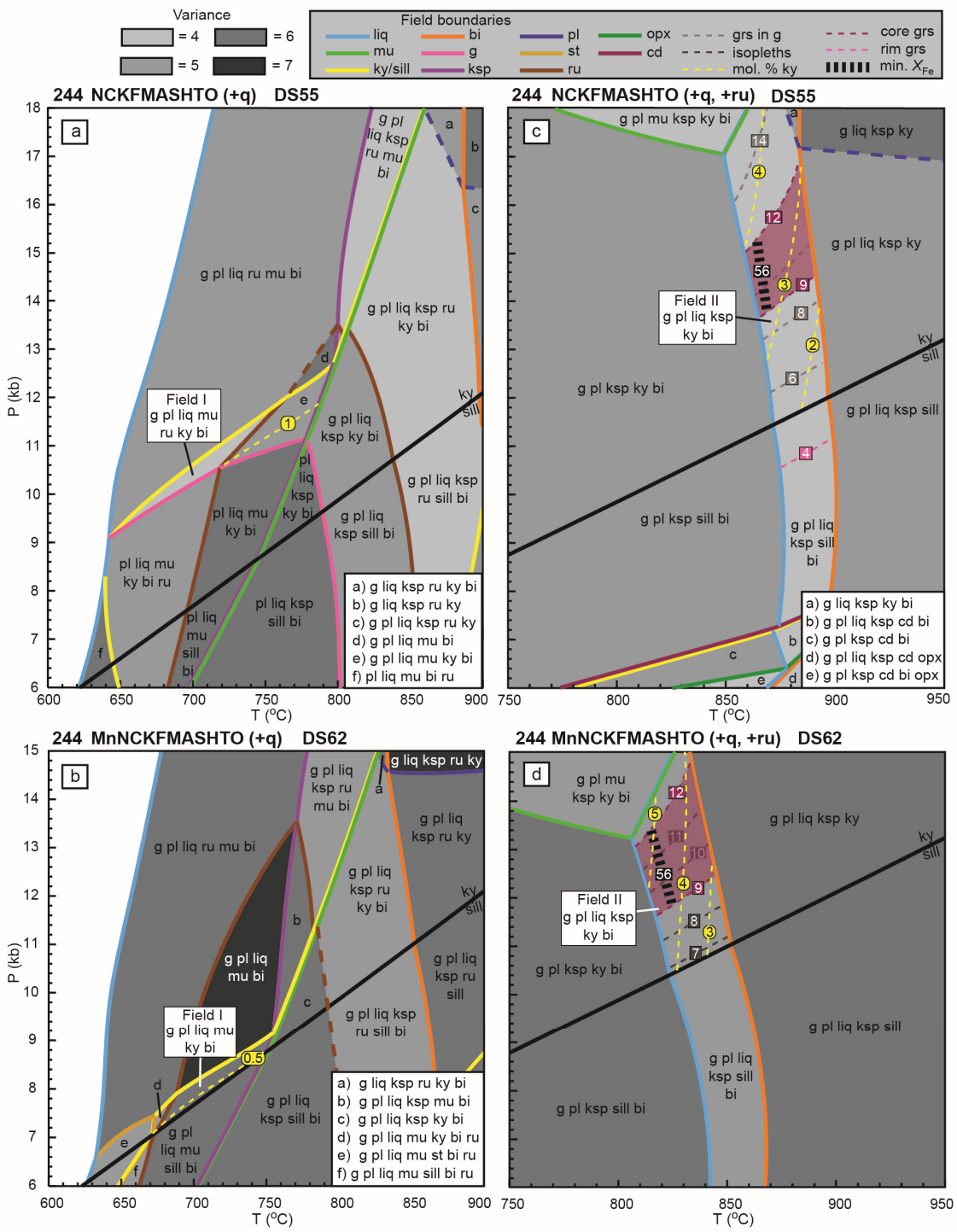

Figure 3.10. Pseudosections produced for sample 244 with isopleths of equal proportion of kyanite, isopleths of X_{grs} in garnet, and an isopleth for the previously reported minimum X_{Fe} of garnet. (a) Melt-reintegrated pseudosection produced with DS55 dataset. (b) Melt-reintegrated pseudosection produced with DS62 dataset. (c) Residual pseudosection produced with DS55 dataset. (d) Residual pseudosection produced with DS62 dataset.

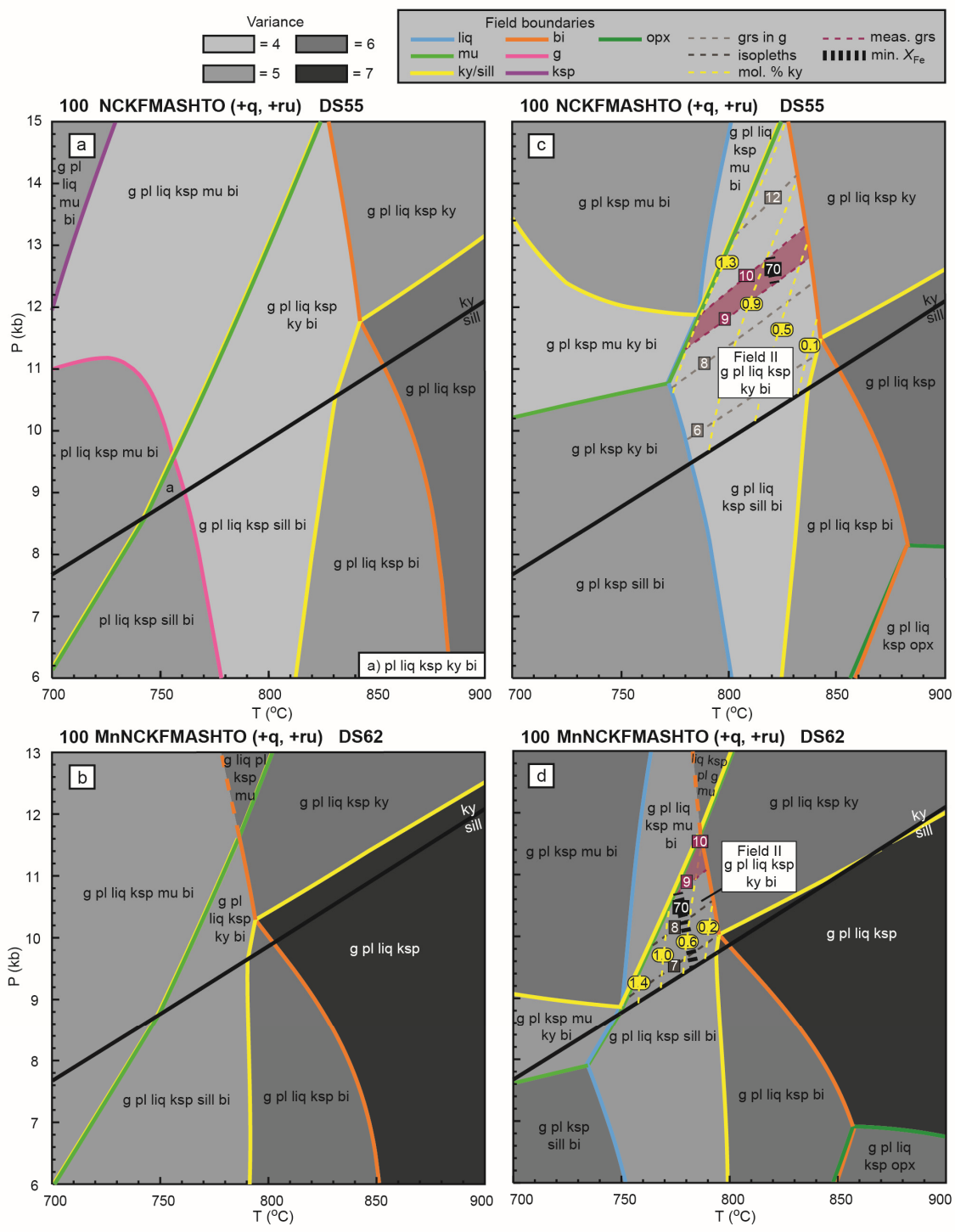

Figure 3.11. Pseudosections produced for sample 100, with isopleths of equal proportion of kyanite, isopleths of X_{grs} in garnet, and an isopleth for the previously reported minimum X_{Fe} of garnet. (a) Melt-reintegrated pseudosection produced with DS55 dataset. (b) Melt-reintegrated pseudosection produced with DS62 dataset. (c) Residual pseudosection produced with DS55 dataset. (d) Residual pseudosection produced with DS62 dataset.

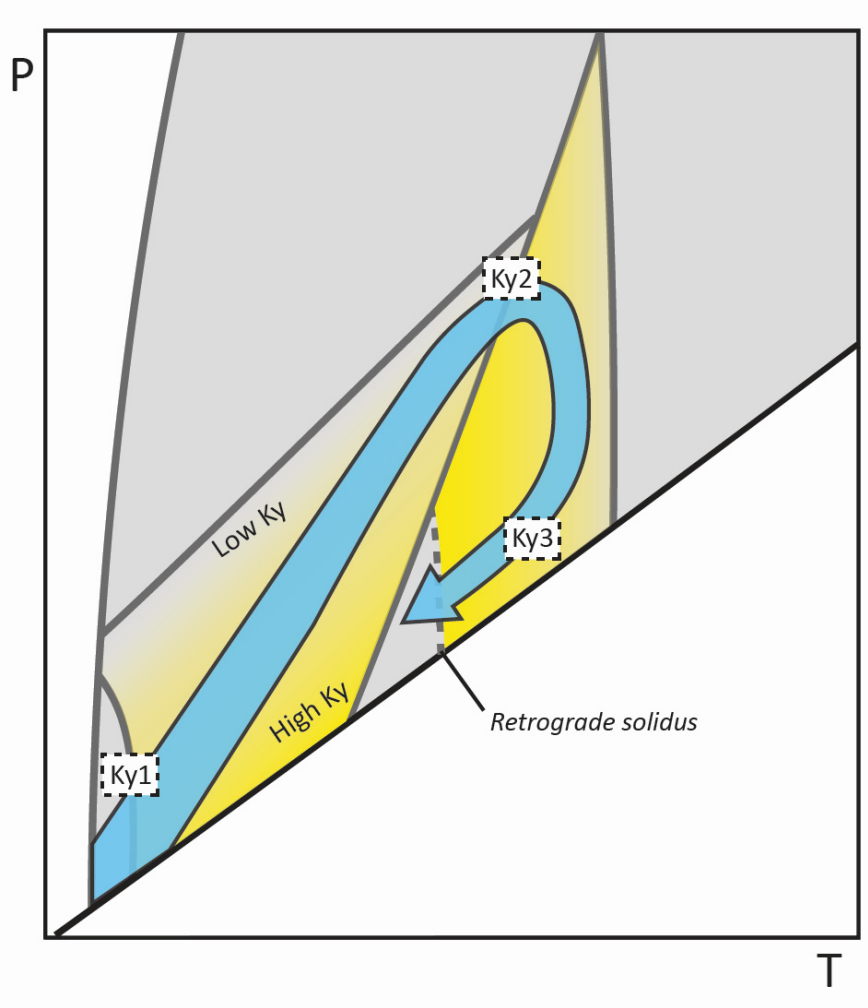

Figure 3.12. Schematic *P–T* diagram with *P–T* path for an aluminous bulk composition after melt-reintegration. The *P–T* evolution is based on the internal structures in kyanite observed in samples 320 and 244, as discussed in the text.

CHAPTER 4: SUMMARY

Trace element analysis and CL imaging were applied to anatectic aluminous granulites from the Grenville Province in Québec for the purpose of shedding new light on their metamorphic record, complementary to constraints from phase equilibria modelling. Quartz and kyanite, two chemically simple minerals, were shown to record important information about the evolution of these rocks based on the distribution of their trace elements.

The Ti record preserved in quartz, a mineral strongly linked to the process of anatexis, was investigated in five samples. Quartz partially consumed by melting reactions during prograde metamorphism was identified, mapped using CL, and analysed for trace Ti. Retrograde quartz produced by crystallisation of anatectic melt was also identified, and for two samples, it was found only by CL mapping. Retrograde, interstitial overgrowths on existing quartz are evident in CL maps, despite being invisible by the other methods used. The Ti content of retrograde quartz is generally lower than that of prograde quartz, and the interstitial quartz overgrowths are particularly Ti-poor. Titanium-in-quartz thermobarometry was evaluated by calculating Ti-in-quartz isopleths in *P–T* space and determining the Ti values expected for the previously constrained *P–T* paths of these samples. The activity of TiO_2 in these rocks was assumed to be 1.0, based on the presence of rutile in all samples. The highest Ti concentrations measured in prograde quartz in two samples were consistent with the inferred prograde to near-peak *P–T* conditions of these rocks; however, prograde quartz from the other samples was too Ti-poor. Given that Ti incorporation into quartz becomes less favourable at high *P*, the

relatively low Ti concentrations of retrograde quartz in all samples is inconsistent with this quartz growing at considerably lower *P* during melt crystallisation. These results suggest that despite the presence of rutile, a_{TiO2} was variable and less than 1.0 in most cases, caused by disequilibrium between quartz and rutile. Overall, this study demonstrated that CL imaging is an essential tool for interpreting the metamorphic history of quartz and for applying Ti-in-quartz thermobarometry. Additionally, the results have implications for evaluation of a_{TiO2} during metamorphism, as the presence of rutile in these rocks was not sufficient for equilibration between quartz and rutile.

Kyanite was examined in three anatectic aluminous granulites. Cathodoluminescence mapping revealed that kyanite porphyroblasts in two samples comprise up to three generations separated by resorbed interfaces, which are also distinguishable by their trace Cr (± V, Ti, Fe, and Ga) content. In the third sample, which has relatively low bulk Al, two generations of kyanite are present, one as inclusions in garnet and another in the groundmass or replacing garnet rims. These features were interpreted using phase equilibria modelling, with pseudosections produced from both the measured and melt-reintegrated bulk compositions of these samples. For the more aluminous samples, the earliest generation of kyanite can be linked to staurolite breakdown at amphibolite-facies conditions, with subsequent resorption caused by an increase in pressure. The second generation is consistent with production by dehydration melting of muscovite. These composite prograde porphyroblasts were then resorbed during biotite dehydration melting, and finally overgrown by a new rim of kyanite during retrogression. For the subaluminous sample, kyanite inclusions in garnet are interpreted

to have been produced by muscovite dehydration melting and groundmass kyanite is evidently retrograde. The presence of appreciable retrograde kyanite in the aluminous samples suggests a greater temperature range of melt crystallisation, and consequently higher peak temperature, than was estimated for these samples by previous work. This research is an unprecedented investigation into the metamorphic record of kyanite porphyroblasts, which is only made possible by CL imaging. Kyanite is shown here to record invaluable information about prograde and retrograde reactions in aluminous granulites, and these features can be used to place constraints on their *P–T* paths.

In conclusion, trace element analysis coupled with CL imaging is a powerful tool for interpreting the metamorphic history of anatectic aluminous granulites. Through the research conducted for this thesis, the behaviour of quartz and kyanite has been revealed to an extent that would be simply impossible by other methods. These results have implications beyond aluminous granulites – by showing that chemically simple minerals have the potential to contain a relatively detailed record of their growth history, a door has been opened to a novel method for investigating any metamorphic rock. Other luminescent minerals, such as feldspars or the other Al_2SiO_5 polymorphs, represent an avenue for fruitful future research, along with further investigation of quartz and kyanite in rocks of different metamorphic grades and bulk compositions. By combining the unconventional approach of coupled trace element analysis and CL imaging with conventional techniques such as phase equilibria modelling, the metamorphic history of rocks can be reconstructed in greater detail than ever before.

REFERENCES

Ackerson, M. R., Watson, E. B., Tailby, N. D., & Spear, F. S. (2017). Experimental investigation into the substitution mechanisms and solubility of Ti in garnet. American Mineralogist, 102, 158–172.

Ashley, K. T., & Law, R. D. (2015). Modeling prograde TiO2 activity and its significance for Ti-in-quartz thermobarometry of pelitic metamorphic rocks. Contributions to Mineralogy and Petrology, 169, 23.

Ashworth, J. R. (1972). Myrmekites of exsolution and replacement origins. Geological Magazine, 109, 45–62.

Audétat, A., Garbe-Schönberg, D., Kronz, A., Pettke, T., Rusk, B., Donovan, J. J., & Lowers, H. A. (2014). Characterisation of a natural quartz crystal as a reference material for microanalytical determination of Ti, Al, Li, Fe, Mn, Ga and Ge. Geostandards and Geoanalytical Research, 39, 171–184.

Bea, F. & Montero, P. (1999). Behavior of accessory phases and redistribution of Zr, REE, Y, Th, and U during metamorphism and partial melting of metapelites in the lower crust: An example from the Kinzigite Formation of Ivrea-Verbano, NW Italy. Geochimica et Cosmochimica Acta, 63, 1133–1153.

Bromiley, G. D., & Hiscock, M. (2016). Grain boundary diffusion of titanium in polycrystalline quartz and its implications for titanium in quartz (TitaniQ) geothermobarometry. Geochimica et Cosmochimica Acta, 178, 281–290.

Brown, M. (1994). The generation, segregation, ascent and emplacement of granite magma: The migmatite-to-crustally-derived granite connection in thickened orogens. Earth-Science Reviews, 36, 83-130.

Brown, M. (2013). Granite: From genesis to emplacement. Geological Society of America Bulletin, 125, 1079–1113.

Brown, M., & Korhonen, F.J. (2009). Some remarks on melting and extreme metamorphism of crustal rocks. In A.K. Gupta & S. Dasgupta (Eds.), Physics and chemistry of the Earth's interior (pp. 67–87). New York, NY: Springer.

Carrington, D.P., & Harley, S.L. (1995). Partial melting and phase relations in high-grade metapelites: An experimental petrogenetic grid in the KFMASH system. Contributions to Mineralogy and Petrology, 120, 270–291.

Cherniak, D. J., Watson, E. B., & Wark, D. A. (2007). Ti diffusion in quartz. Chemical Geology, 236, 65–74.

Chinner, G.A. (1965). The kyanite isograd in Glen Clova, Angus, Scotland. Mineralogical Magazine, 34, 132–143.

Chinner, G.A., Smith, J.V., & Knowles, C.R. (1969). Transition-metal contents of Al_2SiO_5 polymorphs. American Journal of Science, 267, 96–113.

Clemens, J. D. (2006). Melting of the continental crust: Fluid regimes, melting reactions, and source-rock fertility. In M. Brown & T. Rushmer (Eds.), Evolution and differentiation of the continental crust (pp. 297–331). Cambridge, UK: Cambridge University Press.

Coggon, R., & Holland, T. J. B. (2002). Mixing properties of phengitic micas and revised garnet-phengite thermobarometers. Journal of Metamorphic Geology, 20, 683–696.

Cox, R.A., & Indares, A. (1999). Transformation of Fe–Ti gabbro to coronite, eclogite and amphibolite in the Baie du Nord segment, Manicouagan Imbricate Zone, eastern Grenville Province. Journal of Metamorphic Geology, 17, 537–555.

Cox, R.A., Dunning, G.R., & Indares, A. (1998). Petrology and U–Pb geochronology of mafic, high-pressure, metamorphic coronites from the Tshenukutish domain, eastern Grenville Province. Precambrian Research, 90, 59–83.

Dare, S.A.S., Barnes, S.-J., Beaudoin, G., Méric, J., Boutroy, E., & Potvin-Doucet, C. (2014). Trace elements in magnetite as petrogenetic indicators. Mineralium Deposita, 49, 785–796.

Donovan, J. J., Lowers, H. A., & Rusk, B. G. (2011). Improved electron probe microanalysis of trace elements in quartz. American Mineralogist, 96, 274–282.

Dooley, D.F., & Patiño Douce, A.E. (1996). Fluid-absent melting of F-rich phlogopite + rutile + quartz. American Mineralogist, 81, 202-212.

Dunning, G., & Indares, A. (2010). New insights on the 1.7–1.0 Ga crustal evolution of the central Grenville Province from the Manicouagan – Baie Comeau transect. Precambrian Research, 180, 204–226.

Ewing, T. A., Hermann, J., & Rubatto, D. (2013). The robustness of the Zr-in-rutile and Ti-in-zircon thermometers during high-temperature metamorphism (Ivrea-Verbano Zone, northern Italy). Contributions to Mineralogy and Petrology, 165, 757–779.

Ferri, F., Poli, S., & Vielzeuf, D. (2009). An experimental determination of the effect of bulk composition on phase relationships in metasediments at near-solidus conditions. Journal of Petrology, 50, 909–931.

Ferry, J. M., & Watson, E. B. (2007). New thermodynamic models and revised calibrations for the Ti-in-zircon and Zr-in-rutile thermometers. Contributions to Mineralogy and Petrology, 154, 429–437.

Fournelle, J. H. (2007). The problem of secondary fluorescence in EPMA in the application of the Ti-in-zircon geothermometer and the utility of PENEPMA Monte Carlo program. Microscopy and Microanalysis, 13, 1390–1391.

García-Casco, A., Haissen, F., Castro, A., El-Hmidi, H., Torres-Roldán, R.L., & Millán, G. (2003). Synthesis of staurolite in melting experiments of a natural metapelite: Consequences for the phase relations in low-temperature pelitic migmatites. Journal of Petrology, 44, 1727–1757.

Gardien, V., Thompson, A.B., Grujic, D., & Ulmer, P. (1995). Experimental melting of biotite + plagioclase + quartz ± muscovite assemblages and implications for crustal melting. Journal of Geophysical Research, 100, 15581–15591.

Ghent, E. D., & Stout, M. Z. (1984). TiO2 activity in metamorphosed pelitic and basic rocks: Principles and applications to metamorphism in southeastern Canadian Cordillera. Contributions to Mineralogy and Petrology, 86, 248–255.

Griffen, D.T., & Ribbe, P.H. (1973). The crystal chemistry of staurolite. American Journal of Science, 273, 479–495.

Grigsby, J.D. (1992). Chemical fingerprinting in detrital ilmenite: A viable alternative in provenance research? Journal of Sedimentary Petrology, 62, 331–337.

Guevara, V.E., & Caddick, M.J. (2016). Shooting at a moving target: Phase equilibria modelling of high-temperature metamorphism. Journal of Metamorphic Geology, 34, 209–235.

Guilmette, C., Indares, A., & Hébert, R. (2011). High-pressure anatectic paragneisses from the Namche Barwa, Eastern Himalayan Syntaxis: Textural evidence for partial melting, phase equilibria modeling and tectonic implications. Lithos, 124, 66–81.

Hayden, L. A., & Watson, E. B. (2007). Rutile saturation in hydrous siliceous melts and its bearing on Ti-thermometry of quartz and zircon. Earth and Planetary Science Letters, 258, 561–568.

Herz, N., & Dutra, C.V. (1964). Geochemistry of some kyanites from Brazil. The American Mineralogist, 49, 1290–1305.

Hickmott, D., & Spear, F.S. (1992). Major- and trace-element zoning in garnets from calcareous pelites in the NW Shelburne Falls Quadrangle, Massachusetts: Garnet growth histories in retrograded rocks. Journal of Petrology, 33, 965–1005.

Hietanen, A. (1956). Kyanite, andalusite, and sillimanite in the schist in Boehls Butte Quadrangle, Idaho. The American Mineralogist, 41, 1–27.

Hodych, J.P., & Dunning, G.R. (1992). Did the Manicouagan impact trigger end-of-Triassic mass extinction? Geology, 20, 51–54.

Holland, T. J. B., & Powell, R. (1998). An internally consistent thermodynamic data set for phases of petrological interest. Journal of Metamorphic Geology, 16, 309–343.

Holland, T. J. B., & Powell, R. (2003). Activity-composition relations for phases in petrological calculations: An asymmetric multicomponent formulation. Contributions to Mineralogy and Petrology, 145, 492–501.

Holland, T.J.B., & Powell, R. (2011). An improved and extended internally consistent thermodynamic dataset for phases of petrological interest, involving a new equation of state for solids. Journal of Metamorphic Geology, 29, 333–383.

Holness, M. B., & Sawyer, E. W. (2008). On the pseudomorphing of melt-filled pores during the crystallization of migmatites. Journal of Petrology, 49, 1343–1363.

Holness, M.B., Cesare, B., & Sawyer, E.W. (2011). Melted rocks under the microscope: Microstructures and their interpretation. Elements, 7, 247–252.

Huang, R., & Audétat, A. (2012). The titanium-in-quartz (TitaniQ) thermobarometer: A critical examination and re-calibration. Geochimica et Cosmochimica Acta, 84, 75–89.

Huang, W.L., & Wyllie, P.J. (1974). Melting relations of muscovite with quartz and sanidine in the K2O-Al2O3-SiO2-H2O system to 30 kilobars and an outline of paragonite melting relations. American Journal of Science, 274, 378–395.

Huang, W.L., & Wyllie, P.J. (1975). Melting reactions in the system NaAlSi3O8-KAlSi3O8-SiO2 to 35 kbar, dry and with excess water. Journal of Geology, 83, 737–748.

Indares, A. (1993). Eclogitized gabbros from the eastern Grenville Province: Textures, metamorphic context, and implications. Canadian Journal of Earth Sciences, 30, 159–173.

Indares, A. (1995). Metamorphic interpretation of high-pressure–temperature metapelites with preserved growth zoning in garnet, eastern Grenville Province, Canadian Shield. Journal of Metamorphic Geology, 13, 475–486.

Indares, A. D. (2003). Metamorphic textures and *P–T* evolution of high-*P* granulites from the Lelukuau terrane, NE Grenville Province. Journal of Metamorphic Geology, 21, 35–48.

Indares, A., & Dunning, G. (2001). Partial melting of high-P–T metapelites from the Tshenukutish Terrane (Grenville Province): Petrography and U–Pb geochronology. Journal of Petrology, 42, 1547–1565.

Indares, A., & Moukhsil, A. (2013). Geon 12 crustal extension in the central Grenville Province, implications for the orogenic architecture, and potential influence on the emplacement of anorthosites. Canadian Journal of Earth Sciences, 50, 955–966.

Indares, A., Dunning, G., & Cox, R. (2000). Tectono-thermal evolution of deep crust in a Mesoproterozoic continental collision setting: The Manicouagan example. Canadian Journal of Earth Sciences, 37, 325–340.

Indares, A., Dunning, G., Cox, R., Gale, D., & Connelly, J. (1998). High-pressure, high-temperature rocks from the base of thick continental crust: Geology and age

constraints from the Manicouagan Imbricate Zone, eastern Grenville Province. Tectonics, 17, 426–440.

Indares, A., White, R. W., & Powell, R. (2008). Phase equilibria modelling of kyanite-bearing anatectic paragneisses from the central Grenville Province. Journal of Metamorphic Geology, 26, 815–836.

Jordan, S. L., Indares, A., & Dunning, G. (2006). Partial melting of metapelites in the Gagnon terrane below the high-pressure belt in the Manicouagan area (Grenville Province): Pressure-temperature (*P–T*) and U–Pb age constraints and implications. Canadian Journal of Earth Sciences, 38, 1309–1329.

Kawasaki, T., & Osanai, Y. (2008). Empirical thermometer of TiO_2 in quartz for ultrahigh-temperature granulites of East Antarctica. In M. Satish-Kumar, Y. Motoyoshi, Y. Osanai, Y Hiroi, and K. Shiraishi (Eds.), Geodynamic Evolution of East Antarctica: A Key to the East-West Gondwana Connection (pp. 419-430). Geological Society, London, Special Publications 308.

Kelsey, D. E., Clark, C., & Hand, M. (2008). Thermobarometric modelling of zircon and monazite growth in melt-bearing systems: Examples using model metapelitic and metapsammitic granulites. Journal of Metamorphic Geology, 26, 199–212.

Kooijman, E., Smit, M. A., Mezger, K., & Berndt, J. (2012). Trace element systematics in granulite facies rutile: Implications for Zr geothermometry and provenance studies. Journal of Metamorphic Geology, 30, 397–412.

Korchinski, M., Little, T.A., Smith, E., & Millet, M.-A. (2012). Variation of Ti-in-quartz in gneiss domes exposing the world's youngest ultrahigh-pressure rocks, D'Entrecasteaux Islands, Papua New Guinea. Geochemistry, Geophysics, Geosystems, 13, 1–27.

Korhonen, F.J., Clark, C., Brown, M., & Taylor, R.J.M. (2014). Taking the temperature of Earth's hottest crust. Earth and Planetary Science Letters, 408, 341–354.

Lasalle, S., & Indares, A. (2014). Anatectic record and contrasting P–T paths of aluminous gneisses from the central Grenville Province. Journal of Metamorphic Geology, 32, 627–646.

Lasalle, S., Fisher, C. M., Indares, A., & Dunning, G. (2013). Contrasting types of Grenvillian granulite facies aluminous gneisses: Insights on protoliths and metamorphic events from zircon morphologies and ages. Precambrian Research, 228, 117–130.

Le Breton, N., & Thompson, A.B. (1988). Fluid-absent (dehydration) melting of biotite in metapelites in the early stages of crustal anatexis. Contributions to Mineralogy and Petrology, 99, 226–237.

Leeman, W. P., MacRae, C. M., Wilson, N. C., Torpy, A., Lee, C.-T. A., Student, J. J., Thomas, J. B., & Vicenzi, E. P. (2012). A study of cathodoluminescence and trace element compositional zoning in natural quartz from volcanic rocks: Mapping titanium content in quartz. Microscopy and Microanalysis, 18, 1322–1341.

Lofgren, G. (1974). An experimental study of plagioclase crystal morphology: Isothermal crystallization. American Journal of Science, 274, 243–273.

Luvizotto, G. L., & Zack, T. (2009). Nb and Zr behavior during high-grade metamorphism and retrogression: An example from the Ivrea–Verbano Zone. Chemical Geology, 261, 303–317.

Meyer, M., John, T., Brandt, S., & Klemd, R. (2011). Trace element composition of rutile and the application of Zr-in-rutile thermometry to UHT metamorphism (Epupa Complex, NW Namibia). Lithos, 126, 388–401.

Mitchell, R. J., & Harley, S. L. (2017). Zr-in-rutile resetting in aluminosilicate bearing ultra-high temperature granulites: Refining the record of cooling and hydration in the Napier Complex, Antarctica. Lithos, 272–273, 128–146.

Morgan, D. J., Jollands, M. C., Lloyd, G. E., & Banks, D. A. (2014). Using titanium-in-quartz geothermometry and geospeedometry to recover temperatures in the aureole of the Ballachulish Igneous Complex, NW Scotland. Geological Society, London, Special Publications 394, 145–165.

Müller, A., Lennox, P., & Trzebski, R. (2002). Cathodoluminescence and micro-structural evidence for crystallisation and deformation processes of granites in the Eastern Lachlan Fold Belt (SE Australia). Contributions to Mineralogy and Petrology, 143, 510–524.

Müller, A., van den Kerkhof, A.M., Selbekk, R.S., & Broekmans, M.A.T.M. (2016). Trace element composition and cathodoluminescence of kyanite and its petrogenetic implications. Contributions to Mineralogy and Petrology, 171, 70.

O'Brien, P.J., & Rötzler, J. (2003). High-pressure granulites: Formation, recovery of peak conditions and implications for tectonics. Journal of Metamorphic Geology, 21, 3–20.

Palin, R. M., Weller, O. M., Waters, D. J. & Dyck, B. (2016). Quantifying geological uncertainty in metamorphic phase equilibria modelling; a Monte Carlo assessment and implications for tectonic interpretations. Geoscience Frontiers, 7, 591–607.

Patiño Douce, A.E., & Johnston, A.D. (1991). Phase equilibria and melt productivity in the pelitic system: Implications for the origin of peraluminous granitoids and aluminous granulites. Contributions to Mineralogy and Petrology, 107, 202–218.

Paton, C., Hellstrom, J., Paul, B., Woodhead, J., & Hergt, J. (2011). Iolite: freeware for the visualisation and processing of mass spectrometric data. Journal of Analytical Atomic Spectrometry, 26, 2508–2518.

Pattison, D.RM., De Capitani, C., & Gaidies, F. (2011). Petrological consequences of variations in metamorphic reaction affinity. Journal of Metamorphic Geology, 9, 953–977.

Pearson, G.R., & Shaw, D.M. (1960). Trace elements in kyanite, sillimanite and andalusite. The American Mineralogist, 45, 808–817.

Peterson, J.W., Chacko, T., & Kuehner, S.M. (1991). The effects of fluorine on the vapor-absent melting of phlogopite + quartz: Implications for deep-crustal processes. American Mineralogist, 76, 470-476.

Powell, R., & Holland, T. J. B. (1988). An internally consistent dataset with uncertainties and correlations: 3. Applications to geobarometry, worked examples and a computer program. Journal of Metamorphic Geology, 6, 173–204.

Rasband, W.S. (2016). ImageJ, U. S. National Institutes of Health, Bethesda, Maryland, USA, https://imagej.nih.gov/ij/.

Rivers, T. (1983a). Progressive metamorphism of pelitic and quartzofeldspathic rocks in the Grenville Province of western Labrador – tectonic implications of bathozone 6 assemblages. Canadian Journal of Earth Sciences, 20, 1791–1804.

Rivers, T. (1983b). The northern margin of the Grenville Province in western Labrador – anatomy of an ancient orogenic front. Precambrian Research, 22, 41–73.

Rivers, T., Culshaw, N., Hynes, A., Indares, A., Jamieson, R., & Martignole, J. (2012). The Grenville orogen – a post lithoprobe perspective. In J.A. Percival, F.A. Cook, & R.M. Clowes (Eds.), Tectonic Styles in Canada: The Lithoprobe Perspective (pp. 97–236). Geological Survey of Canada, Special Paper 49.

Rivers, T., Ketchum, J., Indares, A., & Hynes, A. (2002). The High Pressure belt in the Grenville Province: Architecture, timing, and exhumation. Canadian Journal of Earth Sciences, 39, 867–893.

Rivers, T., Martignole, J., Gower, C.F., & Davidson, A. (1989). New tectonic divisions of the Grenville Province, southeast Canadian Shield. Tectonics, 8, 63–84.

Rivers, T., van Gool, J.A.M., & Connelly, J.N. (1993). Contrasting tectonic styles in the northern Grenville Province: Implications for the dynamics of orogenic fronts. Geology, 21, 1127–1130.

Rusk, B. (2014). Quartz cathodoluminescence: Textures, trace elements, and geological applications. In I.M Coulson (Ed.), Cathodoluminescence and its Application to Geoscience (pp. 127–142). Mineralogical Association of Canada, Mineralogical Association of Canada Short Course Series Volume 45.

Rusk, B.G., Lowers, H.A., & Reed, M.H. (2008). Trace elements in hydrothermal quartz: Relationships to cathodoluminescent textures and insights into vein formation. Geology, 36, 547–550.

Sawyer, E. W. (1999). Criteria for the recognition of partial melting. Physics and Chemistry of the Earth, Part A: Solid Earth and Geodesy, 24, 269–279.

Schertl, H.-P., Neuser, R.D., Sobolev, N.V., & Shatsky, V.S. (2004). UHP-metamorphic rocks from Dora Maira/Western Alps and Kokchetav/Kazakhstan: New insights using cathodoluminescence petrography. European Journal of Mineralogy, 16, 49–57.

Spear, F. S., & Wark, D. A. (2009). Cathodoluminescence imaging and titanium thermometry in metamorphic quartz. Journal of Metamorphic Geology, 27, 187–205.

Spear, F.S., & Kohn, M.J. (1996). Trace elements zoning in garnet as a monitor of crustal melting. Geology, 24, 1099–1102.

Spear, F. S., Kohn, M. J., & Cheney, J. T. (1999). P-T paths from anatectic pelites. Contributions to Mineralogy and Petrology, 134, 17–32.

Spear, F.S., & Pattison, D.R.M. (2017). The implications of overstepping for metamorphic assemblage diagrams (MADs). Chemical Geology, 457, 38–46.

Spear, F.S., Kohn, M.J., & Cheney, J.T. (1999). P-T paths from anatectic pelites. Contributions to Mineralogy and Petrology, 134, 17–32.

Storm, L. C., & Spear, F. S. (2009). Application of the titanium-in-quartz thermometer to pelitic migmatites from the Adirondack Highlands, New York. Journal of Metamorphic Geology, 27, 479–494.

Thomas, J. B., Watson, E. B., Spear, F. S., & Wark, D. A. (2015). TitaniQ recrystallized: Experimental confirmation of the original Ti-in-quartz calibrations. Contributions to Mineralogy and Petrology, 169, 27.

Thomas, J. B., Watson, E. B., Spear, F. S., Shemella, P. T., Nayak, S. K., & Lanzirotti, A. (2010). TitaniQ under pressure: The effect of pressure and temperature on the solubility of Ti in quartz. Contributions to Mineralogy and Petrology, 160, 743–759.

Tohver, E., Bettencourt, J.S., Tosdal, R., Mezger, K., Leite, W.B., & Payolla, B.L. (2004). Terrane transfer during the Grenville orogeny: Tracing the Amazonian ancestry of southern Appalachian basement through Pb and Nd isotopes. Earth and Planetary Science Letters, 228, 161–176.

Tomkins, H. S., Powell, R., & Ellis, D. J. (2007). The pressure dependence of the zirconium-in-rutile thermometer. Journal of Metamorphic Geology, 25, 703–713.

van Gool, J.A.M., Rivers, T., & Calon, T. (2008). Grenville Front zone, Gagnon terrane, southwestern Labrador: Configuration of a midcrustal foreland fold-thrust belt. Tectonics, 27, TC1004.

Vielzeuf, D., & Clemens, J.D. (1992). The fluid-absent melting of phlogopite + quartz: Experiments and models. American Mineralogist, 77, 1206–1222.

Vielzeuf, D., & Holloway, J.R. (1988). Experimental determination of the fluid-absent melting relations in the pelitic system: Consequences for crustal differentiation. Contributions to Mineralogy and Petrology, 98, 257–276.

Walderhaug, O., & Rykkje, J. (2000). Some examples of the effect of crystallographic orientation on the cathodoluminescence colors of quartz. Journal of Sedimentary Research, 70, 545–548.

Wark, D. A., & Watson, E. B. (2006). TitaniQ: A titanium-in-quartz geothermometer. Contributions to Mineralogy and Petrology, 152, 743–754.

Waters, D. J. (2001). The significance of prograde and retrograde quartz-bearing intergrowth microstructures in partially melted granulite-facies rocks. Lithos, 56, 97–110.

White, R. W., & Powell, R. (2002). Melt loss and the preservation of granulite facies mineral assemblages. Journal of Metamorphic Geology, 20, 621–632.

White, R.W., Powell, R., & Holland, T.J.B. (2007). Progress relating to calculation of partial melting equilibria for metapelites. Journal of Metamorphic Geology, 25, 511–527.

White, R.W., Powell, R., & Johnson, T.E. (2014a). The effect of Mn on mineral stability in metapelites revisited: New a–x relations for manganese-bearing minerals. Journal of Metamorphic Geology, 32, 809–828.

White, R.W., Powell, R., Holland, T.J.B., Johnson, T.E., & Green, E.C.R. (2014b). New mineral activity–composition relations for thermodynamic calculations in metapelitic systems. Journal of Metamorphic Geology, 32, 261–286.

Wiebe, R.A., Wark, D.A., & Hawkins, D.P. (2007). Insights from quartz cathodoluminescence zoning into crystallization of the Vinalhaven granite, coastal Maine. Contributions to Mineralogy and Petrology, 154, 439–453.

Wojtowicz, A.J. (1991). Luminescence of Cr^{3+} in kyanite. Journal of Luminescence, 50, 221–230.

Yakymchuk, C., & Brown, M. (2014). Behaviour of zircon and monazite during crustal melting. Journal of the Geological Society, London, 171, 465–479.

Yang, P., & Rivers, T. (2000). Trace element partitioning between coexisting biotite and muscovite from metamorphic rocks, Western Labrador: Structural, compositional and thermal controls. Geochimica et Cosmochimica, 64, 1451–1472.

Yang, P., & Rivers, T. (2001). Chromium and manganese zoning in pelitic garnet and kyanite: Spiral, overprint, and oscillatory (?) zoning patterns and the role of growth rate. Journal of Metamorphic Geology, 19, 455–474.

Yardley, B.W.D., Rochelle, C.A., Barnicoat, A.C., & Lloyd, G.E. (1991). Oscillatory zoning in metamorphic minerals: An indicator of infiltration metasomatism. Mineralogical Magazine, 55, 357–365.

Zack, T., von Eynatten, H., & Kronz, A. (2004). Rutile geochemistry and its potential use in quantitative provenance studies. Sedimentary Geology, 171, 37–58.

Zack, T., Moraes, R., & Kronz, A. (2004). Temperature dependence of Zr in rutile: Empirical calibration of a rutile thermometer. Contributions to Mineralogy and Petrology, 148, 471–488.

Zane, A., Sassi, R., & Guidotti, C.V. (1998). New data on metamorphic chlorite as a petrogenetic indicator mineral, with special regard to greenschist-facies rocks. The Canadian Mineralogist, 36, 713–726.

Zhang, C., Holtz, F., Koepke, J., Berndt, J., & Ma, C. (2014). Decompressional anatexis in the migmatite core complex of northern Dabie orogen, eastern China: Petrological evidence and Ti-in-quartz thermobarometry. Lithos, 202–203, 227–236.